WIRELESS BODY AREA NETWORKS FOR INTRA-SPACESUIT COMMUNICATIONS: MODELING, MEASUREMENTS AND WEARABLE ANTENNAS

by

MOHAMMED TAJ-ELDIN

B.S., University of Aleppo, 2008
M.S., Florida Institute of Technology, 2011

AN ABSTRACT OF A DISSERTATION

submitted in partial fulfillment of the requirements for the degree

DOCTOR OF PHILOSOPHY

Department of Electrical and Computer Engineering
College of Engineering

KANSAS STATE UNIVERSITY
Manhattan, Kansas

2015

Abstract

Wireless body area networks (WBANs) are an important part of the developing internet of things (IOT). NASA currently uses space suits with wired sensors to collect limited biomedical data. Continuous monitoring and collecting more extensive body vital signs is important to assess astronaut health. This dissertation investigates wireless biomedical sensor systems that can be easily incorporated into future space suits to enable real time astronaut health monitoring. The focus of the work is on the radio-wave channel and associated antennas.

We show that the space suit forms a unique propagation environment where the outer layers of the suit's thermal micrometeoroid garment are largely radio opaque. This environment can be modeled as a coaxial one in which the body itself plays the role of the coax center conductor while the space suit shielding materials play the role of the outer shield. This model is then validated through simulations and experiments.

Selecting the best frequency of operation is a complex mixture of requirements, including frequency allocations, attenuation in propagation, and antenna size. We investigate the propagation characteristics for various frequency bands from 315 MHz to 5.2 GHz. Signal attenuation is analyzed as a function of frequency for various communication pathways through 3D simulations and laboratory experiments. Small-scale radio channel results indicate that using lower frequency results in minimal path loss. On the other hand, measurements conducted on a full-scale model suggest that 433 MHz and 2400 MHz yield acceptable path loss values. Propagation between the left wrist and left ankle yielded the worst overall path loss, but signals were still above –100 dBm in raw measurements for a 0dBm transmission indicating that the intra-suit environment is conducive to wireless propagation.

Our findings suggest that the UHF bands are best candidate bands since there is interplay between the body conductivity favoring lower frequencies, and the difficulty of coupling RF energy into and out of the channel using suitably sized antennas favoring higher frequencies.

Finally, a new self-shielded folded bow-tie antenna is proposed that can be a promising choice for the general area of WBAN technologies as well as potential new space suit environments.

WIRELESS BODY AREA NETWORKS FOR INTRA-SPACESUIT COMMUNICATIONS: MODELING, MEASUREMENTS AND WEARABLE ANTENNAS

by

MOHAMMED TAJ-ELDIN

B.S., University of Aleppo, 2008
M.S., Florida Institute of Technology, 2011

A DISSERTATION

submitted in partial fulfillment of the requirements for the degree

DOCTOR OF PHILOSOPHY

Department of Electrical and Computer Engineering
College of Engineering

KANSAS STATE UNIVERSITY
Manhattan, Kansas

2015

Approved by:

Co-Major Professor
William Bill Kuhn

Approved by:

Co-Major Professor
Bala Natarajan

Copyright

Abstract

Wireless body area networks (WBANs) are an important part of the developing internet of things (IOT). NASA currently uses space suits with wired sensors to collect limited biomedical data. Continuous monitoring and collecting more extensive body vital signs is important to assess astronaut health. This dissertation investigates wireless biomedical sensor systems that can be easily incorporated into future space suits to enable real time astronaut health monitoring. The focus of the work is on the radio-wave channel and associated antennas.

We show that the space suit forms a unique propagation environment where the outer layers of the suit's thermal micrometeoroid garment are largely radio opaque. This environment can be modeled as a coaxial one in which the body itself plays the role of the coax center conductor while the space suit shielding materials play the role of the outer shield. This model is then validated through simulations and experiments.

Selecting the best frequency of operation is a complex mixture of requirements, including frequency allocations, attenuation in propagation, and antenna size. We investigate the propagation characteristics for various frequency bands from 315 MHz to 5.2 GHz. Signal attenuation is analyzed as a function of frequency for various communication pathways through 3D simulations and laboratory experiments. Small-scale radio channel results indicate that using lower frequency results in minimal path loss. On the other hand, measurements conducted on a full-scale model suggest that 433 MHz and 2400 MHz yield acceptable path loss values. Propagation between the left wrist and left ankle yielded the worst overall path loss, but signals were still above –100 dBm in raw measurements for a 0dBm transmission indicating that the intra-suit environment is conducive to wireless propagation.

Our findings suggest that the UHF bands are best candidate bands since there is interplay between the body conductivity favoring lower frequencies, and the difficulty of coupling RF energy into and out of the channel using suitably sized antennas favoring higher frequencies.

Finally, a new self-shielded folded bow-tie antenna is proposed that can be a promising choice for the general area of WBAN technologies as well as potential new space suit environments.

Table of Contents

List of Figures

List of Tables

Acknowledgements

بسم الله الرحمن الرحيم

In the name of Allah, the Most Merciful, the Most Compassionate

(وَقُل رَّبِّ زِدْنِي عِلْمًا)

Say,"My Lord, increase me in knowledge." (Quran, 20:114)

First and foremost I praise Allah for blessing me and giving me the opportunity to pursue this program and being able to study as there are many people who cannot pursue their educational dreams in circumstances that are beyond desire.

This dissertation would have not been possible without the help of other people during the years of project. I would like to send special thanks to my advisors: Prof. William Kuhn and Prof. Bala Natarajan for their guidance, motivation, encouragement and their uninterrupted help. Their way of inspiring my imagination, passionate to learn and think critically is very valuable asset for me. Also, I would like thank my committee members: Dr. Steven Warren, Dr. Minyoung Suh, a former professor in the Department of Apparel, Textiles, and Interior Design for her help in wearable textile antennas design, and outside committee chairperson; Dr. Bret Flanders for reading the draft and providing valuable feedback.

Also, special thanks to the sponsor of this project, Kansas NASA EPSCoR, for funding their project for whole three years and then extending the funding upon request. In addition, I would like to thank my colleagues who donated some of their valuable time to help me in conducting extensive laboratory experiments; Amelia Hodges Fowles, Garrett Peterson, Muhannad Alshetaiwi, Shuo Ouyang, German Sanchez, Erin Monfort-Nelson, Virashree Patel, and Jiazhang Song. Also, my labmates: Siddharth Deshmukh, Shafiul Alam, Kan Chen, Kumarsinh Jhala, Chang Liu, and Wenji Zhang.

Dedication

I dedicate this dissertation to my mother, Rabaa Alnayef and my father, Radwan Tajeddin, whose unconditional love and support made this work possible.

O my Lord! have compassion on them, as they brought me up when I was little

(Quran, 23:24)

(وَقُل رَّبِّ ارْحَمْهُمَا كَمَا رَبَّيَانِي صَغِيرًا)

Chapter 1 - Introduction

The rising median age of most industrial countries and the associated potential rise in healthcare cost has become a problematic societal phenomenon. For example, the percentage of people over the age of 65 in the United States is projected to rise from 14% in 2015 to approximately 21% in 2050 [1], as shown in Figure 1.1. This problem is projected to be even more threatening in countries such as Japan which has a population that is aging faster than any other country. In fact, the percentage of people falling in this category is expected to jump from 13% in 2015 to 34% in 2050, introducing unprecedented challenges for governments and strategic planners.

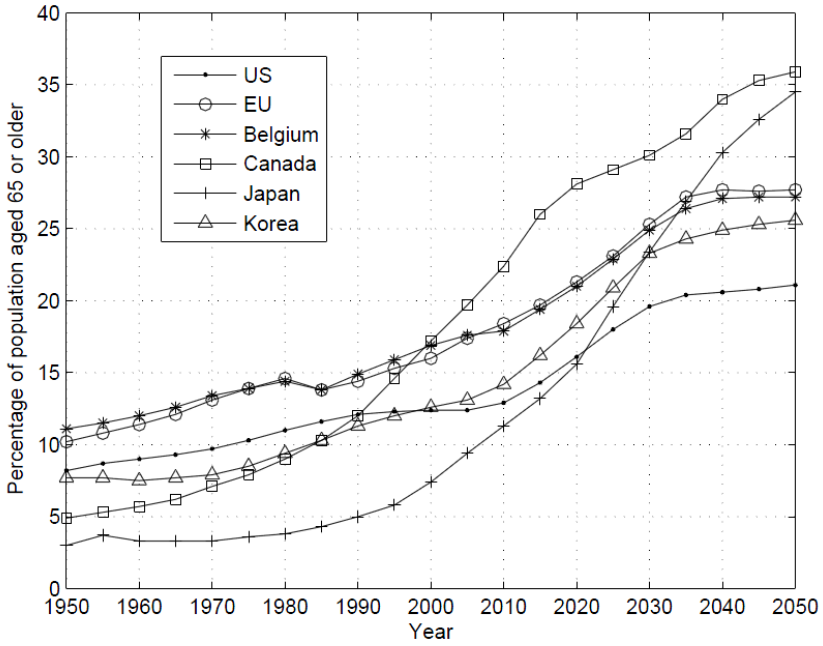

Figure 1.1 Population percentage of 65 years or older from 1950 until 2050 [data obtained from the World Health Organization [2]]

These challenges introduce opportunities for biomedical engineers to come up with innovative solutions. Preemptive monitoring of a patient's vital body health parameters traditionally involves wired biomedical sensors that can measure parameters such as body

temperature, respiration rate, and heart rate. However, a primary disadvantage of using wired sensor is that this kind of sensor is inconvenient and uncomfortable for elderly people, especially those susceptible to skin irritations. In addition, continuous monitoring of a patient's vital body signs typically requires medical staff responsible for caring for those patients, thereby increasing the cost of healthcare systems. Therefore, the demand to seek unconventional heath monitoring techniques is appealing from engineering, medical, and economic perspectives.

Recent advancements in wireless communications and on-body portable devices offer a key element of a solution and have attracted the attention of wireless, biomedical, and healthcare professionals and investors. Widespread deployment of wireless technologies such as Bluetooth, Wi-Fi, wireless sensor networks, heterogeneous networks, and new generation mobile communication systems, such as the 5G and Internet of Things (IoT), offer the promise of potential integration of these technologies. One of these technologies, body-centric wireless communications, is anticipated to be a significant portion of the fourth and fifth generation mobile communication systems and is the focus of this dissertation.

1.1 Wireless Body Area Networks

A body-centric wireless network is comprised of a set of wireless sensors that are placed in, on, or in proximity to the human body. These sensors collect multiple vital body signs, and share that data with other units, such as external devices or a gateway radio such as a patient's cellphone. Body-centric communication technology incorporates various technologies that can be used separately or combined, including wireless body area networks (WBANs), wireless personal area networks (WPANs), and body sensor networks (BSNs).

WBANs are built around small wireless sensors on or inside the body that collect relevant health information and send the data to a central node that is also worn on the body. Some potential medical applications for WBANs are listed in Table 1.1 [3].

Table 1.1 Some medical applications of wireless body area networks

Signal	Application examples	Average data rates (kbps)
EEG	Sleep analysis, epilepsy research and monitoring, localize damaged brain tissue	10 – 100
ECG	Remote patient heart monitoring, research and early identification of Parkinson's disease, research child development of motor skills	10 – 100
EMG	Physiotherapy, identify fall risk among elderly, research and early identification of Parkinson's disease, research child development of motor skills	10 – 100
EEG Similarity index	Seizure warning systems	0.5
Blood pressure	Patient monitoring and automatic emergency response, sport applications	0.01 – 0.1
O_2 and CO_2 levels	Patient monitoring and automatic emergency response, identify respiratory illnesses	0.01 – 0.1
Glucose levels	Diabetic patient monitoring, automatic administration of insulin	0.01 – 0.1

According to the IEEE 802.15 standardization group, WBANs utilize a variety of communication, including on-body, off-body, or in-body communications. Figure 1.2 depicts on-body and off-body communication scenarios.

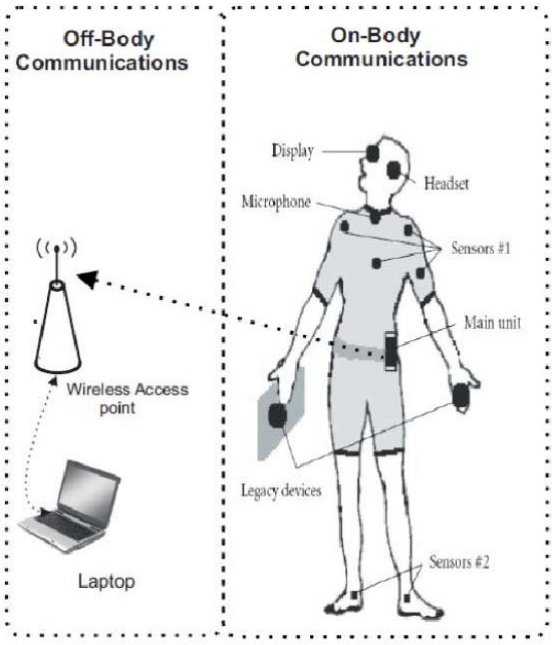

Figure 1.2 Wireless body area network and possible components for on-body and off-body communications [reproduced from [4]]

Three types of communication can be defined in the context of WBAN:

1) **On-body communication**

   On-body communication exchanges data between body-mounted devices that communicate wirelessly.

2) **Off-body communication**

   Off-body communication describes wireless links between on-body devices and base units or mobile units located in ambient environments.

3) **In-body communication**

   In-body communications describes links and relays that exchange data between implant devices and on-body nodes.

The next Section reviews common spectrum allocations for WBANs.

1.2 Medical and non-Medical Spectrum Allocation

Without loss of generality, this research focuses on communication systems that operate in licensed and unlicensed portions of the spectrum suitable for medical system related WBANs.

Table 1.2 Licensed and unlicensed bands suitable for medical communications

Name Licensed (L), Unlicensed (U)	Frequency band (MHz)	Max. Transmit power (dBm EIRP)	Max. duty cycle	Region
ISM, (U)	433.1 – 434.8	+7.85	10%	Region 1 (Europe, Arica, the Middle East, and Russia)
ISM, (U)	868.0 – 868.6	+11.85	1%	Europe
ISM, (U)	902.0 – 928.0	+ 36 w/ spreading	-	US
ISM, (U)	2400.0 – 2483.5	+36 w/ spreading	-	Worldwide
MICS, (U)	402.0 – 405.0	-16.0	-	Worldwide
MedRadio, (L)	401 – 206			US
MedRadio, (L)	413 – 419			US
…	426 – 432			US
…	438 – 444			US
MedRadio, (L)	451 – 457			US
WMTS, (U)	608 – 614			US
WMTS, (U)	1395 – 1400	+10.8		US
WMTS, (U)	1427 – 1432	+22.2		US
MBANs (L)	2360 – 2400	+22.2		US

Bands considered include Industrial, Scientific, and Medical bands (ISM), Medical Implanted Communication System bands (MICS), Medical Device Radiocommunications Service bands (MedRadio), Wireless Medical Telemetry Service bands (WMTS), Medical Body Area Networks bands (MBANs), and Ultra-wideband. Frequency bands and sub-bands for these regions are provided in Table 1.2.

1.2.1 Industrial, Scientific, and Medical Bands

ISM bands were initially allocated for international non-commercial use. However, ISM bands are also used in commercial devices such as Wi-Fi networks. Frequency bands may vary

based on regulations specific to each country. Examples of ISM bands include the international band in the range of 2400.0 – 2483.5 MHz and a country-specific band in the range of 868.0 – 868.6 MHz band that can be used only in Europe.

1.2.2 Medical Implanted Communication System Band

MICS bands, occupying the region of 402.0 – 405.0 MHz, can communicate data from implants inside the human body to an external device with a radio receiver in order to monitor patient data. The MICS band has a restriction to narrow bandwidth (300 KHz) signaling. Transmit power is also limited to 25 microwatts.

1.2.3 Medical Device Radiocommunications Service Bands

MedRadio bands consist of the sub-bands 401 - 406, 413 - 419, 426 - 432, 438 - 444, and 451 - 457 MHz [5], licensed by the Federal Communication Commission (FCC) for use in the United States, these sub-bands can be used for diagnostic and therapeutic objectives in conjunction with in-body or on-body communication technologies. Unfortunately, however, devices operating at these bands cannot be used outside the United States since their band is not licensed in other countries.

1.2.4 Wireless Medical Telemetry Service Bands

WMTS bands comprise a wireless service established by the FCC in 2000 in order to transmit a patient's biomedical data to a remote location such as a nurse's station that incorporates a radio receiver [6]. This data includes a patient's vital body signs, such as pulse and respiration rates. As shown in Table 1.2, WMTS includes three bands: 608 – 614, 1395 – 1400, and 1427 – 1432 MHz.

1.2.5 Medical Body Area Networks Band

In May 2012, the FCC has adopted a portion of the spectrum for what is called the Medical Body Area Networks [7]. This band occupies the region from 2360 – 2400 MHz where it is adjacent to the unlicensed band that hosts Bluetooth, most of Wi-Fi, and other wireless applications. In particular, it is divided into two sub-bands: 2360 – 2390 MHz and 2390 – 2400 MHz.

However, this band can only be used with low-power signals within indoor environments due to the fact that aircraft flight test stations use this spectrum and the medical device can cause interfering signals with test receive stations if placed close to them.

1.2.6 Ultra-Wideband

In 2002, the FCC defined Ultra-Wideband (UWB) communication as any transmission system that occupies an instantaneous bandwidth exceeding 500 MHz or having a fractional bandwidth of more than 20% in which fractional bandwidth is defined as the ratio of the 10 dB bandwidth to the center frequency. UWB has a very wide bandwidth (3.1 to 10.6 GHz), thereby enabling audio and video data transmission and allowing potential unprecedented medical and general-use applications.

The following two sections will focus on the motivations and goals of our research.

1.3 Motivations

WBANs have attracted considerable research interest for the last decade because of the wide variety of possible applications, including telemedicine, sports applications, and applications for persons in extreme environments such as firefighters, mine workers, and outer space. Unfortunately, current space suits are limited in their ability to collect medical information. They use wired links to acquire electrocardiogram (ECG) data and can indirectly

monitor oxygen uptake on a long-term basis. For future missions such as missions to asteroids and Mars, additional monitoring is desired.

Replacing the current system with wireless sensors would provide several benefits, including:

1) Protection against mechanical wear associated with wiring.

2) Ability to monitor multiple vital body signs in order to better understand the burden on astronauts and its effects on astronaut health.

3) Easy reconfiguration of sensor placement.

WBANs are able to monitor multiple vital body signs, such as heart rate, respiration rate, and muscle fatigue. The benefits of replacing wired links with wireless link in addition to the variety of body signs that can be monitored with this technology has inspired the study and design of a WBAN for astronauts in this work.

This research investigates astronaut wireless body area networks (AWBANs) in which a central master node receives data transmitted from various sensor nodes distributed on the body. A sensor node is simply a device that incorporates radio transceiver, microcontroller, memory, antenna and various medical sensors collecting vital body biomedical data, may process them, and transmit the information/data to other nodes via the antenna. The master node is envisioned to be powered by the backpack and provide the off-body link. The sensor nodes are low power devices using buttery or energy harvesting technologies [8]. In conjunction with NASA Johnson Space Center, researchers at the Kansas State University Department of Kinesiology [9], Manhattan, Kansas, recommended strategic sensor types and locations for astronaut health and fatigue monitoring. The work covered in this dissertation is focused on determining if such a system can be built by assessing the radio link within the suit.

1.4 Research Objectives

Goals of the study can be summarized as follows:

1) *Understanding tissue absorption and impact of space suit material at various frequencies*. Since the human body is known to absorb radio energy, an understanding of radio wave interactions and absorption is needed. The space suit material and its shielding properties also need to be studied. This understanding is vital to the design of a successful AWBAN.
2) *Investigation and development of propagation models for intra-suit radio signals*. Signal attenuation is analyzed and simulated as a function of frequency for various communication pathways within a space suit. Small scale space suit model (e.g., arm space suit segment) is used initially. The assumption that the arm and space suit section have cylindrical geometry simplifies the problem and enables quantification of path loss as a function of frequency, thereby allowing recommendation of optimal carrier frequencies for low-power transmitters and expected data rates for intra-suit wireless communication systems. A subset of movements associated with physical activity that affects relative orientation of communication pathways is also investigated. Based on availability of off-the-shelf integrated circuits and the size of practical antennas, UHF frequencies through approximately 10 GHz were emphasized in the theoretical and experimental study.
3) *Performance evaluation in a full-scale space suit mock-up model*. This evaluation involved both 3D simulations on and laboratory measurements in full scale space suit method.

4) *Investigation of techniques for launching electromagnetic waves into the space suit radio channel.* This part investigates possible antennas for the intra-suit environment and determines optimal antenna orientations and polarizations at various body locations to ensure minimal path loss in the wireless links.
5) *Development of on-body wearable, flexible, cost-effective antennas in the emerging MedRadio* band that are conformal to the human body and provide reliable on-body wireless links during movement.

1.5 Prior Efforts

Early research of WBANs focused on statistical modeling for characterizing their radio channels for on-body communications and on simulation methods. In [10], the authors theoretically and experimentally studied on-body radio channels using a method based on the Friss formula and a novel local distorted non-orthogonal Finite Difference Time-Domain (LN-FDTD). In narrowband channel characterization, most probability distributions of path gain are log-normal, and the distribution spread depends on the degree of freedom between the transmitter and the receiver locations. For a wideband channel, system performance is evaluated and compared based on the antenna that is used: a horn-shaped self-complementary antenna (HSCA) or a planar inverted cone antenna (PICA). Results showed that PICA outperforms HSCA in terms of root mean square (RMS) delay spread for free space propagation.

In [11], the author investigated the performance of an on-body radio channel that utilized microstrip patch antennas. Propagation links were categorized based on body locations on which the transmitter and receiver antennas were placed. A comparison of system performance for various body postures and activities was also conducted. According to the author, path loss of the measured data fit log-normal cumulative distribution function (CDF), and monopole antennas

produced superior performance. The graphed bit error rate (BER) vs. signal-to-noise ratio (SNR) was used to analyze system performance, revealing that the system produced superior performance for trunk-to-head and trunk-to-hand compared to other on-body links. However, system performance degraded as higher data rates were used.

In [12], the authors exploited the capabilities of conformal Finite-Difference Time-Domain (FDTD), Finite Element Method (FEM), and Finite Integral Technique (FIT) to model on-body radio channels at a frequency of 2.4 GHz. The authors suggested that conformal FDTD provides superior performance compared the other methods when modeling the geometric path of waves traveling through and on the surface of the human body. In fact, the system suffered variable path loss amounts when body posture changed in the case of narrowband channels. These results held when the experiment was conducted in the lab and multipath propagation occurred. In addition, signal attenuation was higher compared to that for anechoic chamber environment. However, the RMS delay spread decreased and produced higher path loss when using HSCA antennas for UWB communication as opposed to the case when PICA antenna was used. In fact, RMS delays were fairly high because of line-of-sight propagation in the anechoic chamber.

Other research works have concentrated on development of models for UWB propagation channels because this type of communication has advantageous for low power consumption, high data rates, and robustness against jamming signals. For example, in [13], the authors investigated UWB on-body radio propagation at high frequencies (3 to 9 GHz) in which channel characterization was derived and system level analysis modeling was conducted. The study also compared communication channel performances when body postures and activities as well as antenna orientation were changed.

In [14], the author introduced a body area network that does not use antenna theory by attempting to develop a WBAN using a conductive fabric. His goal was to develop a garment for remote wearable health monitoring that utilizes conductive fabric sheets for data transmission. However, the author did not use antennas to transmit biological data, but parallel conductors (Parallel-Plate Transmission line model) instead. Therefore, the concept of direct-current power-line carrier communication (DC-PLC) was utilized. This model incorporates impedance change at the shoulder section of the human body. According to the author, experimental results agreed with results obtained using the proposed transmission line model in the frequency range of 100 KHz to 100 MHz.

In all previous studies, propagation analysis and modeling were conducted for typical WBANs. However, to the best of this author's knowledge, no work has been published for radio frequency (RF) signal propagation inside a space suit. This dissertation is focused on that unique environment.

1.6 Contributions

Major contributions of this dissertation are listed below:

- A novel analytical model is proposed for the intra-space suit propagation environment (see Chapter 4). The proposed model is a coaxial-cable propagation structure with the body serving as a lossy center conductor and the conductive suit material taking the role of the outer shield. These contributions were published in our paper [15].
- The effect of antenna polarization and the frequency of operation on path loss experienced in an intra-space suit propagation environment is quantified via a small scale suit model (see Chapter 4). Specifically, the vertical polarization was found to

result in lower path loss values compared to that produced using horizontal polarization. Also, the path loss for higher frequency bands generally results in higher path loss values. These contributions were published in our paper [16].

- Analysis, simulation, and measurement results based on a full scale space suit model/mock-up (see Chapter 5) indicate that the radio channel has enough link-margin to allow low-power energy-harvesting systems (e.g., transmit power of 1 mW) to be built and to communicate within the suit at data rates up to 10 Mbps or higher. These contributions were published in our papers [17] and [18]. These results can serve as a basis for development of wireless links and intra-space suit antennas for NASA's next-generation space suits to be used in long-term missions to explore remote planets and other interplanetary missions.
- We discovered that the radio-opacity of the space suit is affected based on the physical stress that the space suit experiences. Specifically, our measurements (see Chapter 3) suggest that arm segments that typically endure significant wear due to frequent movement tend to become less radio-opaque relative to rigid torso-segment.
- We propose a novel self-shielded bow-tie antenna operating in the MedRadio band with superior performance compared to existing antennas (see Chapter 6). These contributions are presented in our paper [19]. Findings related to antennas used and developed in this study also can guide antenna development for commercial use in general wireless BANs and potential integration into space suit fabrics.

1.7 Organization of the Dissertation

This dissertation is organized as follows:

Chapter 2 includes a review of basic electric properties of human body tissues and fundamentals of radio channel propagation. This chapter also includes reviews of recent works regarding body-centric wireless communications.

Chapter 3 includes discussion of the structure of the extravehicular mobility unit (EMU) space suit and its electromagnetic shielding. This chapter also includes discussion and analysis of shielding properties of metal in general using principles of physics and validation from laboratory experiments.

Chapter 4 describes propagation models and includes an evaluation of intra-space suit loss characteristics at various frequency bands for the arm segment of a space suit.

Chapter 5 includes expanded discussion of the study conducted in the arm space suit segment, resulting in a full-scale space suit model propagation model. This chapter also contains details of the effects of space suit breaks at body joints and other body parts on propagation performance.

Chapter 6 builds on the study conducted and evaluates the performance of several on-body wearable antennas at MedRadio band and proposes a novel antenna design that overcomes the drawbacks found in those antennas.

Chapter 7 provides the overall conclusions and findings of the research. The chapter also recommends potential future research directions.

Chapter 2 - Electromagnetic Interaction and Modelling of the Human Body

As explained in the introduction, the aim of this research is to investigate the intra-space suit propagation environment. However, a thorough understanding of electrical properties of human tissues and how electromagnetic waves interact with body tissues is necessary in order to comprehend details of this research. Therefore, this chapter begins with a brief discussion of dielectric properties of human tissues, specifically the relative dielectric constant and electrical conductivity, including a study of their behavior at various frequency bands for different body tissues. In addition, the electromagnetic energy absorption problem for the human body and how it has been historically investigated is presented in this chapter. This review will enable the transition to general radio channel propagation and in particular in the context of body-centric wireless communications. Research works related to this field are provided and summarized.

2.1 Electric Properties of Human Tissues

In the context of wireless communications for body area networks, electromagnetic waves interact significantly with human body tissues. However, the nature and degree of this interaction varies depending on body location and relative tissue thickness of different layers compared to total thickness. Therefore, a thorough understanding of the nature of this interaction and parameters affecting it is essential. Certain parameters of human tissue are commonly used to model electromagnetic properties of body tissues, namely relative permittivity ε_r and conductivity σ (S/m). Another important factor is the frequency of the operation which plays a significant role in determining the values of these parameters, including dielectric properties and others that are presented in the following paragraphs.

Dielectric properties of body tissues at radio frequencies and microwave frequencies have been investigated by various researchers studying electromagnetics biocompatibility. Measurements of live tissues are typically not feasible because the probe usually used must be in contact with the tissue. Therefore, almost all EM biocompatibility studies are conducted on dead tissues, and an open-ended coaxial probe technique [20] is used for most measurements. The results obtained using dead tissues are fairly representative and can be applied to the case when live tissues are used. However, for this research, all experiments will be conducted on real human subjects.

In order to highlight dependence on operating frequency, Figure 2.1 illustrates varying conductivity and relative permittivity for various body tissues for a range of 1 KHz to 10 GHz.

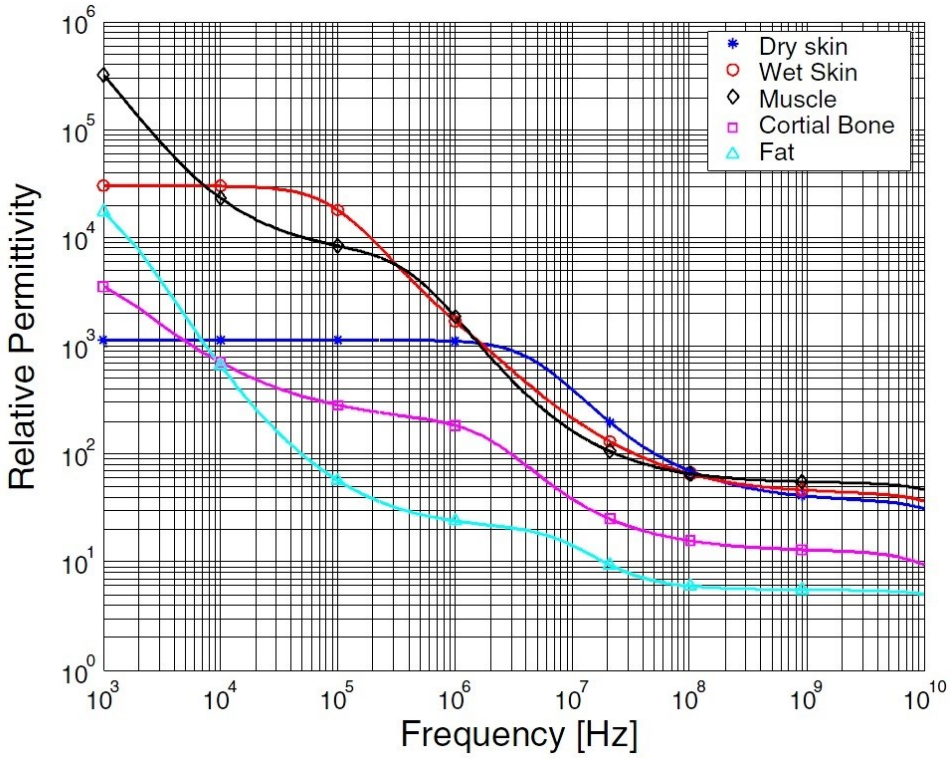

Figure 2.1 Simulated real relative permittivity for various tissues calculated with the Cole-Cole Eq. (2.2), and the dielectric parameters from Gabriel [21]

As shown in Figure 2.1, permittivity generally decreases as frequency increases. However, conductivity of a certain tissue increases as frequency increases, especially at frequencies above 1000 MHz.

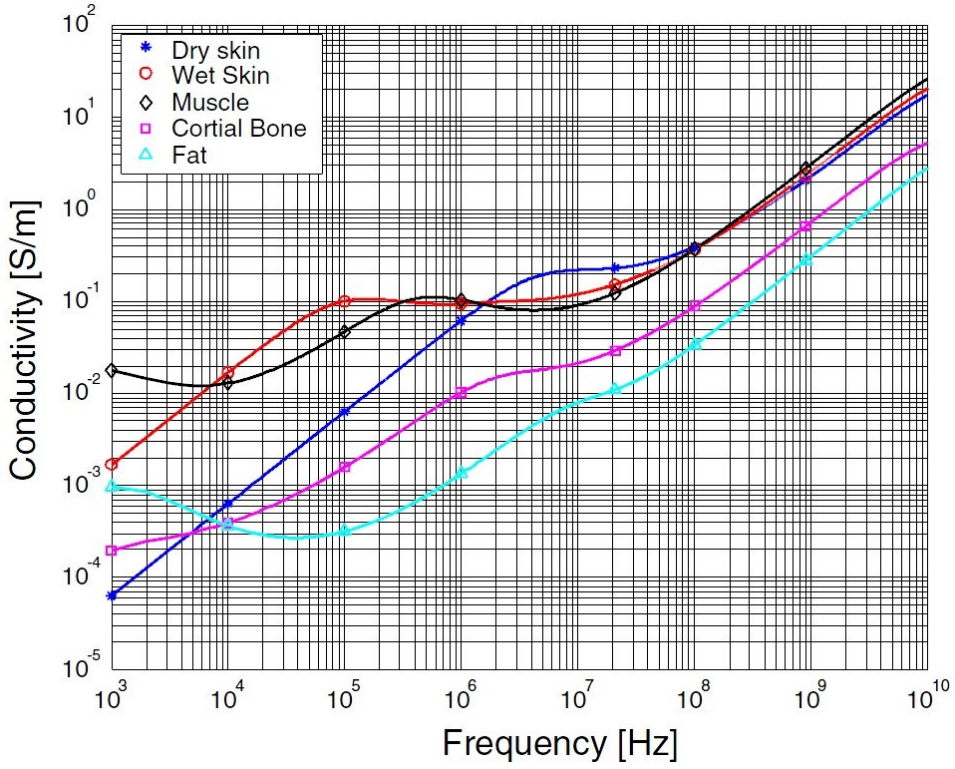

Figure 2.2 Simulated conductivity for various tissues calculated with the Cole-Cole Eq. (2.2), and the dielectric parameters from Gabriel [21]

2.1.1.1 Relative permittivity, conductivity, skin depth and attenuation models

A related parameter is the complex relative permittivity that has the following form:

$$\varepsilon_r'(\omega) = \varepsilon' - j\varepsilon'' = \varepsilon' - j\left(\frac{\sigma_j}{\omega\varepsilon_0}\right) . \tag{2.1}$$

where $\varepsilon_r'(\omega)$ denotes material complex relative permittivity as a function of angular frequency ω, ε' denotes real part of material permittivity, ε'' denotes imaginary part of material permittivity, and σ_j denotes ionic conductivity.

Several computational models have been proposed to produce values for relative permittivity and conductivity that are close to those measured and plotted in Figure 2.1 and Figure 2.2. One commonly used model, the Cole-Cole Model, produces fairly comparable results to the measured ones in its first order approximation. However, an improved and more accurate fourth order Cole-Cole Model was developed [21]:

$$\varepsilon_r'(\omega) = \varepsilon_\infty + \sum_{m=1}^{4} \frac{\Delta\varepsilon_m}{1+(j\omega\tau_m)^{(1-\alpha_m)}} + \frac{\sigma_j}{j\omega\varepsilon_0} \quad . \tag{2.2}$$

where $\varepsilon_r'(\omega)$ denotes material complex relative permittivity as a function of angular frequency ω, ε_∞ denotes material permittivity at terahertz frequency, ε_0 denotes free-space permittivity, and σ_j denotes ionic conductivity. Dispersion is given by $\Delta\varepsilon_m = \varepsilon_{s_m} - \varepsilon_{s_\infty}$, where ε_{s_m} is static permittivity at which angular frequency ω multiplied by relaxation time τ_m, i.e., $(\omega\tau_m) \leq 1$. The exponent α_m stretches relaxation over a wide frequency range.

Values of material parameters can be obtained from [22] and, by substituting values in Eq. (2.2), complex relative permittivity ε_r' can be calculated at any frequency ω for various human body tissues [23].

Relative permittivity and conductivity are fundamental parameters for calculation of another key parameter, skin depth. Skin depth (δ) of a material is defined as a measure of the distance over which the field falls by 1/e (approximately 37%) of its original value. Mathematically, skin depth for conductors can be calculated by [24]:

$$\delta = \frac{1}{\sqrt{\pi\mu f\sigma}} \quad . \tag{2.3}$$

where μ denotes permeability of the material, f denotes the frequency of operation, and σ denotes conductivity of the material.

Intensity of the electric field of a wave propagating at a point spaced by r meters from the wave source decays exponentially inside the body which is considered as lossy dielectric [24]:

$$E(r) = E_0 e^{-jk.r} \quad . \tag{2.4}$$

where k is the wavenumber of the conducting medium, found from [25]:

$$k = \beta + j\alpha = \frac{2\pi}{\lambda} + j\alpha \quad . \tag{2.5}$$

where β denotes the phase constant, α denotes the attenuation constant, and λ denotes the wavelength of waveform propagating in the medium. When the medium is not free space, the effective wavelength should be considered instead of the free-space wavelength in Eq. (2.5). In fact, the effective wavelength becomes shorter due to propagation over a lossy medium, shown by [26]:

$$\lambda_{eff} = \frac{\lambda_0}{Re\left[\sqrt{\varepsilon_{eff} - j\frac{\sigma_{eff}}{\omega\varepsilon_0}}\right]} \quad . \tag{2.6}$$

An important result derived from skin depth is penetration depth (δ_p), defined as the distance over which power of the wave decays to $1/e^2$, or approximately 13% of its surface value [26]:

$$\delta_p = \frac{1}{\alpha} \quad . \tag{2.7}$$

where α denotes the propagation attenuation. Penetration depth is inversely related to attenuation and the expression to find the attenuation factor (α) of a wave propagating in a certain tissue is [26]:

$$\alpha = \omega \sqrt{\frac{\mu\varepsilon_r\varepsilon_0}{2}\left[\sqrt{1 + \left(\frac{\sigma}{\omega\varepsilon_r\varepsilon_0}\right)^2} - 1\right]} \quad . \tag{2.8}$$

where $\mu \approx \mu_0$ is permeability of the tissue that is approximately equal to the permeability of free space.

In the far-field for unbounded media, intensity of the electric field of wave at distance d from the wave source propagating away from the body in general decays inversely proportional to the square of distance. That is,

$$|E|^2 \propto d^{-2} \quad . \tag{2.9}$$

Another essential parameter of a material is its dielectric loss. This parameter quantifies a dielectric material's inherent dissipation of electromagnetic energy into heat. Dielectric loss is typically parameterized in terms of the loss tangent ($\tan \delta$). The loss tangent can be calculated from [24]:

$$\tan \delta = \frac{\omega \varepsilon'' + \sigma_{eff}}{\omega \varepsilon'} \quad . \tag{2.10}$$

2.1.1.2 Loss in various Tissues

Table 2.1 presents measured examples where the conductivity and real part of relative permittivity are found from the Cole-Cole model in Eq. (2.2) and penetration depth and loss tangent formulas shown in Eq. (2.7) and Eq. (2.10), respectively for human tissues at 2.45 GHz.

Table 2.1 Electromagnetic Properties of Human Tissues at 2.45 GHz [22]

Tissue Name	*Conductivity [S/m]*	*Relative Permittivity*	*Loss Tangent*	*Penetration Depth [m]*
Aorta	1.467	42.47	0.24837	0.023761
Bladder	0.69816	17.975	0.27927	0.032545
Blood	2.5878	58.181	0.31981	0.015842
Bone, Cancellous	0.82286	18.491	0.31996	0.028087
Bone, Cortical	0.40411	11.352	0.25597	0.044616
Brain, Gray Matter	1.843	48.83	0.27137	0.02031
Breast Fat	0.14067	5.137	0.1969	0.085942
Cartilage	1.7949	38.663	0.3338	0.018638
Cerebro Spinal Fluid	3.5041	66.168	0.38078	0.012537
Cornea	2.3325	51.533	0.32544	0.016548
Eye Sclera	2.0702	52.558	0.28321	0.018773
Fat	0.10672	5.2749	0.14547	0.11455
Gall Bladder Bile	2.8447	68.305	0.29945	0.015592
Heart	2.2968	54.711	0.30185	0.017286
Kidney	2.4694	52.63	0.33736	0.015811
Liver	1.7198	42.952	0.2879	0.020434
Lung, Inflated	0.81828	20.444	0.28779	0.02963
Muscle	1.773	52.668	0.24205	0.021886
Skin, Dry	1.4876	37.952	0.28184	0.022198
Skin, Wet	23.984	20.369	0.84665	0.0010736
Small Intestine	3.2132	54.324	0.42529	0.012438
Stomach	2.2546	62.078	0.26114	0.018707
Testis	2.2084	57.472	0.27628	0.018394
Tongue	1.8396	52.558	0.25167	0.021083

As shown in Table 2.1, conductivity of certain tissues is dramatically higher than the conductivity of other tissues. For example, conductivity of wet skin is approximately 16 times higher than conductivity of dry skin. Below the skin layer, conductivity of fat is very low compared to conductivity of muscle tissue because muscle has high water content compared to fat.

Body tissues with high water content, such as skin and muscle, tend to be better conductors as demonstrated in the conductivity σ of material ($\sigma = \omega\varepsilon_0\,\varepsilon''$). This degrades the communication link by introducing losses that increase with increasing frequency. Hence,

medical devices inside the body use lower frequency because the penetration depth is better. For 2.45 GHz systems, penetration depth for muscle tissue is only 53% of the value at 915 MHz. Indeed, the newest allocation for in-body devices is in the 400 MHz band to address this issue.

2.1.1.3 Specific Absorption Rate

In order to measure electromagnetic absorption by a certain phantom or material, parameters that can quantify the amount of absorption must be defined. The first parameter, the Specific Absorption Rate (SAR), can be defined as the quantity of power from an electromagnetic wave absorbed per unit mass by an absorber, such as human body tissues. Mathematically, SAR can be defined in Eq. (2.11), where P_{abs} is power absorbed by the body and m is body mass:

$$SAR = \frac{P_{abs}}{m} \quad . \tag{2.11}$$

SAR is measured in Watts per kilogram or mWatt in milligram. The exposure limits in the United States are defined by the FCC [27] and are based on recommendations from the Institute of Electrical and Electronics Engineers (IEEE) [28] and the National Council on Radiation Protection and Measurements (NCRP) [29]. In Europe, however, most countries set exposure limits based on recommendations from the International Committee on Nonionizing Radiation Protection (ICNIRP) [30].

The ICNIRP has set certain exposure limits, including a Whole-Body SAR (WBSAR) limit for public exposure of 0.08 W/kg and localized limits over 10g and 1g of flesh including a set of frequency-dependent reference levels of power density to ensure compliance with ICNIRP or FCC exposure limits. The maximum SAR exposure values that are allowed for mobile devices between 100 KHz and 6 GHz in the United States and Europe are summarized in Table 2.2.

Table 2.2 Exposure Limits in terms of the Specific Absorption Rate, from [28], [29], [30]

	US exposure limit	European exposure limit
Whole-body average	$< 0.08\ W/kg$ averaged over 1 gram	$< 0.08\ W/kg$ averaged over 10 grams
Partial Body average	$\leq 1.6\ W/kg$ averaged over 1 gram	$\leq 2.0\ W/kg$ averaged over 10 grams

2.1.1.4 Literature review of electromagnetic wave interactions with human body

Researchers have studied absorption characteristics of electromagnetic waves on the human body [31]- [32]. One of the early works in this area is [31], in which the author investigated electromagnetic absorption in a multilayered slab model of tissue. The study concentrated on near-field exposure analysis, and calculations were made for 2,450 MHz. The paper examined resonant absorption caused by the layered slab model of the human body. Results showed that energy deposition for fields that are constant over a free-space wavelength is less than or equal to results obtained from plane-wave exposure, but it is greater than values obtained for a homogenous muscle slab model.

In [33], analytical derivations for EM energy absorption mechanism using numerical techniques are explained. The author utilized capabilities of the Method of Moments for this purpose by deriving integral equations. Resulting equations were transformed to a matrix equation, the matrix elements were evaluated, and the set of equations could be solved simultaneously.

In [34], the author studied the behavior of electric fields of small antennas placed near a dielectric half-space with sources operating at 900 MHz. Results showed that boundary conditions of electric near-fields can be applied to analysis of EM absorption in human tissue,

thereby allowing location of SAR maximums to be determined. This means that the peak SAR is not related to the antenna current as previously believed [35].

Other researchers have carried out analysis of layered body tissue in relation to absorption of EM waves by taking into account variation of parameters such as frequency range (from 236 to 5800 MHz), distance between the transmitter and the body, exposed location, and the layering effect of the body [36]. This paper claimed that two effects can significantly increase average SAR compared to SAR computed with tissue simulating liquid: standing wave effects in the analysis of far-field effects and enhanced coupling of reactive fields into fat tissue with low permittivity. In both cases, an increased SAR by 3 dB magnitude for biological tissue is found.

Recent research works have studied EM energy absorption in the human body caused by UWB antennas. For example, in [32], the authors thoroughly studied this problem for near-field scenarios suitable for body area networks. Results were compared for homogeneous and multilayer body models (skin, fat, and muscle) with varying degrees of thickness. Criteria used included peak 1-g SAR and peak SAR. Results showed that layered models always exhibit higher SAR than SAR for a homogeneous body model. For a specific UWB frequency, SAR increased as the distance between the antenna and the body decreased in the reactive near-field region due to having more fields' interaction with human body which results in more absorbed power. Moreover, the unaveraged SAR increased as the effective dielectric constant decreased. However, when the distance between the antenna and the body became larger ($d > \lambda/25$), standing waves emerged, thereby increasing SAR.

The literature, however, lacks necessary studies on absorption characteristics of EM waves on other types of dielectrics (with the exception of skin tissue). In fact, there is a need to

conduct a comprehensive study of WBANs used for special purposes, such as for astronauts, especially if significant transmitter power levels (e.g., > 1mW) are used.

2.2 Fundamentals of Radio Propagation Channels

The previous overview of electromagnetic properties of the human body and literature review is essential for deriving WBANs propagation behavior because the on-body radio channel is in proximity to the body's surface. This offers a good starting point to enable development of radio propagation models for WBANs.

2.2.1 Radio Channels for Free Space vs. for on-Body Communication

A radio link is typically categorized into three blocks: the transmitting antenna with transfer function $H_{T_x}(\omega)$, the radio channel with transfer function $H_{Ch}(\omega)$, and the receiving antenna with transfer function $H_{R_x}(\omega)$.

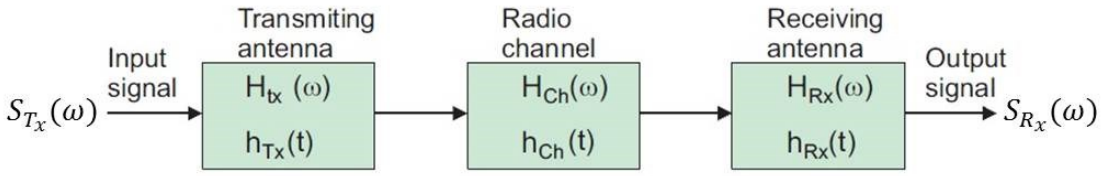

Figure 2.3 Block diagram representing the radio link.

The received signal $S_{R_x}(\omega)$ for the block diagram representing the radio link in Figure 2.3 can be obtained using the following formula [37]:

$$S_{R_x}(\omega) = S_{T_x}(\omega)H_{T_x}(\omega)H_{Ch}(\omega)H_{R_x}(\omega) \tag{2.12}$$

where $S_{T_x}(\omega)$ is the input signal. The path gain (PG), which equals the ratio of output power of receiving antenna ($P_r(\omega)$) to the transmit signal power ($P_t(\omega)$), can also be defined.

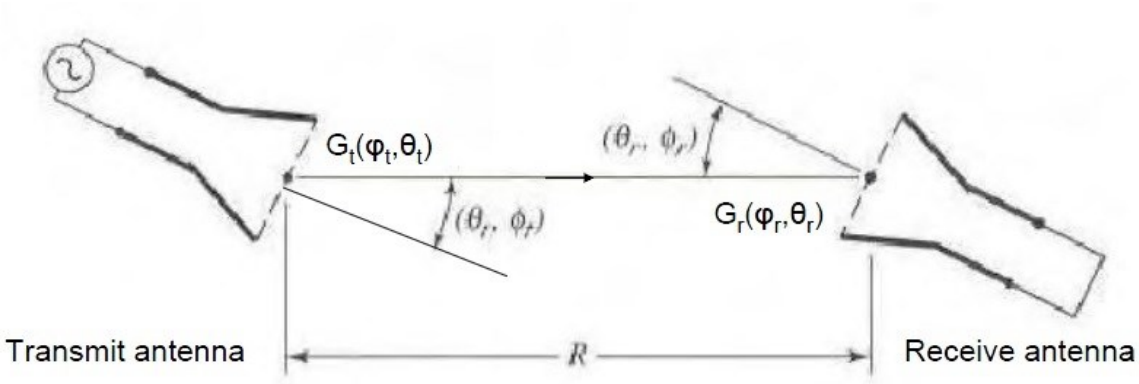

Figure 2.4 Geometrical orientation of transmitting and receiving antennas in Friss formula [37]

PG in free space between transmit and receive antenna shown in Figure 2.4 can be computed using the Friss transmission formula [37]:

$$PG = (1 - |\Gamma_t(\omega)|^2)G_t(\varphi_t, \theta_t)(1 - |\Gamma_r(\omega)|^2)G_r(\varphi_r, \theta_r)|\hat{\rho}_t(\omega).\hat{\rho}_r(\omega)|^2 P \quad (2.13)$$

where $P = \left(\frac{\lambda}{4\pi d}\right)^2$ is the propagation channel transfer function, d is the distance between transmitting and receiving antennas, $G_t(\varphi_t, \theta_t)$ is the realized gain of the transmitting antenna, $G_r(\varphi_r, \theta_r)$ is the realized gain of receiving antenna, Γ_t represents the reflection coefficient at the input of transmitting antenna, Γ_r is the reflection coefficient at the output of receiving antenna, $|\hat{\rho}_t(\omega).\hat{\rho}_r(\omega)|^2$ is the polarization matching factor between the transmitter and receiver antennas, and λ is the wavelength at the operating frequency. The path loss (inverse of path gain) is more commonly used.

Equation (2.13) is valid for a free-space environment and when the receiving antenna is placed at a point within the far-field propagation region. Therefore, Eq. (2.13) is not strictly accurate for body-centric communication. In this on-body propagation environment, the received electric field is a combination of free-space waves, field interactions with body parts, reflections from surrounding objects that can scatter signals, and creeping waves along the surface of the body.

In an intra-suit propagation environment, no reflections are present from the surrounding scatterers, but interactions with multiple layers of aluminized, radio opaque mylar are present. Behavior of antennas is more complex in this body centric environment. For example, the antenna input impedance and the antenna realized gain are functions of the position of the antenna on the body, distance from aluminized mylar material, and the antenna-body separation distance, respectively. Antenna polarization also plays a crucial role in the on-body radio channel. Investigation of these factors is a major focus of this dissertation, primarily within the context of the intra-suit environment.

Wearable on-body antennas for the more typical environment with aluminized mylar and their performance characteristics will be investigated at chapter 6, anticipating the development of future space suits which may use alternative TMG materials in their outer layers.

In the next subsection, we present the parameters that are generally used to compare the performance of antennas.

2.2.2 Narrowband Antenna Performance Parameters

2.2.2.1.1 Reflection Coefficient

It describes either the amplitude or the intensity of a reflected wave relative to an incident wave. The reflection coefficient can be given by the equation below, where Z_{in} is the input impedance of the antenna, Z_0 is the impedance of the port [37]:

$$\Gamma = \frac{Z_{in} - Z_0}{Z_{in} + Z_0} \tag{2.14}$$

The optimal value of reflection coefficient is when $|\Gamma|$ approaches zero which means that almost all of the incident power is radiated and no reflected power. Alternative metric is what is called the return loss (RL) and it can be calculated from the following formula [37]:

$$RL = -20log|\Gamma| \tag{2.15}$$

The optimal value of the return loss is when it approaches infinity.

2.2.2.1.2 Antenna Bandwidth

The impedance bandwidth of narrowband antennas is usually measured and it can be extracted from the S11 result. The impedance bandwidth is calculated for a certain return loss. Most common measure is the impedance bandwidth for a 10 dB return loss.

2.2.2.1.3 Antenna Resonant Frequency shift and Antenna Input Impedance

The resonance frequency detunes from the free space value when the antenna placed on the body. Frequency detuning occurs due to changes in the antenna effective length caused by the presence of the human lossy tissue. The presence of ground plane in antennas like patch antenna blocks the effects of the body on the antenna which results in minimal frequency detuning.

2.2.2.1.4 Antenna Radiation Efficiency

The radiation efficiency (e_{cd}) is a measure of the efficiency with which a radio antenna converts the radio-frequency power accepted at its terminals into radiated power. The total efficiency of antenna (e_0) incorporates the radiation efficiency and other factors as shown below [37]:

$$e_0 = e_r e_c e_d \tag{2.16}$$

where e_r is the reflection efficiency = $1 - |\Gamma|^2$

e_c is the conduction efficiency

e_d is the dielectric efficiency

The product of conduction efficiency and the dielectric efficiency produces the antenna radiation efficiency (e_{cd}). Thus, the total efficiency (e_0) can be rewritten in the following form [37]:

$$e_0 = e_{cd}(1 - |\Gamma|^2) \tag{2.17}$$

2.2.2.1.5 Realized Gain

First, we can define the antenna gain as the ratio of the power radiated to the power accepted by the antenna. However, the realized gain is the gain taking into account the reflection coefficient losses at the input of the antenna. In other words, the realized gain is the ratio of power radiated ($4\pi U$) to the input power of the antenna (P_{inc}) [37]

$$Gain = \frac{4\pi U}{P_{acc}} \tag{2.18}$$

$$Realized\ Gain = \frac{4\pi U}{P_{inc}} \tag{2.19}$$

where U denotes the radiation intensity in a certain direction and antenna directivity can be defined as the ratio of actual transmitted power in a particular direction to that which would be transmitted if the power radiated isotopically [37]:

$$Directivity = \frac{4\pi U}{P_{rad}} \tag{2.20}$$

where P_{inc} is the incident power, P_{acc} is the accepted power which equals $P_{acc} = P_{inc}(1 - S_{11}^2)$ P_{rad} is the radiated power which can be calculated from [37]:

$$P_{rad} = P_{acc}\ .\ Radiation\ Effieicncy \tag{2.21}$$

The realized gain can be measured in the azimuth plane (on-body direction) and vertical (off-body direction) plane.

2.2.2.1.6 Radiation Pattern

The radiation pattern defines the variation of the power radiated by an antenna as a function of the direction away from the antenna. To measure the 3D radiation pattern in 2D planes, two 2D planes are usually plotted; one for the elevation angle and another for the azimuth angle. It is usually measured/simulated for free space environment and on body case. The

radiation pattern is usually distorted by the presence of human body and hence the optimal design is the one which attempts to minimize this distortion.

2.2.2.1.7 Polarization

The polarization of an antenna is the polarization of the radiated fields produced by antenna, evaluated in the far-field. There are various types of antenna polarization namely, linear polarization, circular polarization and elliptical polarization. In general, if two linearly polarized antennas are rotated from each other by an angle $\emptyset$, the power loss due to this polarization mismatch is described by the Polarization Loss Factor (PLF) [37]:

$$PLF = cos^2\emptyset \tag{2.22}$$

2.2.3 Literature Review on On-Body Antennas

We can say that the parameters that control the narrowband antenna performance are the ground plane size, full or partial ground plane, antenna type and size, antenna-body separation and the locations of the body.

In the literature, many studies have been conducted to study the behavior of antennas located in proximity to the body tissues [38], [39], [40], [11] as well as on the specific absorption rate [41], [42]. Those studies show that antennas with full ground plane are minimally sensitive to human presence. In [43], a parametric study is presented to evaluate the how the antenna-body separation distance affects the antenna performance. It has been shown that the further the antenna from the body, the lower the absorption from the body. Also, using lossy material is useful to reduce the electromagnetic fields absorption by human body as significant part of the power is dissipated in the lossy material instead of body tissues.

There are two main requirements for on-body antennas: (1) optimally the antennas should be insensitive to the body effects and (2) the antenna should have a radiation pattern shape that

minimizes the channel loss [44]. Studies of body-worn antennas have recently gained significant attention [43], [45], [11], [41], [42], [46], [47], [48], [49].

The performance of 2.45 GHz narrowband on-body antennas is studied extensively in [50], [46]. The author found that for on-body communication, wire monopole antennas show good performance in terms of path loss since monopole antennas have omnidirectional radiation pattern in the horizontal/azimuth plane. In [48], a dual-band, 2.4 GHz, 5.2 GHz, button antenna is proposed for Wireless LAN applications. The size of this antenna is similar to that of a standard metal button used in jeans and can be easily attached to clothes. The antenna has a radiation pattern that is similar to that of monopole antenna in both frequency bands. More on-body antenna types include microstrip patch antenna [11], [51], planar monopole antenna [51], printed monopole [43], planar inverted-L antenna [51], [52], printed circular loop antenna [53], planar inverted-F antenna (PIFA).

To facilitate the integration of wireless devices into garments, wearable antennas are proposed. By definition, wearable antennas are antennas used for body-centric communications that are conformal to the human body and can be bent, stretched and deformed while maintaining relatively good performance. Textile wearable antennas are a class of wearable antennas and in the literature, textile antennas can be easily found [40], [54], [55], [56], [57], [58], [59] . In [58], a patch antenna designed to be integrated into protective clothing is introduced. The antenna is printed on a flexible pad of foam that is commonly used in protective clothing. Antennas that are printed above Electromagnetic Band Gap (EBG) structures are presented in [56], [55], [60] to reduce the effect of human body and minimize the frequency shift from the resonance frequency. In [56], a flexible dual-band (2.4 GHz and 5.5 GHz) patch antenna on an EBG textile substrate made of felt is proposed. The author claims that the radiation into the body is reduced by 10 dB

and the gain is improved by 3 dB after introducing the EBG material. However, the antenna is big (12 cm times 12 cm) which makes it impractical for human body area networks. Another type of antenna, textile PIFA is designed [59] and planned to be used for smart clothing applications.

2.2.4 Radio Channel Measurement Techniques

After briefly going over the principles of radio channel propagation, it is useful to preview the basic methods used to measure the radio channel since they will be heavily used in our study. First, it should be noted that the propagation simulation and measurement setups are typically classified into two categories; time-domain and frequency-domain measurements [61], [62]. Almost all radio propagation sounders rely on those two techniques to characterize the wideband radio channel for various propagation environments (e.g., indoor, outdoor, and body-centric communications) [63], [64]. In our work, we employ exclusively the frequency domain method. Figure 2.5 depicts the general setup for frequency-domain measurement.

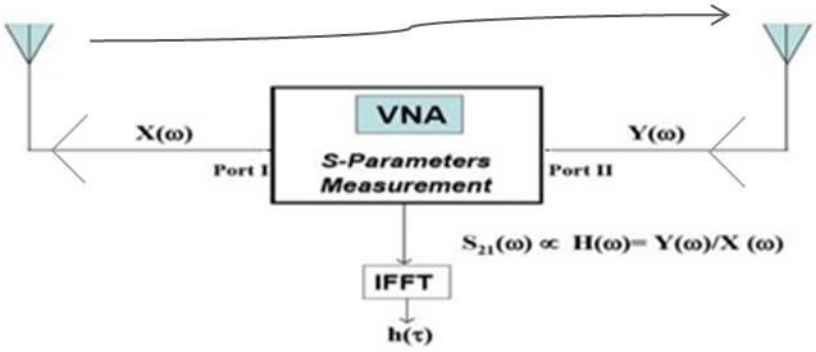

Figure 2.5 Frequency-domain Measurement Method for Indoor Communication [61]

Using a vector network analyzer (VNA) as shown in Figure 2.5, we can measure the forward transmission gain (S21) where ($X(\omega)$) is output at Port I through the transmit antenna and the received signal ($Y(\omega)$) is input to Port II. The frequency response of the channel can computed

from ($H(\omega) = (Y(\omega)/ (X(\omega))$) which is presented in Eq. (2.12). It should be noted that the overall frequency response includes the channel radio and the effects of the two antennas as well.

The frequency response for a sweep of discrete frequency points can be obtained using the network analyzer where the magnitude and phase of $H(\omega)$ can be displayed. If desired, the time-domain form of the channel can be computed as well by taking the Inverse Discrete Fourier Transform (IDFT) of $H(\omega)$. By first using low loss cables and then properly applying advanced calibration techniques, the losses introduced in the cable can mitigated.

Throughout our dissertation, we will use mainly the frequency-domain technique to characterize the radio channel and in particular the forward transmission gain $|S21|$ as the main criterion for the evaluating the channel performance. In some cases the network analyzer is avoided due to the difficulty of decoupling the antenna from the transmission line required in this setup. Instead, we rely on battery powered radios to provide the desired $|S21|$ magnitude information using a received signal strength indicator (RSSI) function in the receiver [8].

2.3 Modeling of Human Body for On-Body Applications

After going over the principles of radio channels and their measurement techniques, we consider phantoms used to represent the human body tissues. First, the physical phantoms are introduced and then the numerical phantoms used in electromagnetic simulations in later chapters are presented.

2.3.1 Physical Phantoms for Human Body

The aim of using a physical phantom is typically to have a physical model whose dielectric properties are quite similar to that of a real human body tissue. The physical phantom can be used to investigate the electromagnetic interaction with human tissues instead of using real subjects. Physical phantoms have been used for many applications; in medical research

(implantable devices, and for the diagnosis and treatment of certain diseases) and for mobile communications to ensure that the electromagnetic emission of cell phones are within the safety limits imposed by IEEE, for instance. More recently, physical phantoms have been used for body-worn devices to quantify the amount of electromagnetic absorption by the human body [44].

There are various types of phantoms depending on the desired frequency range, body tissue that the phantom is representing, homogenous or inhomogeneous tissues, and the state of the phantom which can be either solid, semi-solid (gel), or liquid. Each type of the phantom can be used for certain purpose. For example, liquid phantoms are typically used to measure the amount of specific absorption rate (SAR), where the electric field is measured inside the phantom using a probe and then the SAR can be calculated [65].

In this research, we are using low power transmitters (1mW) and the specific absorption rate is less than limit specified by IEEE as shown in Table 2.2. Therefore, we believe that it is more accurate and more meaningful to use the on-body devices/antennas with real human subjects. All subjects were adults and enrolled at the Department of Electrical and Computer Engineering at Kansas State University at the time of conducting experiments.

2.3.2 Numerical Phantoms for Simulation Study

3D EM simulation is also used extensively in this work to allow for understanding and visualization of fields as well or an alternate method of studying the propagation losses in the suit. Models composed of cylindrical/rectangular/cubical shapes are used to gain initial insights while models with more complex geometries simulating the shapes and thickness of real human body tissues are used for more accurate simulation results. An example of this model is what is called HUGO Human Body Model displayed in Figure 2.6 (right) which is composed of many

voxels [66]. The parts of the body and tissues are modeled using the dielectric properties discussed earlier (i.e., relative permittivity, conductivity, loss tangent, etc) depending on the method of insertion. For instance, for Debye-Drude model, the conductivity, static relative permittivity, infinite relative permittivity, number of poles and relaxation time are required. Such highly accurate models are available and can be easily imported into the simulation domain of EM simulators.

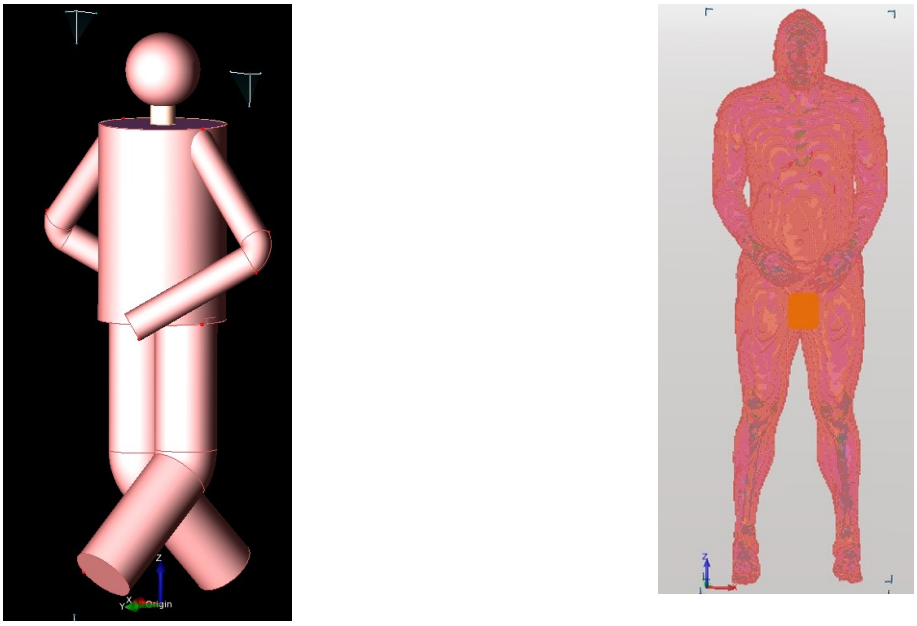

Figure 2.6 (left) Simplified Cylindrical Human Body Model, (right) HUGO Model in EMPro Simulator, Keysight Technologies

2.4 Numerical Modeling of Electromagnetic Problems

Throughout this research work, we use 3D EM simulation to study the radio channel inside space suits. This unique 3D propagation structure is complex in nature, and thus closed-form or analytical solutions can be very complicated and impractical. Numerical techniques can provide a physical insight into the propagation structure with reasonably accurate results. We use two common computational algorithms, namely Finite-Difference Time-Domain (FDTD) and Finite-Element Method (FEM). These algorithms have applications in many physical, chemical,

and biological phenomena in diverse areas such as fluid dynamics, material science, economy, financial modelling and electromagnetism. We will use these methods in the context of electric and magnetic field simulations.

In the following subsections, we provide a brief description of both algorithms and then a comparison of their performance in the context of electromagnetic problems involving human body and small antennas. Detailed mathematical derivations of electric and magnetic solutions using FDTD and FEM methods can be seen in any computational electromagnetics book [67].

2.4.1 Fundamentals of the FDTD Method

Finite-Difference Time-Domain technique employs finite differences as approximations to both the temporal and spatial derivatives which appear in Maxwell equations (particularly Ampere's and Faraday's laws) [68]. The FDTD algorithm was first proposed by Kane Yee in 1996 utilizing second-order difference equations.

FDTD divides both time and space into discrete segments. In particular, we divide the 3D space into cells with rectangular shape which are small compared to the shortest wavelength of the simulation domain. After division, the electric field components are positioned on the edges of the box whereas the magnetic fields are located on the faces as illustrated in Figure 2.7. This form of fields with this orientation is known as Yee cell and it is the basic element of FDTD algorithm. Time is divided into small steps such that each step represents the time required for field to pass from one cell to another.

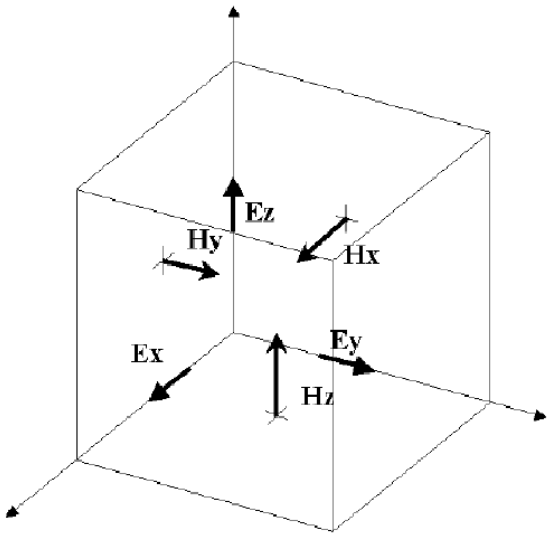

Figure 2.7 Yee Cell labeled Field Components [68]

With many FDTD cells combined together, the three-dimensional volume formed is called FDTD grid or mesh. Each cell will overlap the edges and faces with its neighbors, thus each cell will have three electric field components that start at a common node associated with it. However, the electric field at the other nine edges of the FDTD cell will belong to the other adjacent cells. The same thing applies to the magnetic fields where three components are originating on the faces of the cell adjacent to the common node of the electric fields.

The general procedure to solve electric and magnetic fields using FDTD method is as follows:

1) We modify the equations of Ampere's and Faraday's laws from their derivative form to their finite difference equations.
2) Then, we solve the resulted difference equations to get what can be called "update equations" that express the future fields in terms of their past fields using time domain.

3) After that, we compute the electric and magnetic fields one time-step into the future.
4) We repeat the previous step for both the electric and magnetic fields until the fields are obtained for the desired time duration.

The previous procedure works for a one-dimensional space domain. For a three-dimensional EM domain, we solve the electric and magnetic fields in a similar manner where the field solutions are expressed using three variables; x, y, and z in three difference equations instead of one variable.

The maximum time-step for stable computational operations is bounded by the following equation [68]:

$$\Delta t_{max} \leq \frac{1}{c\sqrt{\frac{1}{(\Delta x)^2}+\frac{1}{(\Delta y)^2}+\frac{1}{(\Delta z)^2}}} \quad . \tag{2.23}$$

where c denotes the maximum speed of wavelength for all materials in the simulation domain, Δt_{max} the maximum time step, and Δx, Δy, Δz the lengths of the cell sides in meters.

Common applications of the Yee algorithm including scattering problems or antenna analysis and theoretically requires an unbounded simulation space to obtain accurate simulation. However, since the computational resources of practical computers are limited, the computation domain is usually truncated with what is called an absorbing boundary condition (ABC). This boundary condition simulates the propagation behavior of open space in which the waves are allowed to propagate outside the simulation domain and there are no reflected waves. However, practically, there will be some reflected waves but they can be minimized if the size of boundary box is large compared to the wavelength (e.g., multiples of wavelengths). In all the simulations presented in this dissertation, a computational absorbing boundary condition called Perfect Matched Layer (PML) with seven layers has been adopted.

2.4.2 Fundamentals of the FEM Method

The finite element method divides the full simulation space into a number of smaller regions (the so called elements) and represents the fields in each element by a focal function [69]. Each region is a triangle in 2D space and a tetrahedron in 3D space. The value of a vector quantity which can be either an E-field or H-field at points inside each tetrahedron is interpolated from the vertices of the tetrahedron.

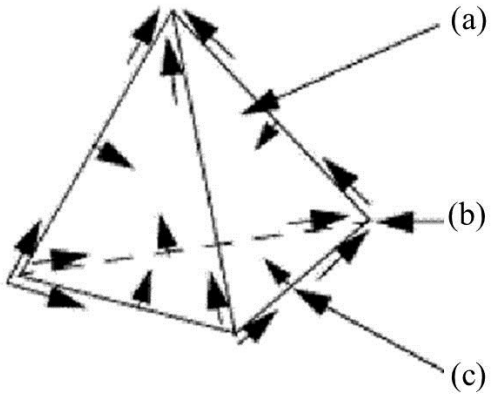

Figure 2.8 Field Quantities are interpolations of the Nodal Values in 3D space [69]

Figure 2.8 shows the field components of a tetrahedron where the components are classified as: (a) the components of a field that are tangential to the edges of an element are stored at the vertices, (b) the component of a field that is tangential to the face of an element and perpendicular to an edge is explicitly stored at the midpoint of the selected edges, and (c) the component of field at a point inside the tetrahedron can be computed as the interpolation of the nodal values. Using this method of representing vector fields, we can change the conventional form of Maxwell's equations into a matrix form where the matrix can be solved easily using common numerical methods.

The matrix can be solved either directly or iteratively. In the case of a direct solution, the convergence to a solution is guaranteed if the FEM settings are properly adjusted. However, this

consumes extensive memory resources, especially when the structure is in a three-dimensional volume. In the case of iterative solutions, memory usage is not a concern since the solver stores only the last values in each iteration. In contrast to the direct solver, the iterative technique does not guarantee convergence to a solution. Overall, the choice of selecting the appropriate way depends on the available resources and desired speed of obtaining a solution.

For solutions involving excitation ports, the procedure to calculate the S-Parameter matrix can be summarized in the following steps:

1) First, the structure is divided into a finite element mesh (tetrahedral)

2) The electromagnetic waves on each port of the structure are computed.

3) Assuming that each of the ports is excited by one of waves, we compute the full electromagnetic field inside the structure.

4) Lastly, we can compute the generalized S-Parameter matrix using the values of transmission and reflection occurring.

2.4.3 Comparison between FDTD vs. FEM: Pros and Cons.

The FDTD can be easily applied to the modelling of inhomogeneous structures, and it has the big advantage of having an O(N) computing complexity, while the FEM is more complex and time-consuming (O(N^2) complexity). In addition, FDTD is a time domain method which enables obtaining wideband results using a single simulation run.

However, FDTD has some shortcomings. First, the whole simulation domain needs to be meshed into small cells compared to wavelength and simulated, thus the simulation time and memory usage rise quite rapidly.

In the context of on-body communications where an electrically very large object is typically used, this may require the use of parallel computers. In addition, when there is a need to

analyze sharp edges of a structure, we need to have very fine mesh and small time-step to accurately model the edge, which increases the computational time dramatically.

Despite these problems, in the literature, it can be seen that FDTD method has been extensively used to study the effect of human body in the electromagnetic radiation. This method is the most suitable technique for modeling the EM wave propagation inside and on the human body. In fact, FDTD has been adopted to study the specific absorption rate (SAR) for mobile communications [70]. Also, the FDTD method has been commonly utilized to investigate both the electromagnetic radiation of implanted devices inside the human body [71], [72], and the performance of on-body antennas [73]. In [74], a dispersive FDTD method is developed for use with inhomogeneous structures and dispersive materials where their dielectric properties vary as a function of frequency.

When using small antennas for on-body radio wireless links, very fine grid settings are needed to get high spatial resolution which in turn increases the computation time and memory utilization especially if uniform mesh settings are used. In contrast, if non-uniform mesh and subgriding schemes are applied, it may produce incorrect solutions or show unstable sub-gridding scheme [75]. Finite Element Method (FEM) method may be regarded in such situations.

As mentioned earlier, FEM decomposes the structure into a set of elements called tetrahedral which are suitable for modelling curved structures. Despite its advantages, FEM has some drawbacks as mentioned earlier, such as the high computational complexity.

In the simulations utilized in this study, both FDTD and FEM solvers are used. When characterizing the performance of antenna is needed, FEM is mostly used due to its convenience for general antenna simulation and fitting the antennas with curved structures.

2.5 Chapter Summary

This chapter included a review of the concepts of dielectric properties of common human body tissues and their variations for a range of frequencies. Fundamental concepts typically used in studying electromagnetic energy interaction with human body were also presented. Then, we moved on to review the principles of radio channel modeling in free space and in general body-centric communication channels. Next, the typical physical and numerical phantoms used in modeling electromagnetic problems in the context of body-centric wireless communications are presented.

This chapter also outlined the advantages and disadvantages of two common numerical algorithms used to solve electric and magnetic fields in structures with three-dimensional volume. Both algorithms are alternatively used in simulation studies presented in the following chapters.

Chapter 3 - Shielding in Space Suits

Successful design and implementation of a WBAN inside a space suit requires knowledge of the wireless propagation environment within the suit. This chapter first details the structure of an extravehicular mobility unit (EMU) space suit. This suit has been in use for a long time and is especially useful for short-term missions (e.g., international space station (ISS) missions). Although other space suits are under development, particularly for long-term missions, materials in those suits may differ but their shielding properties are largely expected to be the same.

Understanding the shielding properties of space suit materials is crucial for characterizing intra-space suit propagation environment. Therefore, this chapter highlights the basics of metal surface shielding for various materials using plane wave and near-field shielding principles. A preliminary analytical study is conducted using simplifying assumptions in order to quantify the insights and shielding effectiveness of space suit materials. Results of analytical calculation are verified using laboratory experiments.

3.1 EMU Space Suit Structure

EMU space suits, commonly used by the National Aeronautics and Space Agency (NASA), are composed of a cooling and ventilation garment (CVG) liner, liquid CVG (LCVG) water transport, pressure bladder, and thermal micrometeoroid garment (TMG) cover layers, as illustrated in Figure 3.1. The outermost TMG segment includes multiple metallic layers of aluminized mylar. These layers are radio opaque at ultra-high frequency (UHF) and above due to metallization thickness in the range of 500 nm to 1000 nm for each layer. The number of TMG layer varies from five to seven depending on the segment of space suit.

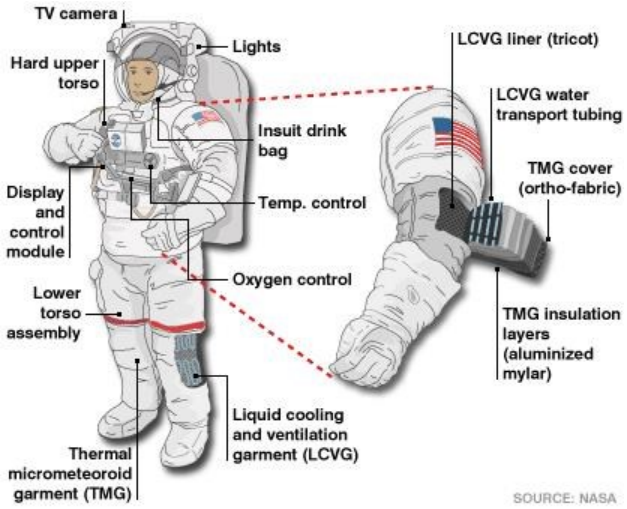

Figure 3.1 EMU space suit structure [76]

In this study, experiments are conducted on a space suit to understand the propagation environment and develop propagation models. However, conducting experiments on a real space suit at NASA space centers is not feasible because of lack of time and access. Therefore, a section of an EMU space suit (Figure 3.2) was obtained from the primary manufacturer (ILC Dover, Inc) to build a space suit mockup with electrical properties similar to properties of a real space suit. The space suit mockup was built at Kansas State University's Department of Apparel, Textiles, and Interior Design. As shown in Figure 3.3, various design stages primarily incorporated copper fabric (Pure Copper Polyester Taffeta Fabric [77]). First, electrical properties of the space suit mockup are compared to that of a section of EMU space suit (shown in Figure 3.2). Results show that electrical properties of the space suit mockup are fairly similar to properties of the real EMU suit[1], specifically 0.05 Ohms per square surface resistivity and

[1] It is important to note that various TMG layer materials may have various aluminum thicknesses, since the goal is only to reflect infrared energy, not radio waves. A system designer should measure actual suit materials and consider the type of antennas used before assuming strong radio-opacity.

through-suit attenuation of at least 40 dB, indicating that the mockup suit is almost radio opaque at UHF.

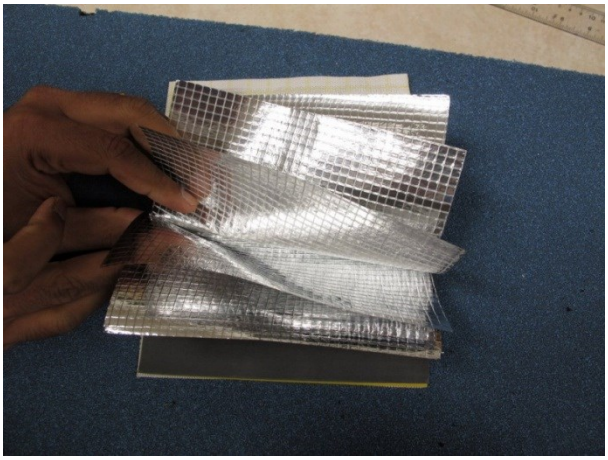

Figure 3.2 Multiple aluminized mylar in a section of EMU space suit from ILC Dover, Inc

The construction process of individual space suit sections and the final space suit mockup is demonstrated in Figure 3.3[2]. Figure 3.3 (left) shows copper fabric being sewed to build segments of space suit mock up according to the drawings shown. After all space suit segments are built and assembled, the final suit is worn by a subject with average height and weight as illustrated in Figure 3.3 (right).

[2] Spacesuit mockup was designed and built by Erin Monfort-Nelson, Department of Apparel, Textiles, and Interior Design, Kansas State University, 2012.

Figure 3.3 Construction of KSU space suit

Highlighting electrical properties of common conductive metallic surfaces, particularly materials used in the EMU space suit, is beneficial in the context of intra-space suit characterization. Therefore, in the following section, we briefly review two basic approaches for evaluating the shielding effectiveness for different waveforms. Then, a simple analytical study is conducted to obtain insights into the shielding properties at DC and low frequencies. Finally, we verify the analytical results against results of laboratory measurements.

3.2 Basic Principles of Shielding

The shielding effectiveness parameter (SE) is commonly used to quantify shielding of any conductive surface. Shielding effectiveness of a surface can be defined as the ratio of field magnitude (electric or magnetic) without placing a conductor surface to field magnitude with conductor surface placed.

Shielding effectiveness is typically a function of distance between the source of incident wave and the location of the shielded surface. Therefore, the shielding investigation is divided into far-field or near-field wave source [78]. A plane wave typically represents the far-field case,

whereas a near-field source has a more complex electric or magnetic field structure and thus will be discussed separately.

3.2.1 Uniform Plane Wave Shielding Effectiveness

In this case, the shield is first assumed to be planar with certain thickness (th), as shown in Figure 3.4.

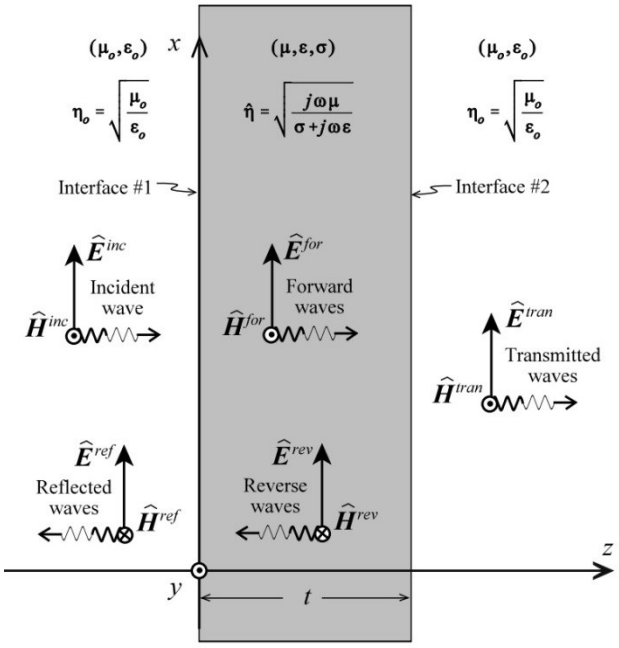

Figure 3.4 Electric and magnetic field components for an incident wave, taken from [78]

Shielding effectiveness in dB scale (SE_{dB}) in plane wave case consists of three distinct components: (1) shielding effectiveness due to reflection loss (R), (2) shielding effectiveness due to multiple reflections (M), and (3) shielding effectiveness due to absorption loss (A). Mathematically, SE_{dB} expressed in dB scale has the following form [78]:

$$SE_{dB} = R_{dB} + M_{dB} + A_{dB} \tag{3.1}$$

where each component can be calculated via [78]:

$$R_{dB} = 20\log_{10}\left|\frac{(\eta_0+\hat{\eta})^2}{4\eta_0\hat{\eta}}\right| \tag{3.2}$$

$$M_{dB} = 20\log_{10}\left|1 - \hat{\Gamma}_{a-c}^{2} e^{-2th/\delta} e^{-j2\beta.th}\right| \tag{3.3}$$

$$A_{dB} = 20\log_{10} e^{th/\delta} \quad . \tag{3.4}$$

Here, $\hat{\Gamma}_{a-c}$ denotes the reflection coefficient for waves moving from air into the conductor; th denotes the shield thickness; δ denotes the skin depth of the shield at certain frequency ω; and β denotes the phase constant. The reflection coefficient for waves transitioning from the conductor into air ($\hat{\Gamma}_{c-a}$) corresponds to [78]:

$$\hat{\Gamma}_{c-a} = \frac{\eta_0 - \hat{\eta}}{\eta_0 + \hat{\eta}} \tag{3.5}$$

where $\hat{\eta}$ is the intrinsic impedance of the conductor. $\hat{\eta}$ is frequency-dependent and can be calculated using [78]:

$$\hat{\eta} = \sqrt{\frac{j\omega\mu}{\sigma + j\omega\varepsilon}} \quad . \tag{3.6}$$

Here, σ denotes the conductivity of the shield, μ denotes the permeability of the shield, and ε denotes the permittivity of the shield. For a good conductor with shield thickness that is multiple orders of skin depth, M_{dB} is not negligible and must be included in the calculation of shielding effectiveness. On the other hand, for a thin shield with good conductivity and thickness that is comparable to one skin depth, the value of component M_{dB} is negligible compared to reflection loss (R_{dB}) and absorption (A_{dB}) loss.

3.2.2 Near-Field Shielding Effectiveness

For near-field source, calculating shielding effectiveness is more complicated than that of plain wave because of its complex electric and/or magnetic fields behaviors. In near-field problems, it is important to consider electric field and magnetic field sources as discussed in the following subsections.

3.2.2.1 Electric field-based sources

Electric field sources act as a superposition of Hertzian dipoles. Wave impedances for this source are given as [78]:

$$\hat{Z}_{we} = \frac{\hat{E}_\Theta}{\hat{H}_\varphi} = \eta_0 \frac{j/\beta_0 r + 1/(\beta_0 r)^2 - j/(\beta_0 r)^3}{j/\beta_0 r + 1/(\beta_0 r)^2} \ , \tag{3.7}$$

where $\hat{E}_\Theta$ and $\hat{H}_\varphi$ denote the magnitude of electric and magnetic field of the incoming wave, respectively, r denotes distance from the source and β_0 denotes the phase constant of the wave in free space. The electric field is dominant in the near-field of a Hertizan dipole.

3.2.2.2 Magnetic Field-Based Sources

The magnetic field source acts as a superposition of small loops. Wave impedances for this source correspond to [78]:

$$\hat{Z}_{wm} = \frac{\hat{E}_\varphi}{\hat{H}_\Theta} = -\eta_0 \frac{j/\beta_0 r + 1/(\beta_0 r)^2}{j/\beta_0 r + 1/(\beta_0 r)^2 - j/(\beta_0 r)^3} \ . \tag{3.8}$$

The magnetic field is dominant in the near-field of a small loop and wave impedances for both sources in Eq. (3.7) and Eq. (3.8) approximate η_0 in the far-field.

The near-field shielding effectiveness for electric and magnetic field sources can be calculated by substituting the respective impedance values into the shielding effectiveness equations (3.1-3.6).

By substituting the respective wave impedance into the far-field shielding effectiveness components produces the near-field shielding effectiveness value. It should be noted that only the reflection loss and multiple reflection losses are functions of the wave impedance whereas the absorption loss component A_{dB} does not change and thus can be calculated using Eq. (3.4). For electric-field based sources, the two individual terms constituting the shielding effectiveness are [78]:

$$R_{dB} = 20\log_{10}\left|\frac{(\hat{Z}_{we}+\hat{\eta})^2}{4\hat{Z}_{we}\hat{\eta}}\right| \tag{3.9}$$

$$M_{dB} = 20\log_{10}\left|1-\left(\frac{(\hat{Z}_{we}-\hat{\eta})}{(\hat{Z}_{we}+\hat{\eta})}\right)^2 e^{-2th/\delta}e^{-j2\beta.th}\right| \tag{3.10}$$

For magnetic field sources, the reflection loss (R_{dB}) and multiple reflections loss (M_{dB}) correspond to [78]:

$$R_{dB} = 20\log_{10}\left|\frac{(\hat{Z}_{wm}+\hat{\eta})^2}{4\hat{Z}_{wm}\hat{\eta}}\right| \tag{3.11}$$

$$M_{dB} = 20\log_{10}\left|1-\left(\frac{(\hat{Z}_{wm}-\hat{\eta})}{(\hat{Z}_{wm}+\hat{\eta})}\right)^2 e^{-2th/\delta}e^{-j2.\beta.th}\right| \tag{3.12}$$

In the following section, the shielding effectiveness of common conductive fabrics is evaluated based on the principles of Faraday's Law of Induction.

3.3 Near-Field Shielding: Analysis and Measurements

3.3.1 Analysis

The exact theoretical analysis of the shielding due to space suit materials is complicated. In order to develop some basic intuition on shielding behavior of space suits, we resort to simplifying assumptions that can lead to a tractable analysis. Consider a source in the form of a circular loop with one turn and diameter a and a receiving loop is located at a very close distance to the transmitter, as shown in Figure 3.5.

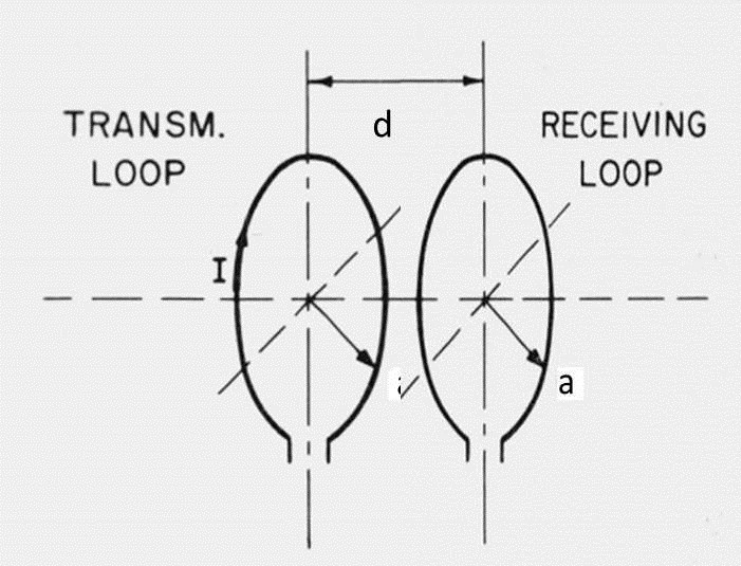

Figure 3.5 Transmit and receive loops

The transmitting loop, which has a current source when flowing, creates a time-varying magnetic field according to Faraday's Law of Induction. The magnetic field passes through a receive loop embedded within a sheet and both the loop and the receive loop have thickness (*th*), creating Eddy currents in closed curves because voltage induced in the sheet creates a current with certain density as represented in Figure 3.6.

Current density can be represented by the width of current flow in which most char, I es are concentrated. Current direction opposes change in the magnetic field in the source loop.

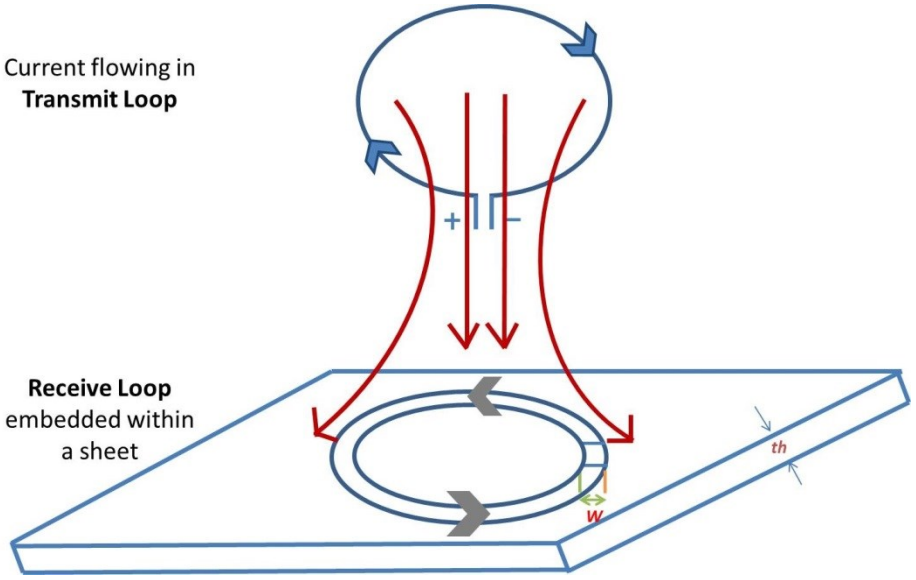

Figure 3.6 Transmit loop and receive loop embeded within a sheet with thickness *th*

To calculate magnetic field induced by all current elements, contributions from all current elements with length dY have to be considered resulting in the following expression [79]

$$B_{induced} = \frac{\mu_0 I a}{4\pi} \int_{-\infty}^{\infty} \frac{dY}{(Y^2+a^2)^{3/2}} \quad , \tag{3.13}$$

Here, μ_0 denotes the permeability of free space; I denotes the current flowing into the wire, a denotes the radius of the loop, and Y is the length of the current flowing.

The goal of this simplified study is to quantify the percentage of electromagnetic shielding as a function of the frequency of the source current waveform.

The following presents shielding effectiveness of a thin sheet at DC and then at low frequencies.

The general procedure involves the indirect evaluation of shielding effectiveness by calculating the percentage of forward current compared to transmitted current.

1) Using Biot-Savart Law to obtain B at center of receiving loop:

As shown in Figure 3.7, a magnetic field is created due to current flowing in a straight wire. Consider a point $\vec{B}$ located at horizontal distance (a) and zero on the vertical distance from the origin, with coordinates (a, o).

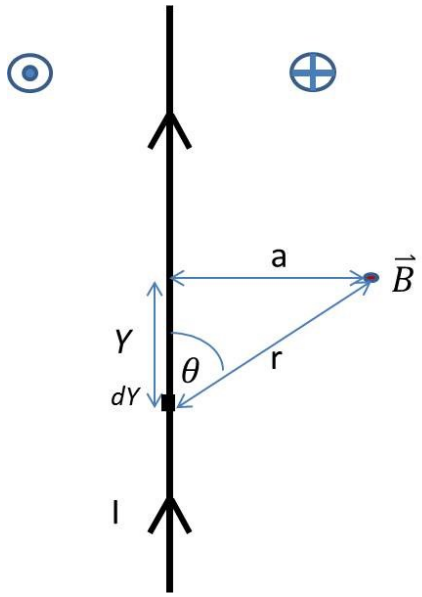

Figure 3.7 Magnetic field calculation due to infinitesimal current element *dY*

The direction of induced magnetic field due to the current flow in the wire can be determined using the right-hand rule in which the thumb refers to the direction of current and the forefinger refers to the direction of magnetic field, as illustrated in Figure 3.7. The induced magnetic field at the location (a, o). can be obtained using [80]:

$$dB_{induced} = \frac{\mu_0}{4\pi} \frac{I\, dY\, \sin\Theta}{r^2} \quad . \tag{3.14}$$

In Eq. (3.14), dY, Θ, and r vary for each current element selected on the vertical axis, r can be substituted in terms of Y and a where $r = \sqrt{y^2 + a^2}$ and $\sin\Theta = {}^{a}/_{(Y^2 + a^2)^{1}/_{2}}$ [80]. That is,

$$dB_{induced} = \frac{\mu_0}{4\pi} \frac{I\, dY\, a}{(Y^2+a^2)(Y^2+a^2)^{1}/_{2}} \tag{3.15}$$

$$dB_{induced} = \frac{\mu_0}{4\pi} \frac{I\, dY \sin\theta}{(Y^2+a^2)^{3/2}} . \tag{3.16}$$

To calculate magnetic field induced by all current elements, contributions from all current elements with length dY can be summed to yield [80]

$$B_{induced} = \frac{\mu_0 Ia}{4\pi} \int_{-\infty}^{\infty} \frac{dY}{(Y^2+a^2)^{3/2}} . \tag{3.17}$$

To compute the magnetic field at the center of the receiving loop with one turn, as shown in Figure 3.8, the following analysis can be followed:

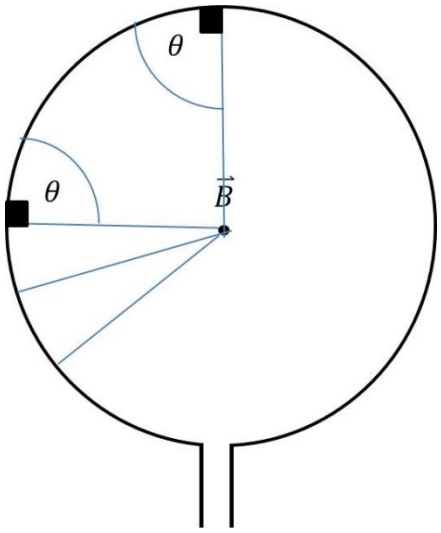

Figure 3.8 Magnetic field calculation at the center of the circular loop

In Figure 3.8, angle Θ is always equal to 90 degrees because the projected line from the center to any point in the circumference is perpendicular to that point. Therefore, $\sin\Theta$ equals 1. Using Biot-Savart Law, the result of integration is [80]

$$B = \frac{\mu_0 I(t)}{4\pi a^2} \oint dL = \frac{\mu_0 I(t)}{4\pi a^2} 2\pi a = \frac{\mu_0 I(t)}{2a} = \frac{\mu_0 I(t)}{D} \tag{3.18}$$

where current $I(t)$ is assumed to be sinusoidal for simplicity, $I(t) = I_0 \sin 2\pi f t$, and D denotes the diameter of the loop. This calculation of $B_{induced}$ is an approximation that is valid only if the receiver loop is very close to the transmitter (i.e., less than a; one radius of the loop).

2) **Assume the magnetic field calculated in Step (1) is approximately equal throughout the area of the source loop:**

This implies that the magnetic field strength is uniformly distributed over the area of loop.

3) **Assume the sheet for which the shielding effectiveness is to be calculated close to the source loop:** This implies that the magnitude of induced magnetic ($B_{induced}$) in the sheet approximately equal to the magnetic field (B) in Eq. (3.17)). That is, the magnetic field in the sheet can be written as:

$$B_{sheet} \cong B = \frac{\mu_0 I(t)}{D} = \frac{\mu_0}{D} I_0 \sin 2\pi f t \quad . \tag{3.19}$$

4) **Use Faraday's Law to obtain electromotive force (EMF) or voltage induced ($V_{induced}$) around loop in sheet:**

Using Faraday's Law of Induction which predicts how a time-varying magnetic field will interact with an electric circuit to produce an EMF, the induced voltage or EMF at the receiving loop can be calculated as [80]:

$$EMF = V_{induced} = -N \frac{d\Phi}{dt} \ , \tag{3.20}$$

where Φ denotes magnetic flux density in Wb/m^2 or Tesla, and N denotes number of turns. This law suggests that additional EMF (voltage) will be induced as the rate of change of magnetic flux density increases. The negative sign means that the induced electric field will directionally oppose the change in the magnetic field. Flux density Φ through a surface is the surface integral of the normal component of the magnetic field (B) passing through that surface. The SI unit of magnetic flux is Weber (*Wb*) or *Volt-seconds*. The flux density time function is defined as [80];

$$\Phi(t) = \iint B_{sheet} \, . \, dS \ . \tag{3.21}$$

This integration is over the area (A) through which the magnetic field passes [80], i.e.,

$$\Phi(t) = B_{sheet}.A\cos(\theta) \tag{3.22}$$

where θ denotes angle between the surface through which the magnetic field passes and the magnetic field vector. Magnetic flux density is maximized when the magnetic field is normal to the surface of the sheet. For a circular loop, area $A = \pi\left(\frac{D}{2}\right)^2$. Thus, the magnetic field can be given as [80]

$$\Phi(t) = \frac{\mu_0}{D} I_0 \sin 2\pi f t \ \pi\left(\frac{D}{2}\right)^2 \cos(0) \tag{3.23}$$

$$\Phi(t) = \frac{1}{4}\mu_0 I_0 D\pi \ \sin 2\pi f t \quad . \tag{3.24}$$

Therefore, induced voltage has the following form [80]:

$$V_{induced}(t) = -N\frac{d\Phi}{dt} = -N\ \frac{1}{4D}\mu_0 I_0 D\pi\ \ 2\pi f \cos 2\pi f t \tag{3.25}$$

$$V_{induced}(t) = \ -\frac{N\mu_0 I_0 D\pi}{4}\omega\cos 2\pi f t \quad . \tag{3.26}$$

5) **Find the resistance (R) around a loop within the sheet:** Resistance R for any section can be generally calculated using the following equation [81]:

$$R = \rho\frac{L}{A} \tag{3.27}$$

where ρ denotes resistivity of material, L is length of section, and A is cross-sectional area of current flowing loop in the sheet, and (L) is the circumference of the current flowing loop in the sheet [81] ($L = \pi.D$). (A is width (W) multiplied by sheet thickness (th); i.e., $A = W.th$ which can be illustrated in Figure 3.6).

Therefore, R for a loop section is given by

$$R = \rho\frac{\pi D}{th\,.\,W}\,. \tag{3.28}$$

For example, if diameter (D) is 0.05 m, width (W) is $1\,.\,10^{-3}$m, and thickness (th) is $1.\,10^{-6}$m, $R = 4.4296$ Ohm. Impedance of the cross-sectional area of the current at angular frequency (ω) is [80]

$$Z = R + j\omega L \quad . \tag{3.29}$$

However, for impedance approximation, the assumption can be made that the inductance is zero for DC. Therefore,

$$Z \cong R \quad . \tag{3.30}$$

6) Find current (*I*) in loop within sheet using Ohm's Law:

To calculate current induced in the sheet/loop, Ohm's law can be used [80]:

$$I_{induced}(t) = \frac{V_{induced}(t)}{Z} \quad . \tag{3.31}$$

Substituting the value of induced voltage in Eq. (3.26) and impedance (Z) in Eq. (3.31) results in

$$I_{induced}(t) = \frac{V_{induced}(t)}{R} \tag{3.32}$$

$$I_{induced}(t) = \frac{-\frac{N}{4}\mu_0 I_0 D\pi\, 2\pi f.\cos 2\pi f t}{(\rho\frac{\pi D}{th.W})} \tag{3.33}$$

$$I_{induced}(t) = \frac{-\frac{N}{4}\mu_0 I_0\, 2\pi f.\ \cos(2\pi f t).th.W}{\rho} \quad . \tag{3.34}$$

For a loop with one turn, $N = 1$, the relative magnitude of current compared to magnitude of original current in source loop = $I_0 \sin 2\pi f t$ is $\frac{\mu_0 I_0.\,\pi f\,.\,th\,.\,W}{2\rho}$

Therefore, the magnitude of induced current is related to the magnitude of initial current I_0 via a multiplication factor corresponds to,

$$Multiplication\ Factor = \frac{\mu_0\,\pi f\,.\,th\,.\,W}{2\rho} \quad . \tag{3.35}$$

7) Compare with original current source $I_{source\_loop}(t)$:

If inductance of the loop wire ($L \approx 0$) is neglected for a first order approximation, a loop with one turn (N=1) is used, and the negative sign represents the direction of induced field removed in the calculation, then

$$0.5\, I_0 \sin 2\pi f t \left(\rho \frac{\pi D}{th.W}\right) = \Phi_0 2\pi f \cos(2\pi f t)\ . \tag{3.36}$$

However,

$$f \cos(2\pi f t) = \frac{1}{\Phi_0 2\pi} 0.5\, I_0 \sin(2\pi f t) \left(\rho \frac{\pi D}{th.W}\right) \tag{3.37}$$

$$\frac{f \cos(2\pi f t)}{\sin(2\pi f t)} = \frac{1}{\Phi_0 2\pi} 0.5\, I_0 \left(\rho \frac{\pi D}{th.W}\right). \tag{3.38}$$

Corresponding frequency can be calculated by solving this non-linear equation for every value of thickness (th). The purpose is to vary sheet thickness (th) in the range of 100 nm and 80,000 nm and calculate corresponding frequency that satisfies (3.38). By fixing the sheet effectiveness parameter (th) to a certain value (i.e., $th = 1\ \mu m$), shielding effectiveness as a function of frequency can be plotted, as shown in Figure 3.9.

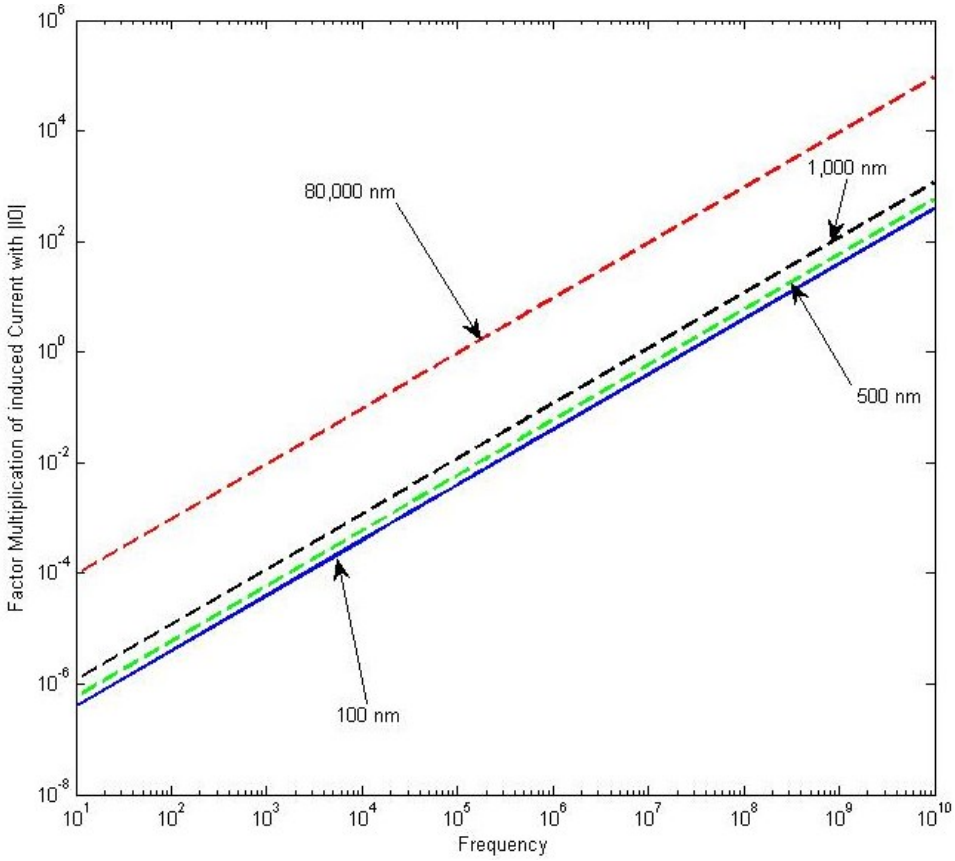

Figure 3.9 Multiplication factor of Eddy current flowing in pure aluminum sheet relative to the current in the source loop

As shown in Figure. 3.9, the current multiplication factor of 0.5 (shielding effectiveness of 6 dB) occurs at frequency 7.145 MHz when sheet thickness is 100 nm. The frequency corresponding to a 6 dB shielding effectiveness for various material thicknesses of aluminum is summarized in Table 3.1.

Table 3.1 Frequency corresponding to 6 dB shielding effectiveness for aluminum

Sheet Thickness	6 dB Shielding Effectiveness Frequency
80,000 nm	0.055 MHz (55 KHz)
1,000 nm	7.145 MHz
500 nm	14.29 MHz
100 nm	71.43 MHz

For a copper fabric that is used to build the space suit mock up, the calculated and measured frequency corresponding to 6 dB shielding effectiveness are listed in Table 3.2

Table 3.2 Frequency corresponding to 6 dB shielding effectiveness for space suit mockup copper plated fabric

Commercially woven copper sheet (space suit mockup model)	Approximate theoretical calculation of frequency at which $I_{induced} = I_{orginal}$	Measured frequency at which $I_{induced} = I_{orginal}$
Thickness = 80,000 nm	~ 1 MHz	~ 987 KHz

In Figure 3.10, the shielding effectiveness for various conductive surfaces is plotted for comparison at fabric thickness of 1000 nm. Frequencies corresponding to 6 dB shielding effectiveness for different materials are summarized in Table 3.3.

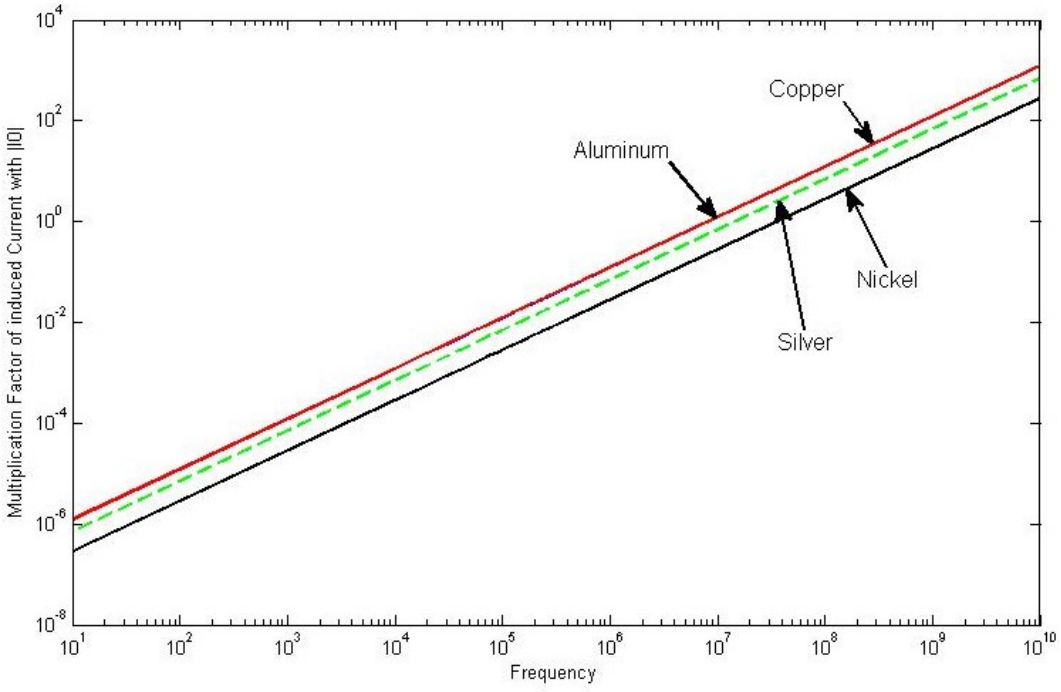

Figure 3.10 Shielding effectiveness for different materials at fabric (thickness=1000 nm)

Table 3.3 Frequency corresponding to 6 dB shielding effectiveness occurs for various materials (1000 nm thickness)

Material	Shielding Effectiveness Frequency
Silver (green)	4.025 MHz
Copper (blue)	4.255 MHz
Aluminum (red)	7.145 MHz
Nickel (black)	17.71 MHz

3.3.2 Measurement Setup and Results

The theoretical first order approximation for shielding effectiveness is validated through laboratory experiments. To conduct these experiments, a two-port network device is assumed in which each port is connected to a small circular loop antenna unmatched to the 50 Ohm coaxial cable impedance.

3.3.2.1 Loop Antennas to Measure Loss Caused by Copper Fabric

After calibrating S21 transmission gain of the network analyzer with coaxial cables to remove their effects of cable loss, two-loop antennas are mounted parallel to each other with a separation distance of 3 cm to serve as a magnetic field source, as demonstrated in Figure 3.11.

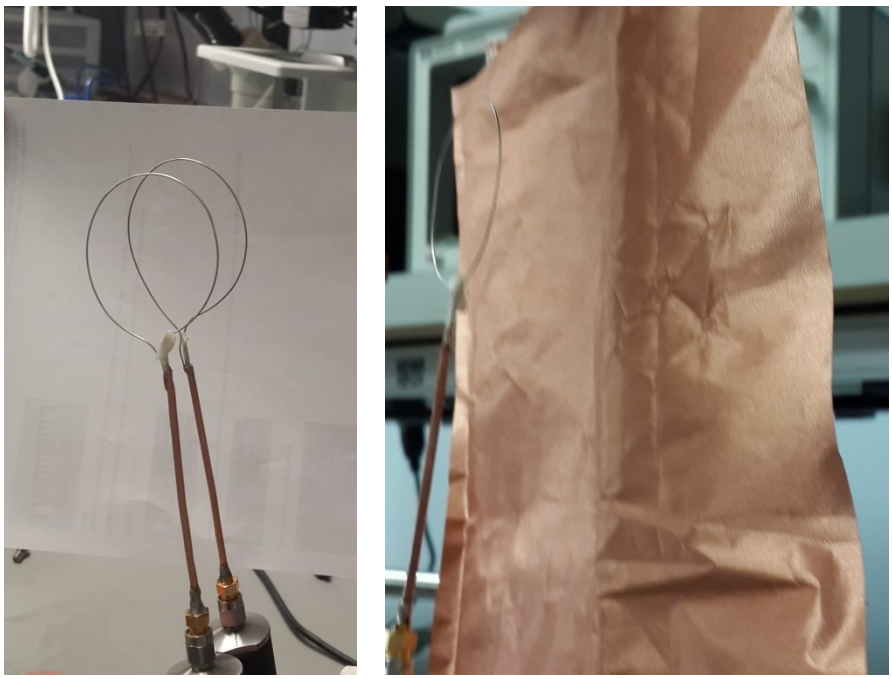

Figure 3.11 Measurement setup for Case 1 (without fabric) and Case 2 (with fabric): two small loop antennas separated by 3 cm

As shown in Figure 3.12, the transmission gain parameter (S21) is measured and plotted The transmission gain parameter is plotted for frequencies ranging from 10 KHz to 20 MHz. Two curves are displayed in the figure: one curve corresponds to Case 1 (two antennas without copper fabric between the loops) in Figure 3.11 (left) and the second curve corresponds to Case 2 (with copper fabric placed fabric between the two antennas in Figure 3.11 (right)).

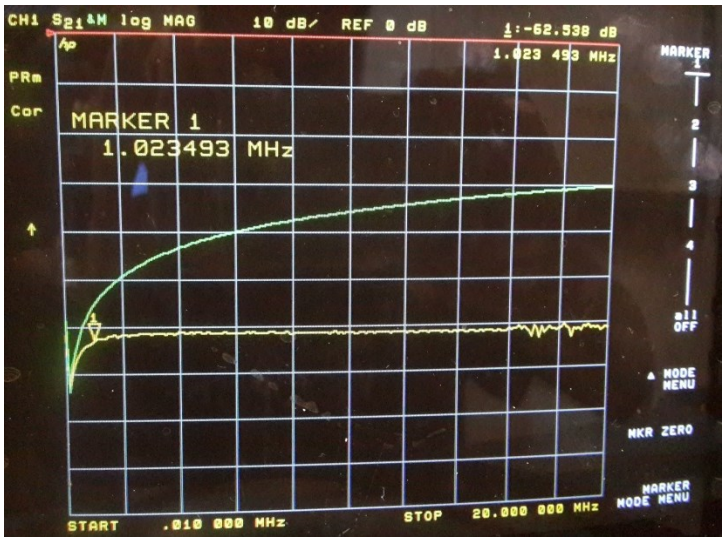

Figure 3.12 S21 measurement for two loops

Figure 3.12 illustrates the effect of copper fabric placement in the middle of the loops. The forward transmission gain (S21) parameter decreased significantly and it is almost flat along all frequencies from 10 KHz to 20 MHz In addition, the 6 dB difference due to the shielding effect of copper fabric occurs around 1 MHz frequency.

Next, the copper fabric is replaced with the torso section of the spacesuit mockup (Figure 3.13); the S21 parameter is re-measured.

Figure 3.13 Torso section of KSU spacesuit mockup

After placing the torso section, the path gain drops significantly and a 6 dB drop occurs at frequency of 1 MHz.

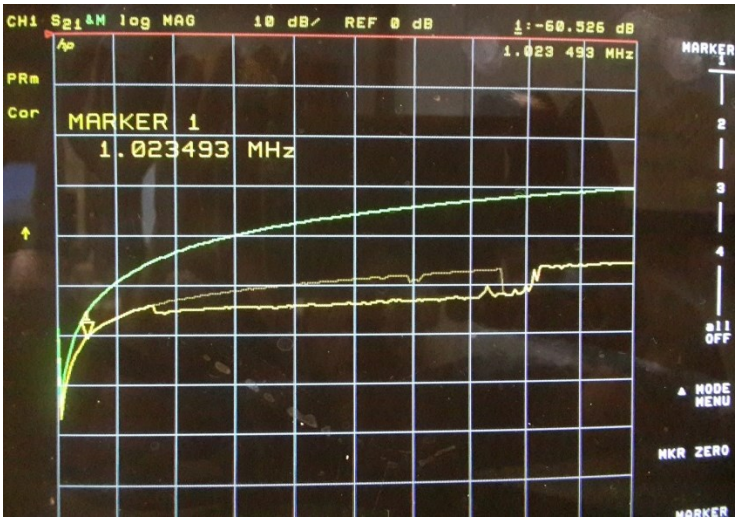

Figure 3.14 S21 for loop antennas with and without the torso section

Next, measurement of shielding effectiveness of a space suit arm segment is conducted to compare with the results of torso section as demonstrated in Figure 3.15.

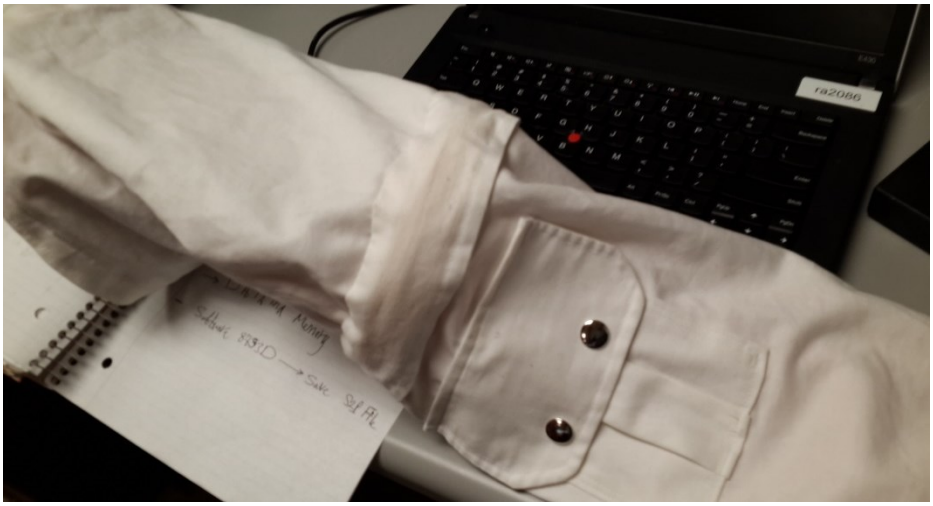

Figure 3.15 Arm section of KSU space suit mockup model

Measured forward transmission gain for this experiment is plotted in Figure 3.16 using two-loop antennas without the arm segment and when the arm segment is placed between the transmit and receive antennas. In this case, a transmission gain drop of only a few dBs is noticed.

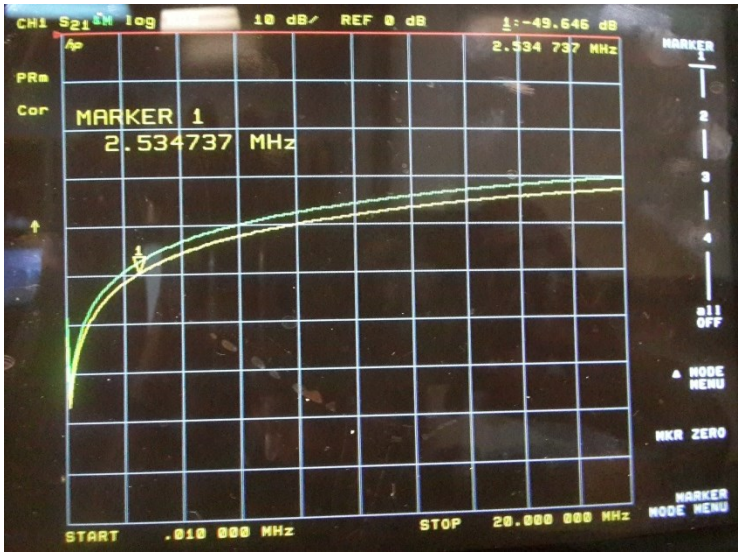

Figure 3.16 Measured S21 for loop antennas without and with arm section corresponding to setup in Figure 3.14

This surprising measurement result was also observed while performing a similar experiment on a real space suit at Kansas Cosmophere and Space Center. One possible explanation for this observation is the following: with extensive use of the suit, crinkles (microscopic breaks) start to appear in the copper fabric mesh over time. These metalized layers in turn change the conductivity of the fabric, reducing their shielding effectiveness. In our mockup space suit, unlike the arm sections, the torso section was designed to be firm and not flexible. Thus, no significant change in conductivity was observed and the shielding behavior is consistent with that expected from a copper fabric. While resistance measurements on the fabric in the arm and torso sections seems to support this hypothesis, further investigation into the effects of "regular use" on the microscopic structure of the fabric is necessary.

3.3.2.2 Helical Monopole to Measure Loss due to Copper Fabric

The previous experiment is conducted again using helical monopole electric field antennas set parallel to each other and separated by 3 cm, as shown in Figure 3.17. The measured S21 parameter in Figure 3.18 shows that a 18 dB difference occurs at frequency of 967 KHz.

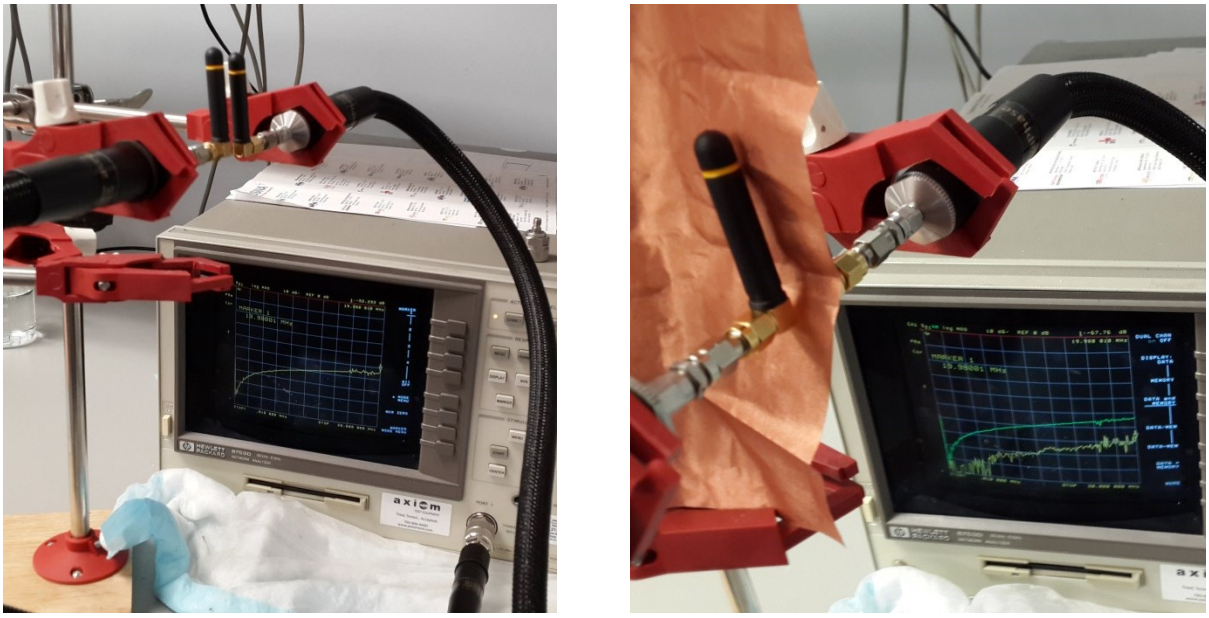

Figure 3.17 Two 915 MHz monopole antennas (left) without and (right) with copper fabric

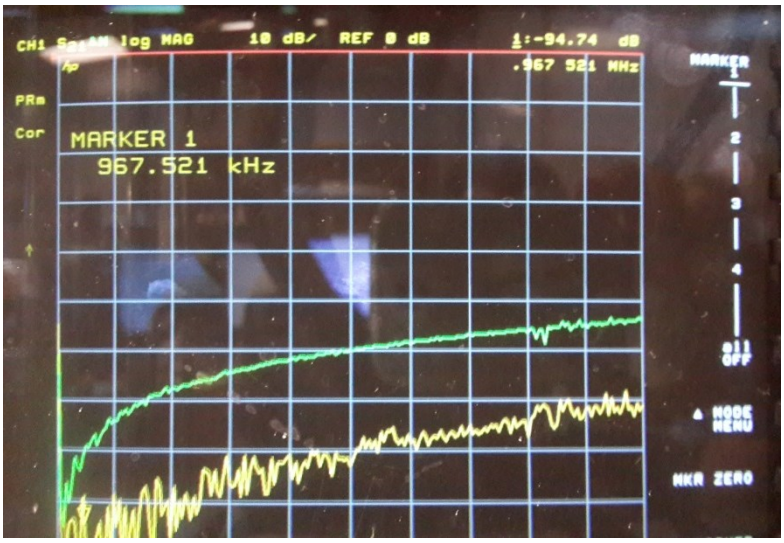

Figure 3.18 Measured S21 corresponding to Figure 3.16: no shield (left) and with fabric shielding (right)

Finally, an arm segment of space suit is inserted between the transmit and receive antennas as shown in the setup in Figure 3.19. Measured transmission gain parameter (S21) is plotted in Figure 3.20. Two curves are shown in Figure 3.20 where one for case when no space suit is placed between the transmitter and receiver and one time when the space suit segment is

placed between the two antennas. It can be noticed that around a 13 dB drop occurs when the arm segment is placed between the transmits and receive helical monopole antennas at 967 KHz.

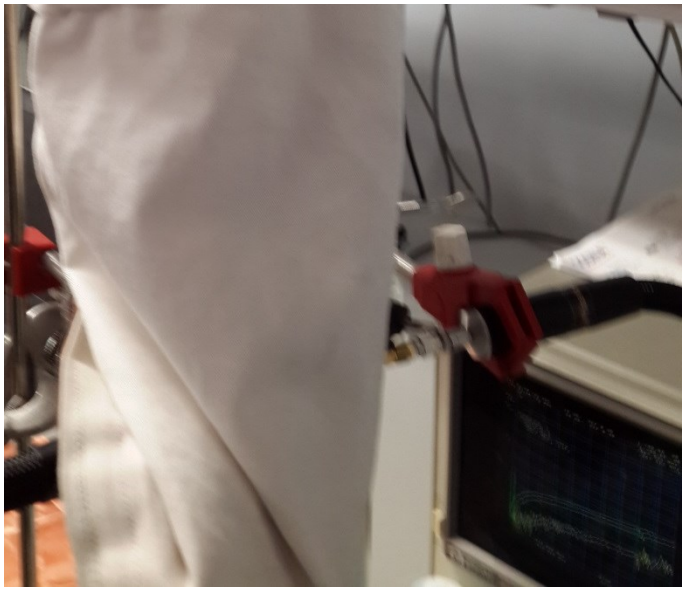

Figure 3.19 Placing arm section of space suit mockup between monopoles

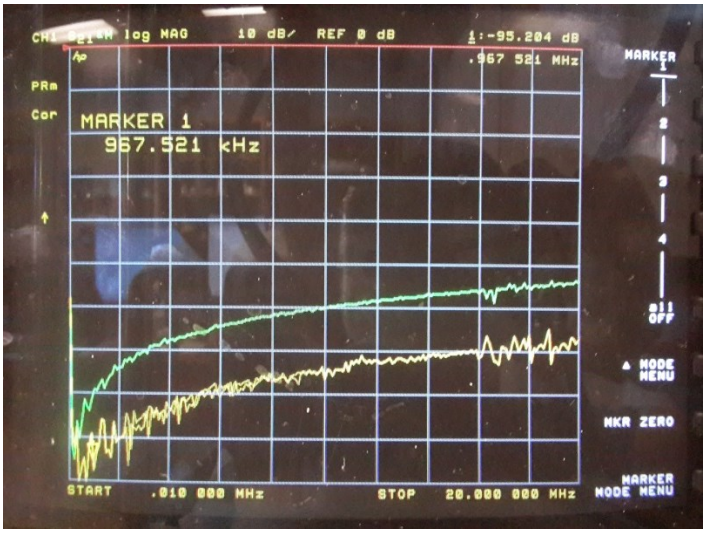

Figure 3.20 Measured S21 corresponding to Figure 3.18 setup (without and with arm section)

3.4 Chapter Summary

This chapter highlighted the fundamentals of electromagnetic shielding for various conductive materials. First, the concepts of shielding effectiveness for plane wave versus near-field sources were reviewed and shielding effectiveness for electrically and magnetically sources was described. Next, a simple analytical study was conducted to indirectly evaluate shielding effectiveness for the aluminized mylar embedded in space suit fabrics under simplifying assumptions. Based on this chapter's findings, if electric field antennas are used, the EMU space suit is largely radio-opaque to electrically polarized antennas. Also, the shielding effectiveness for small loop magnetic field antennas is found be to be high for torso section. However, forward transmission gain of the two small loop antennas didn't differ significantly for arm/leg segments. One possible explanation for this phenomenon is that the space suit segments, such as arm or leg segments, after extensive use can suffer from crinkles resulting in non-uniform distribution of the conductive threads that constitutes the fabric. This microscopic change in the fabric appears to significantly reduce the conductivity of the fabric which in turn makes the conductive fabric or TMG layers in these segments largely radio-transparent. For the rest of this dissertation, we will assume that the space suit TMG layers are largely radio-opaque.

Chapter 4 - Propagation Modes in Space Suit Segments

The discussion of the most critical parameters that describe electromagnetic (EM) interaction with the human body in Chapter 2 and the description of space suit structure and its shielding properties in Chapter 3 provide the background necessary to characterize the propagation structure within a space suit. This chapter introduces hypothesized propagation models for a small segment of space suit, specifically the arm segment. The proposed models are validated through both simulations and experiments. This chapter also includes an evaluation of the radio link characteristics at various frequency bands using two common antenna polarizations: vertical and horizontal electric field polarization. The evaluation process involves a comparison of free space antennas, on-body antennas, and antennas on-body and inside the space suit arm segment.

4.1 Small-Scale Propagation Models for Intra-Space Suit Environment[3]

In this Section, two propagation modes are hypothesized and verified through simulations and experiments.

4.1.1 Loaded Circular Waveguide Propagation Model

The cylindrical metal structure of the space suit's outer layers together with the human arm within the space suit motivates consideration of a loaded circular waveguide propagation model. In this hypothesized model, cutoff frequency can be calculated based on the TE_{11} mode for propagation which is typically the dominant propagation mode, as shown Figure 4.1. Cutoff frequency for this mode can be calculated from:

---

[3] *Copyright 2013 Association for Computing Machinery (ACM)*. Portions of section 4.1 are reprinted with permission from M. Taj-Eldin, W. Kuhn, B. Natarajan, "Study of Radio Channel for Biomeidical Sensors in Spacesuits," *BodyNets '13 Processings of the 8th International Conference on Body Area Networks,* Sept 30- Oct 2, 2013, pp 302-306.

$$f_{c_{mn}}^{TE} = \frac{\chi'_{mn}}{2\pi a\sqrt{\mu\varepsilon}} \tag{4.1}$$

where a denotes waveguide radius, μ denotes permeability, ε denotes material permittivity, χ'_{mn} is the constant for propagation mode mn, and the dominant mode number is $mn = 11$. For example, substituting the speed of light in free space for $1/\sqrt{\mu\epsilon}$ with $a = 0.095$ meters and χ'_{11}=1.8412 in (4.1) results in $f_{c_{11}}^{TE}$ = 925 MHz. If the circular waveguide model holds, a cutoff frequency is expected between two extreme cases ($f_{c_{11}}^{TE}$ with air dielectric = 976 MHz and $f_{c_{11}}^{TE}$ with full core of human tissue = 158.4 MHz).

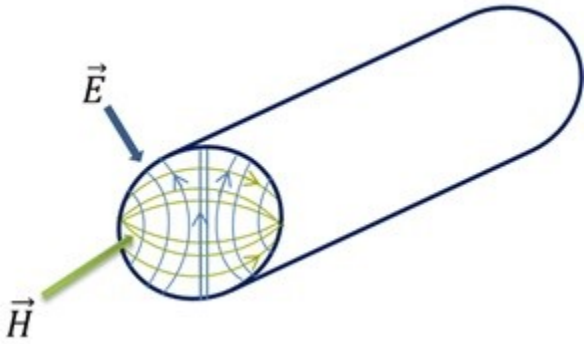

Figure 4.1 Electric and magnetic field for circular waveguide dominant mode

4.1.2 Coaxial Cable Model

Next, we consider a coaxial transmission line model. Figure 4.2 depicts a coaxial transmission line model.

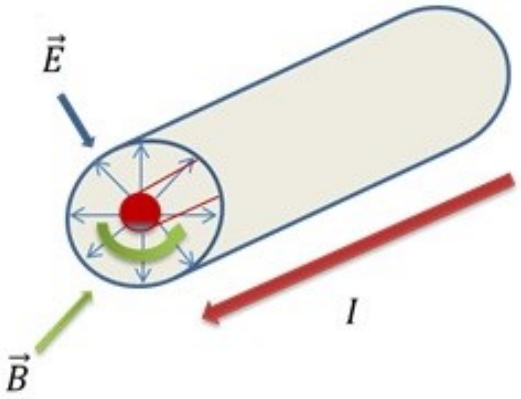

Figure 4.2 Transverse electromagnetic mode

In this model, the electric field (E) is normal to the surface of inner conductor (astronaut's arm), and the magnetic field (B) is tangential to the inner and outer surfaces and normal to both the electric field and to the direction of wave propagation.

Transverse electromagnetic (TEM) fields illustrated in Figure 4.2 represent ideal fields; however, in the experimental validation section, directions of produced fields may not necessarily conform to this ideal case. In particular, at frequencies higher than cutoff frequency, coaxial structure dimensions support more complex modes. This multi-mode propagation begins to occur at frequency f_m, given by

$$f_m = \frac{c}{\lambda_c} = \frac{c}{\pi\left(\frac{D+d}{2}\right)\sqrt{\mu_R \epsilon_R}} \tag{4.2}$$

where μ_R and $\epsilon_R$denote permeability and permittivity of the dielectric, respectively, and d and D denote inner and outer conductor diameters, respectively. Substituting 0.19 meters for D, 0.088 meters for d, and $\mu_R = \epsilon_R = 1$ in Eq. (4.2) results in f_m = 687 MHz.

At frequencies below f_m, the lumped element approximate equivalent circuit for this coax model resembles a lossy transmission line with the addition of C_2 component parallel to series resistance R, as shown in Figure 4.3.

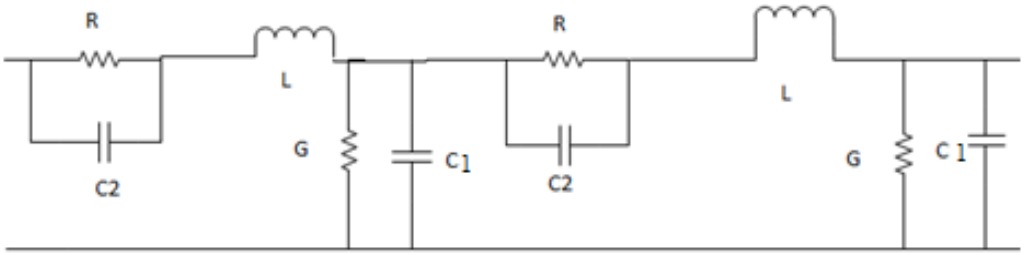

Figure 4.3 Equivalent circuit of a section of human tissue with space suit

The propagation constant can be computed from

$$\gamma = \alpha + j\beta = \sqrt{\left(\frac{R \times (-jX_{C_2})}{R - jX_{C_2}} + j\,\omega L\right)(G + j\omega C_1)} \tag{4.3}$$

where α is the attenuation constant; β is the phase constant; and R, G, C_1, X_{C2}, and L are per unit length values. Conductance G is negligible for air. L and C_1, based on expressions for a coax model derived in [82], utilize inner (arm) and outer conductor (space suit) radius values based on setup parameters from this test ($b = {}^{D}/_{2}$= 0.095 and $a = {}^{d}/_{2}$ = 0.044 meters). Values of L and C_1 are 0.13 uH and 85 pF at 400 MHz. Resistance per unit length R can be calculated from $R = \frac{L}{A\sigma}$, where L and A are length and cross-sectional area of a unit block of cylindrical arm model [83] and σ is the arm conductivity. Similarly, C_2 can be calculated from $C_2 = \frac{\varepsilon_r \varepsilon_0 A}{L}$, where ε_r is relative permittivity of human tissue and ε_0 is permittivity of free space. Table 4.1 shows relative permittivity and conductivity using Cole-Cole Model and published values in [22].

However, attenuation estimation for an arm inside a section of space suit is problematic because of the difficulty in determining area A in R and C_2 in the inhomogeneous body model. Nevertheless, upper and lower bounds of attenuation can be calculated, as explained in the following.

Table 4.1 Permittivity and conductivity of human tissues at 400 MHz

Tissue	ϵ_r	$\sigma(S/m)$
Skin	46.787	0.68806
Fat	5.5798	0.04142
Muscle	57.129	0.79631

4.1.2.1.1 Equipotential Excitation Assumption along the Unit Block Cross Section

Fields within the arm tissue are complex and three-dimensional in nature. Therefore, in order to estimate component values in Figure 4.3 and resulting attenuation per unit length, the cross-section in Figure 4.3 was assumed to be an equipotential surface [83]. In this case, the definition of area A in equations for R and C_2 for a certain tissue is the cross-sectional area of that tissue. For example, the area (A_{tissue}) of skin or fat tissues is the circumference of that tissue multiplied by its corresponding thickness. However, the area (A_{tissue}) for muscle is approximately the area of a circle that represents the muscle with radius equal to the muscle thickness. Capacitances of skin, fat, and muscle layers can be calculated based on the area of each layer and its relative permittivity. Therefore, capacitance C_2 in Figure 4.3 is equivalent to three parallel capacitors and R is the equivalent resistance of three parallel resistors, each calculated based on conductivity and cross-sectional area of those tissues (Table 4.1).

4.1.2.1.2 Excitation of Fields on Skin Surface

The equipotential surface assumption for the cross section in Figure 4.4 is a rough approximation. At sufficiently high frequency, most electric fields propagate only in skin and fat layers. Therefore, capacitances of skin and fat layers in which areas of skin and fat tissues can be calculated identically to the equipotential excitation method, were computed for this study. Capacitance C_2 in Figure 4.3 is the equivalent of only these two parallel capacitors. Similarly, resistance per unit block R is the equivalent resistance of parallel skin and fat resistors.

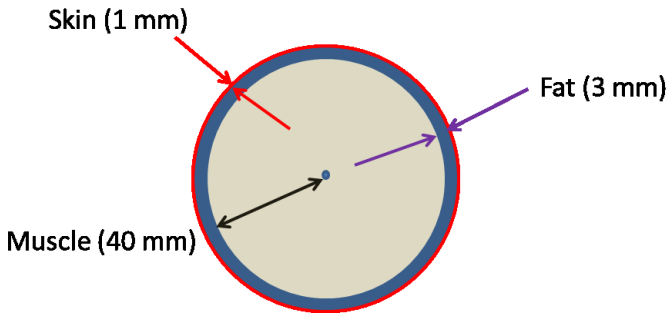

Figure 4.4 Numerical human body model

Resulting R and X_{C2} values for the two cases discussed above are provided in Table 4.2.

Table 4.2 Values of X_{C2}, R per unit block of one meter and attenuation for 30 cm unit length

	X_{C2}	R (Ohm)	Attenuation (dB) for 30 cm unit length
Lower Bound (equipotential excitation)	147.5	230	2.6
Upper Bound (excitation on skin surface)	2574	4468	50.8

Table 4.2 shows that resistance for equipotential excitation is relatively low, so this case provides a lower bound on expected attenuation. However, values of resistance, reactance, and subsequently the attenuation became very high when wave excitation was assumed on the skin surface, thereby providing an upper bound on expected attenuation. In practice, the fields only partially penetrate into the muscle region, thereby requiring simulations and measurements in order to accurately estimate expected attenuation.

4.1.3 Simulation and Experimental Validation of Coax Model

Next, annular copper fabric rings placed 30 cm apart (Figure 4.5) on a person's arm were used to excite TEM wave based on the coax model assumption. Ground was tied to the outer conductive cylinder.

4.1.3.1.1 Simulation and Measurement Setup

Numerical simulation was conducted using Agilent's EMPro FDTD-based solver to find the forward transmission gain (S21) curve. Multilayer cylinders simulated skin, fat, and muscle on a human arm, with layer thicknesses being 1mm, 3mm, and 40 mm, respectively. Figure 4.5 illustrates the simulation model including a human arm and annular rings as well as a tube of aluminum that represents TMG metallic layers in the space suit.

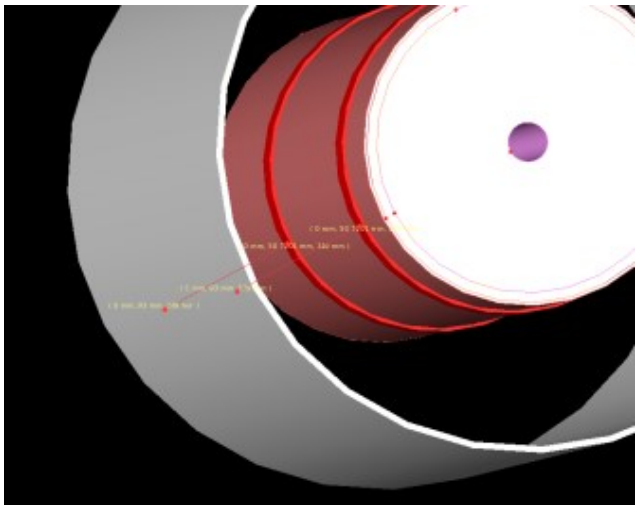

Figure 4.5 Simulation setup

Conformal meshing [84] was enabled for the annular rings and aluminum tube so that meshes for the metal objects could be properly generated. Target cell sizes in the grid for skin, fat, and muscle tissues were 2 mm, 4 mm, and 4 mm, respectively, and target cell sizes for the annular rings and aluminum tube were 1mm and 4 mm, respectively. Target base cell size for the entire simulation domain was set to 1 mm in the three dimensions. The boundary conditions for

the box containing the model were absorbing boundaries in the three dimensions, and a perfectly matched layer (PML) was used with eight layers as type of absorption. Relative permittivity and conductivity values were based on the Cole-Cole model and frequency-dependent. The simulation timestep was 1.178×10^{-12} seconds which satisfied the stability condition. Maximum simulation time was set to 1,000,000 multiplied by the timestep. However, convergence occurred before that maximum time in simulations for this study. Transmit power of 0 dBm was applied to one of the annular ring in a frequency range of 300 KHz to 3 GHz. The field of interest converged sufficiently in these conditions. A convergence threshold of -30 dB produced relatively accurate S-parameter curves.

As shown in Figure 4.6, in order to validate simulations, a path loss measurement was performed in which a human arm was inserted inside a metal tube after being fitted with two annular rings of copper fabric separated by 30 cm. These annular rings were then connected to an HP Network Analyzer and the ground shield contacted the outer cylinder.

Figure 4.6 Measurement setup

4.1.3.1.2 Simulation and Measurement Results

S21 curves for simulated and measured values are plotted in Figures 4.7 and 4.8, respectively. No cutoff frequency was observed in the S21 curves, so waveguide propagation mode was not supported in the presented arm with space suit segment environment. Attenuation of the signal was simulated in Figure 4.7 for a separation of 30, 60, and 90 cm between the two rings (blue, red, and green curves, respectively), but measured for only 30 cm because of length constraints on a real human arm length. Total simulated loss at 400 MHz was 28.6 dB for 30 cm, 36.5 dB for 60 cm, and 45.5 dB for 90 cm. However, measured total loss at 400 MHz was 31.7 (Figure 4.8), or 3.1 dB higher than simulated loss due to non-ideal measurement setup. An impedance discontinuity occurred between the cavity inside the aluminum tube and impedance of the coaxial feed lines, resulting in extra loss in the S21 curves.

According to Figure 4.8, one can estimate the channel loss due to coax mode propagation for 30 cm arm length as the difference between simulated losses at 60 cm and 30 cm, or approximately 7.9 dB at 400 MHz. Channel loss for the following 30 cm arm length was approximately 9 dB. As the fluctuations in simulation results were not significant, the average of these two values was considered a reasonable estimate. Compared to upper and lower bounds of attenuation previously discussed, simulated path loss was well within the upper and lower bounds and simulated path loss (attenuation) was closer to the lower bound at which equipotential excitation was assumed. This observation suggests that fields in the tissue expectedly penetrate well into the muscle region, especially if the wave is launched at a relatively low frequency (400 MHz) compared GHz frequencies at which penetration/skin-depth of body layers is relatively deep (5.53 cm for skin, 30 cm for fat, and 5.2 cm for muscle) compared to that at GHz frequencies which is on the order of mm.

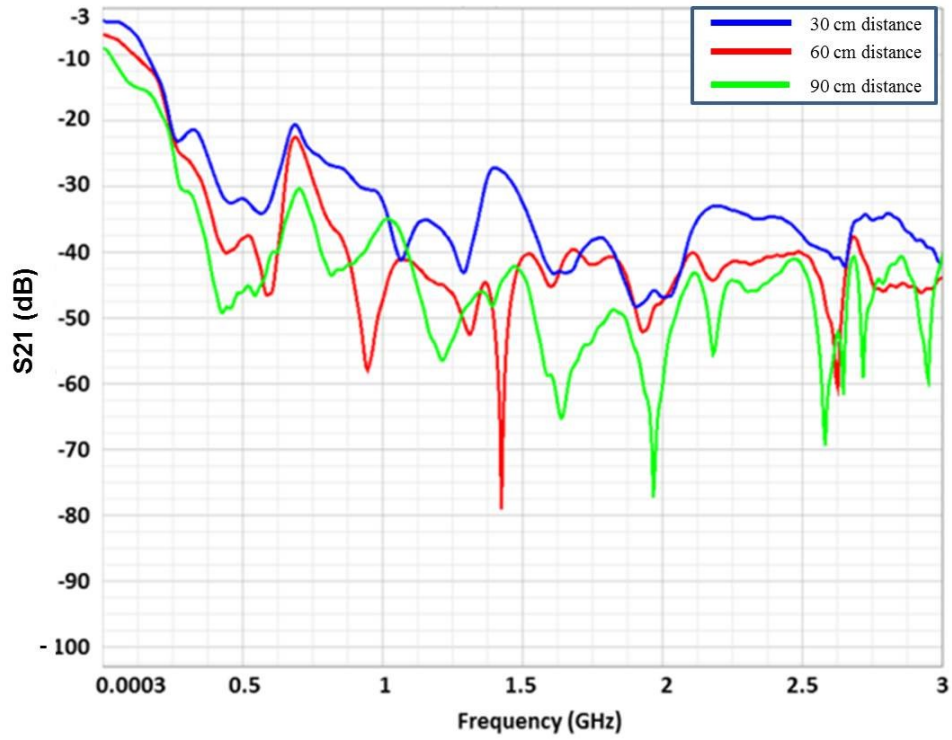

Figure 4.7 Simulated S21 curve: 300 kHz to 3 GHz; 10 dB/division vertical (blue for 30 cm, red for 60 cm, and green for 90 cm distance)

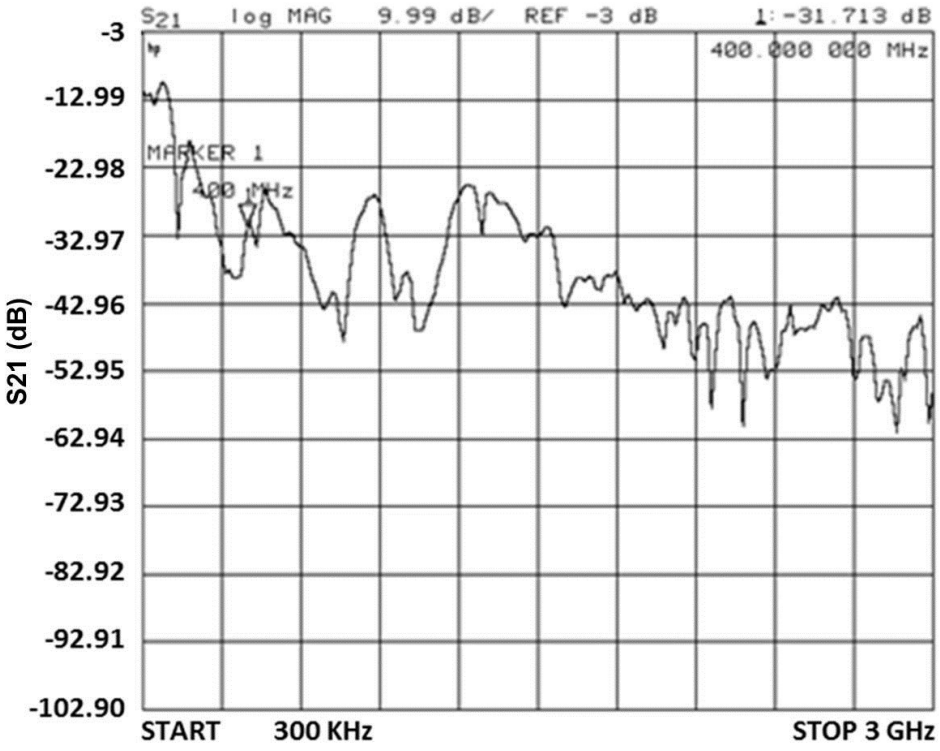

Figure 4.8 Measured S21 curve: 300 kHz to 3 GHz; ~10 dB/division vertical

In addition to channel loss per unit length, an additional loss was observed. This loss can be calculated as the difference between measured total loss for 30 cm in Figure 4.8 (31.7 dB) and channel loss for 30 cm arm length (~8.4 dB). The result of this difference was 23.3 dB, attributed in part to the impedance mismatch at the input and output of the coax mode with 50 Ohm impedance of network analyzer ports. Another reason for this additional loss is because of the antenna transducer effect of the copper rings (almost quarter wavelength compared to half the ring circumferences). The annular rings and ground connections did not perfectly excite the coax mode, so this level of input/output port mismatch-attenuation was not surprising.

In order to obtain a clear picture of the propagating wave, directions of electric and magnetic fields were plotted using the simulation model in Figure 4.9 (left) and a 3D direct FEM-based solver because FEM engine supports field visualization Minimal mesh size initially was 0.3125 mm, and convergence occurred when delta error was equal to 0.02 and required consecutive passes of delta error before simulation stops were 2 [85]. A vertical cut plane with arrows that represent field directions and strength 34.5 cm (slightly less than half wavelength at 400 MHz) away from the excitation point and electric and magnetic fields is illustrated in Figure 4.9. Red arrows represent strong fields and blue arrows represent weak fields. Results showed that the electric field was normal and the magnetic field was tangential to the human arm. Therefore, the structure supports a TEM wave and the coax model works well, especially at lower frequencies compared to that at the GHz region and higher than the cut-off frequency.

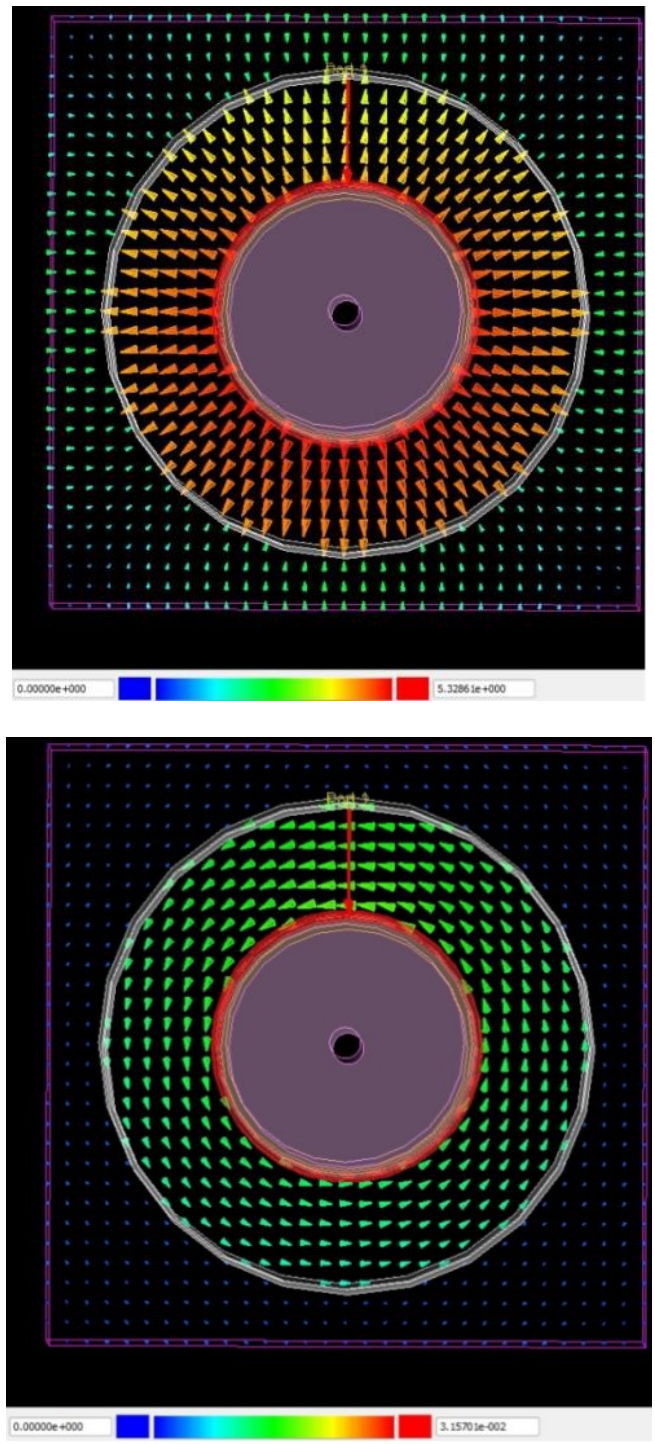

Figure 4.9 Electric (top) and magnetic (bottom) field direction at 34 cm separation

The following section quantifies path loss for various channel frequencies and, using simulation and laboratory measurements, investigate the effects of antenna polarization on channel path loss.

4.2 Antennas and Wave Propagation[4]

As discussed in Section 4.1, propagation structure inside the space suit is coaxial, meaning that when operating at a frequency below the multi-mode frequency, EM wave propagation follows TEM mode in which the electric field is normal to the inner conductor surface (i.e., human arm) and the magnetic field is tangential to the body and normal to the electric field direction and the wave propagation direction. The preliminary study described in Section 4.1 used annular rings to excite a TEM wave mode.

In an idealized setup illustrated in Figure 4.10, it consists of virtually infinite number of ports that start from the central point in the inner conductor and end at one point on the outer conductor that are uniformly distributed. This configuration should produce circularly symmetric TEM wave and one can assess the dB loss per unit length.

[4] *Copyright 2014 IEEE*. Portions of section 4.2 are reprinted with permission from Taj-Eldin, M.; Kuhn, W.; Natarajan, B.; Peterson, G., "Investigation of practical antennas for astronaut body area network," *Wireless for Space and Extreme Environments (WiSEE), 2014 IEEE International Conference on* , vol., no., pp.1,7, 30-31 Oct. 2014

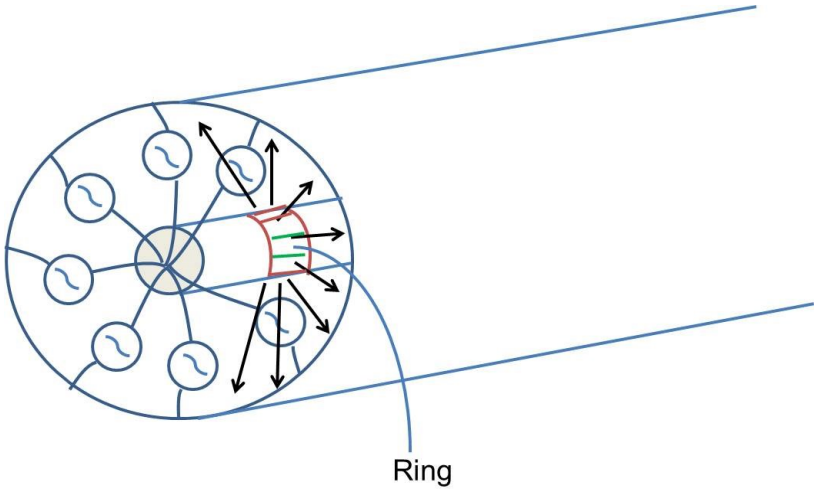

Figure 4.10 Idealized setup consisting of circularly symmetric loop antenna using infinite number of ports

However, because direct connection to the metalized outer layer of the suit is not practical for space suit body area networks, using antennas to launch EM waves is a more practical possibility. Therefore, Section 4.2 investigates use of commonly designed antennas that operate at common frequencies such as 433 MHz, 2.4 GHz, and 5.2 GHz. This includes the reflection coefficient, the 10 dB bandwidth and the gain of antenna.

4.2.1 433 MHz Microstrip Patch Antenna

A patch antenna is designed and built in EMPro EM simulator using very high permittivity material (K-160) with dielectric constant $\varepsilon_r = 160$. Therefore, the dimensions of the antenna are greatly reduced and it has dimensions of 38.6 mm× 24.72 mm for the patch and 48.05 mm×34.17mm for the substrate. The thickness of the substrate is 1.5748 mm. The simulated reflection coefficient for 433 MHz patch antenna is simulated in Figure 4.11 where the antenna has 10 dB bandwidth of 1.77 MHz and gain of 1.9 dBi.

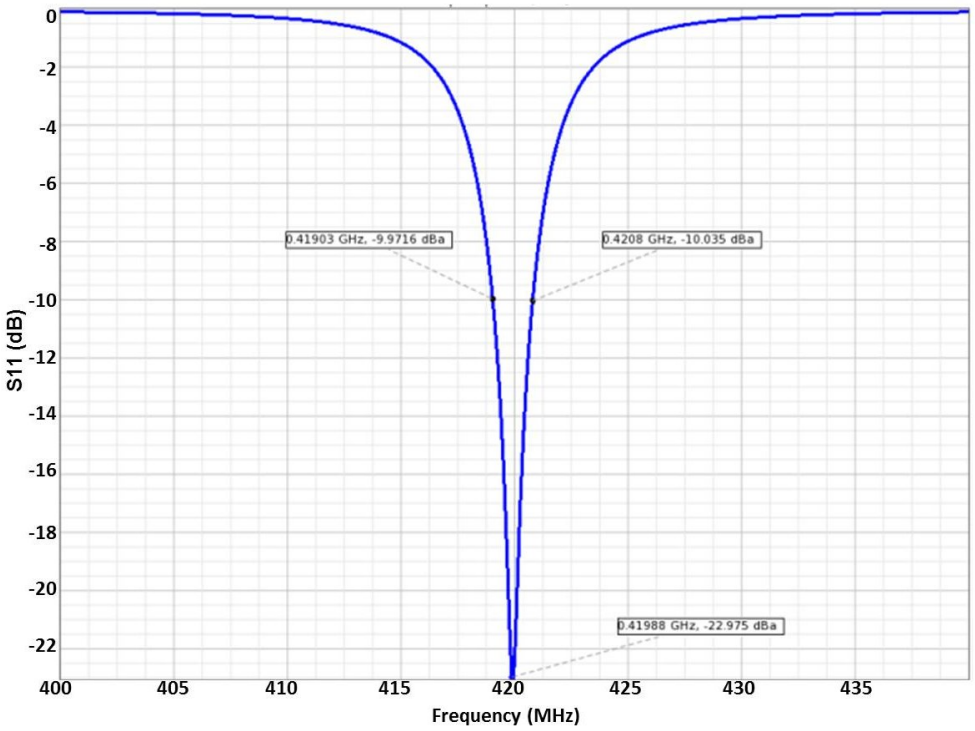

Figure 4.11 S11 for the 420 MHz patch antenna in free space (approximately -20 dB reflection coefficient)

To build such an antenna with the available commercial substrates, a high-K ceramic substrate with $\varepsilon_r = 83$ was used for the 433 MHz patch antenna in order to greatly reduce antenna size for body area network application (bottom, left of Figure 4.19). This 433 MHz patch antenna, which demonstrated somewhat suboptimal performance in terms of reflection coefficient, radiation efficiency, was built by grafting together nine copies of a commercial GPS patch antenna. The 433 MHz patch antenna shows only -3 dB of reflection coefficient due to its narrow bandwidth.

4.2.2 433 MHz Helical Monopole Antenna

A regular monopole designed at 433 MHz will have a length of 173.21 mm. However, for space suit applications, we need to have small antennas. Therefore, a commercial monopole is used and it has the form of helical wire with 26 turns. The antenna has reasonably good return

loss (10 dB) at the desired frequency. The simulated reflection coefficient for 433 MHz helical monopole is plotted in Figure 4.12 where the antenna has 10 dB bandwidth of 22 MHz and gain of 1.64 dBi.

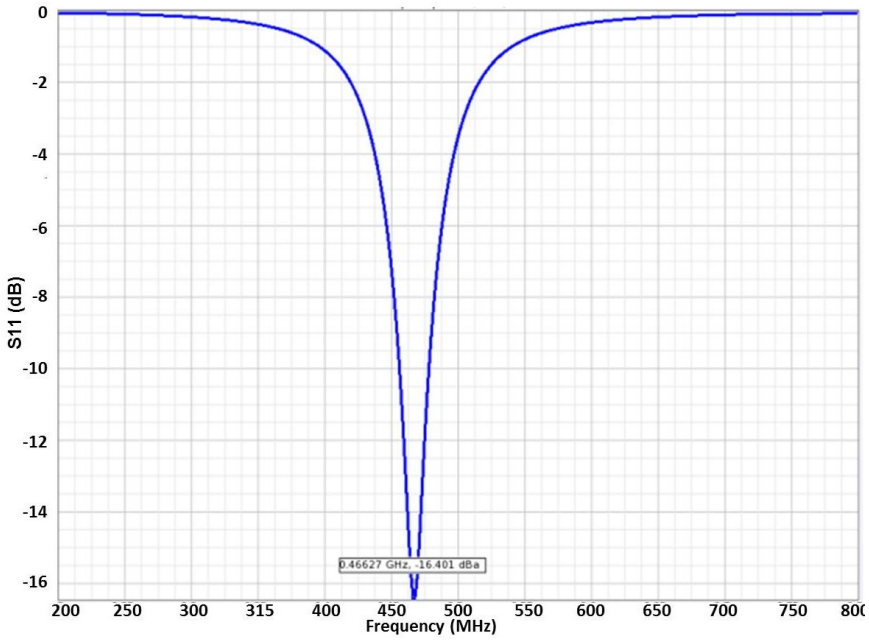

Figure 4.12 S11 for the 433 MHz monopole antenna in free space (-16 dB reflection coefficient)

4.2.3 2.45 GHz Microstrip Patch Antenna

A patch antenna is designed using FR-4 with dielectric constant ε_r= 4.6. The dimensions of this antenna are 11mm×13mm for the patch and 46.02mm×42.53mm for the substrate (top, right of Figure 4.19). The thickness of the substrate is 1.5748 mm. The simulated reflection coefficient for 2.45 GHz microstrip patch antenna is shown in Figure 4.13 where the antenna has -10 dB bandwidth of 50 MHz. The free space gain for this antenna is 4.2 dBi.

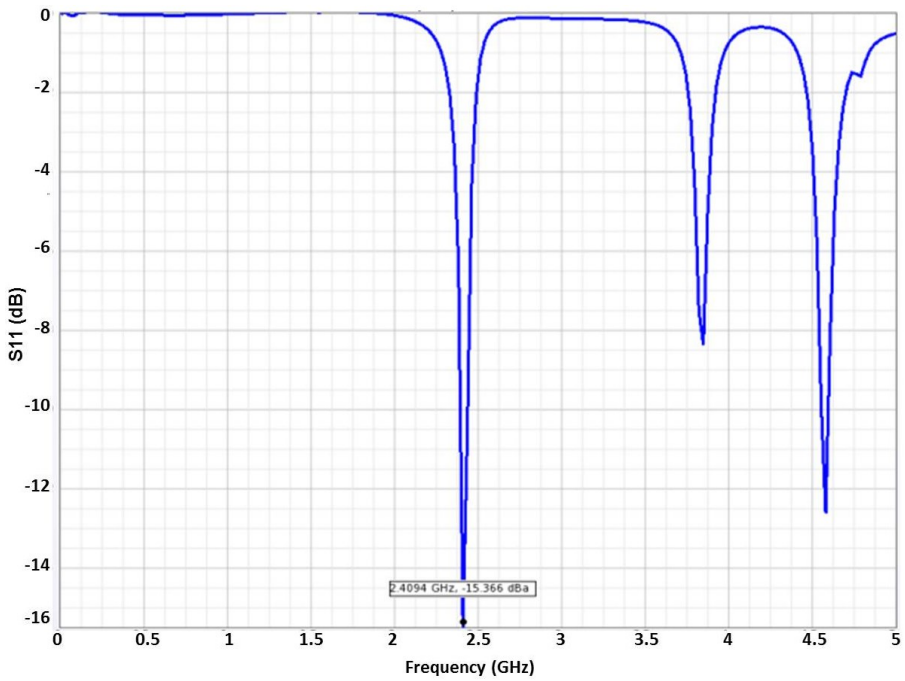

Figure 4.13 S11 for the 2.45 GHz Patch antenna in free space (-12 dB reflection coefficient)

4.2.4 2.45 GHz Helical Monopole Antenna

It is known that the length of the monopole is $\lambda/4$ at 2.45 GHz is 30.61 mm for ground plane (counterpoise). However, also due to our practical application, the ground plane size selected is 40mm×40mm. Thus, to tune the operating frequency to the desired value, we need to extend the monopole to 36 mm. The simulated reflection coefficient for 2.45 GHz monopole is plotted in Figure 4.14 where the antenna has -10 dB bandwidth of 180 MHz and free space gain of 2.2 dBi.

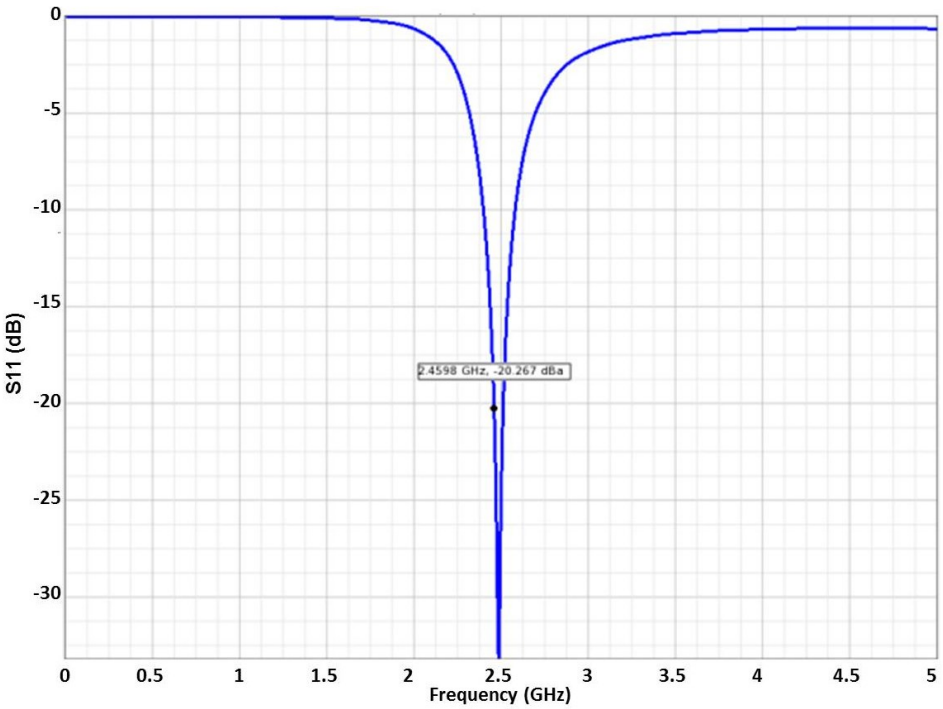

Figure 4.14 S11 for the 2.45 GHz Monpole Antenna in free space (-20 dB reflection coefficient)

It should be noted that helical monopole antennas are used from Antenna Factor by Linx for 433 MHz [86] shown in bottom, right of Figure 4.19 and 2.45 GHz [87]. Then, a custom ground/counterpoise is built for both antennas to make the human body the ground/counterpoise during the path loss measurements. Final 433 MHz and 2.4 GHz helical monopole antennas have the configuration shown in Figure 4.15 where the outer shield of the antenna is in contact with the built counterpoise on a 40 mm * 40 mm FR-4 substrate.

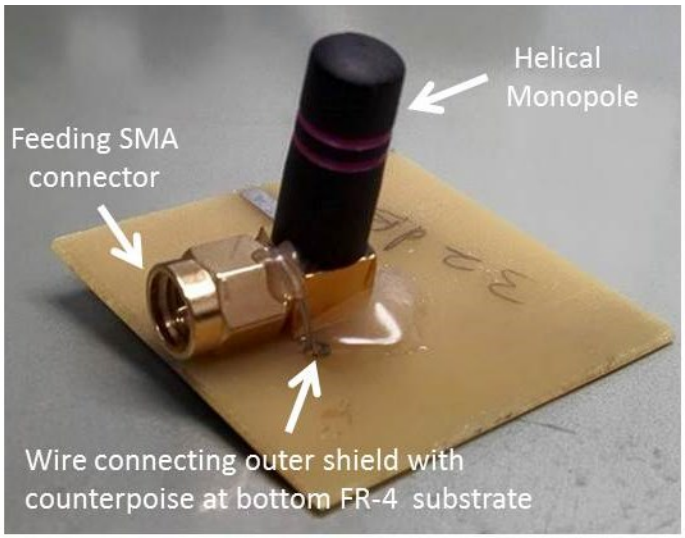

Figure 4.15 Configuration of 2.4 GHz helical monopole [87] for intra-space suit path loss measurements

4.2.5 5.2 GHz Microstrip Patch Antenna

A patch antenna is designed using Rogers RO4003 with dielectric constant ε_r=3.38. The dimensions of this antenna are 11mm×13mm for the patch and 21.74 mm×29.92 mm for the substrate. The reflection coefficient for 433 MHz patch antenna is simulated in Figure 4.17 where the thickness of the substrate is 1.5748 mm. The simulated reflection coefficient for 5.1 GHz patch antenna is presented in Figure 4.16 where the antenna has -10 dB bandwidth of 70 MHz and free space gain of 4.2 dBi.

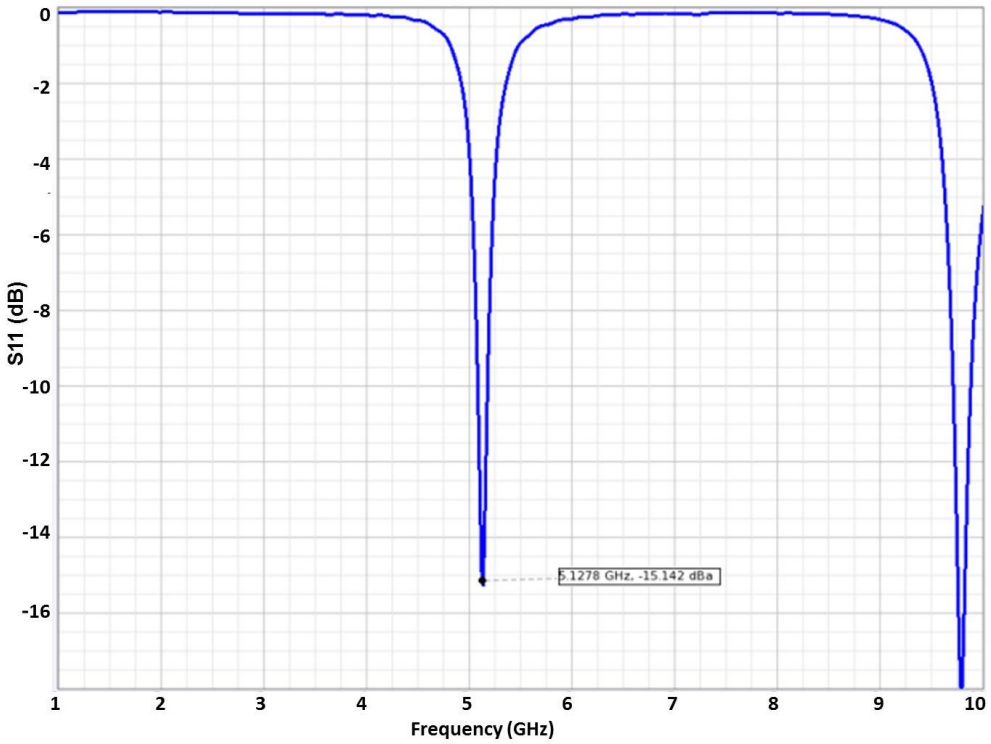

Figure 4.16 S11 for the 5.1 GHz Patch Antenna in free space (-12 dB reflection coefficient)

4.2.6 5.2 GHz Monopole Antenna

It is known that the length of the monopole is $\lambda/4$ and for frequency of 5.25 GHz, the length of the monopole equals 14.28 mm for infinite ground plane. However, for practical reasons, the counterpoise surface used is 40mm × 40mm. We have found that the antenna shown in Figure 4.18 with wire length of 15.8 mm soldiered normally with a 50 Ohm microstrip line to minimize coupling fields' effects. This microstrip line is then extended to an SMA feed connector and found to produce the desired resonance frequency with -16 dB reflection coefficient. The simulated reflection coefficient, however, for this 5.2 GHz monopole antenna with 7.5 mm wire length is plotted in Figure 4.17 where the antenna is matched to 50 Ohm. The measured reflection coefficient (-16 dB) was found to agree fairly with the simulated one and the thus is not included. The free space antenna gain is 3 dBi.

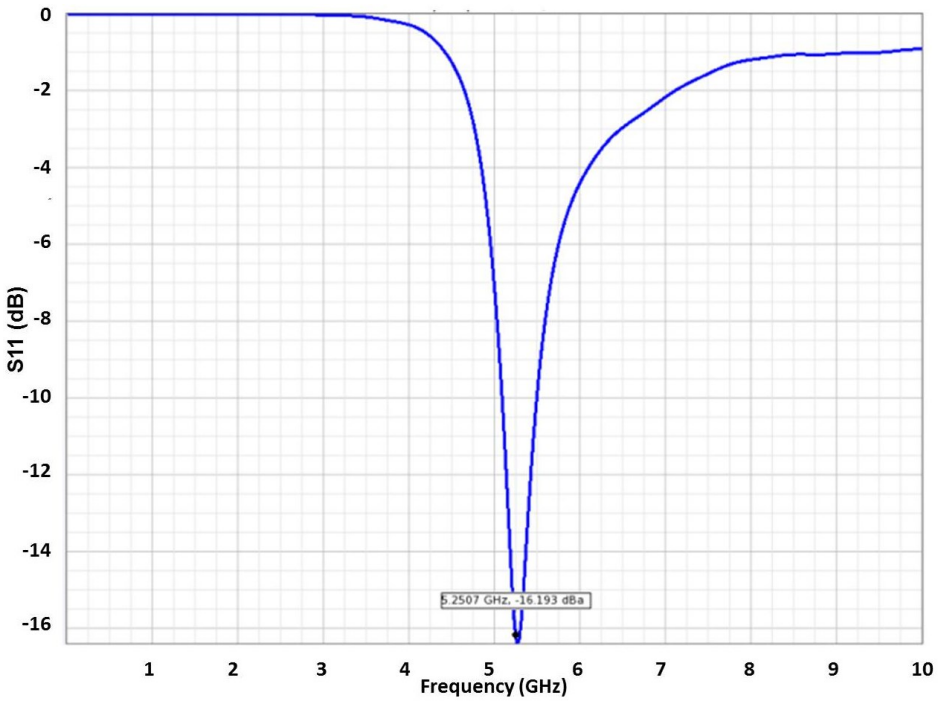

Figure 4.17 S11 for the 5.25 GHz Monopole Antenna in free space (-16 dB reflection coefficient)

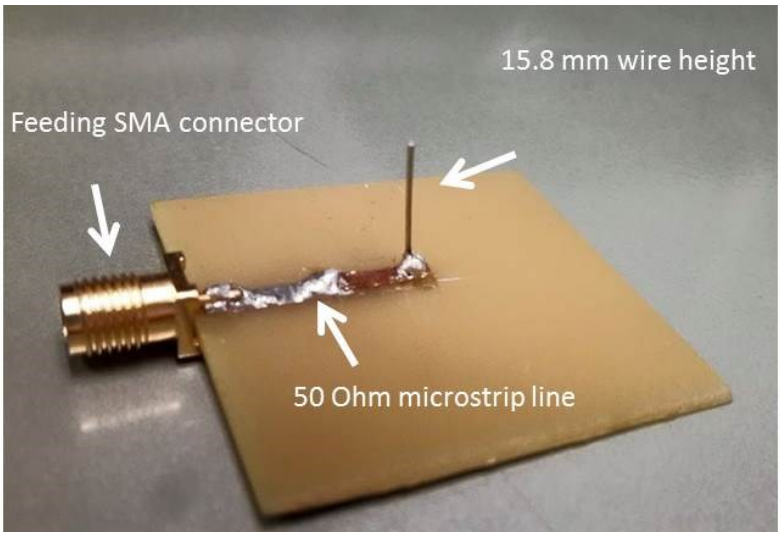

Figure 4.18 Configuration of 5.2 GHz monopole for intra-space suit path loss measurements

The rest of antennas not illustrated previously are shown in Figure 4.19. Antenna dimensions are provided in Table 4.3 and theoretical performance parameters are summarized in Table 4.4.

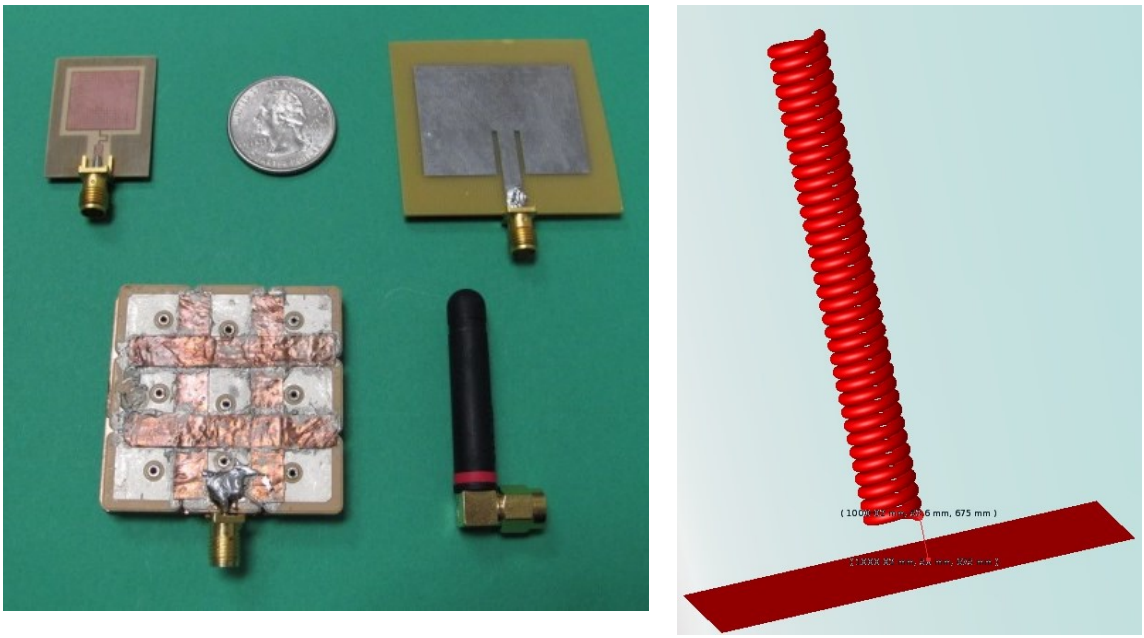

Figure 4.19 (left) Antennas used from left to right: (top) 5.2 GHz patch, 2.4 GHz patch, (bottom) 433 MHz patch, and 433 MHz helical monopole antenna, (right) 433 MHz helical monopole with 3.5 cm × 2 cm counterpoise

Table 4.3 Dimensions of antennas used

Antenna	Dimension of Antenna
5.2 GHz Patch	21.74×29.92× 0.8128 mm
5.2 GHz Monopole (simulation)	7.5 mm wire long normal on 40 mm×40 mm counterpoise
5.2 GHz Helical Monopole (measurements)	15.8 mm wire monopole with 40 mm×40 mm counterpoise
2.4 GHz Patch	46.02×42.53×1.5748 mm
2.45 GHz Monopole (simulation)	36 mm wire length and 40 mm×40 mm counterpoise
2.4 GHz Helical Monopole (measurements)	38 mm helical monopole long [87]
433 MHz Patch	48.05×34.17×1.5748 mm
433 MHz Helical Monopole (simulation)	Helical shape with 36 threads, 2 mm radius, 40.9 mm height
433 MHz Helical Monopole [86] (measurement)	39 mm height

Table 4.4 Performance characteristics of antennas in free space

Antenna	Reflection coefficient	10 dB bandwidth	Free space gain
5.2 GHz Patch	-15 dB	70 MH	4.2 dBi
5.2 GHz Monopole	-16 dB	160 MHz	3 dBi
2.4 GHz Patch	-10 dB	50 MHz	4.2 dBi
2.4 GHz Monopole	-25 dB	180 MHz	2.2 dBi
433 MHz Patch	-3 dB	1.77 MHz	1.9 dBi
433 MHz Helical Monopole	-16 dB	22 MHz	1.64 dBi

4.3 Small-Scale Performance Evaluation[5]

After characterizing the antennas that will be used in path loss measurements, path loss evaluation was conducted for three propagation environments: antennas in free space, antennas on-body, and antennas on-body and inside the space suit. Applicability and feasibility of commercial off-the-shelf antennas for this unique propagation environment were also investigated. On-body antennas in WBANs play a crucial role in determining quality of service. Several antenna designs have been proposed for body-centric wireless communications [88]. In particular, polarization of launched waves is one antenna feature found to significantly affect path loss values. For example, Norton surface waves in on-body channels and associated vertical polarization result in electric fields that are more strongly received and less path loss [89].

In this Section, the vertically (monopole and helical monopole) and horizontally (microstrip patch antenna) polarized antennas presented in Section 4.2 are investigated in the context of astronaut body area network. Effects of polarization and frequency on the path loss performance metric are also studied. Path loss is chosen as the primary criterion because wave reflections inside this unique intra-spacesuit environment are minimal.

4.3.1 *Simulation of Loss in Free Space, On-Body, and Intra-Space Suit*

4.3.1.1 Simulation Setup and Results

Next, we quantify the performance of all four antennas within an arm section of a space suit through computational EM simulations. Simulation setup consists of a section of a human

---

[5] *Copyright 2014 IEEE*. Portions of section 4.2 are reprinted with permission from Taj-Eldin, M.; Kuhn, W.; Natarajan, B.; Peterson, G., "Investigation of practical antennas for astronaut body area network," *Wireless for Space and Extreme Environments (WiSEE), 2014 IEEE International Conference on* , vol., no., pp.1,7, 30-31 Oct. 2014

arm within an aluminum outer layer to mimic the space suit. As shown in Figure 4.20, Tx and Rx antennas were mounted on the arm (with no antenna-body separation distance), and both ends remained open with one base cell as free space padding at each end of the aluminum tube. Free space padding of only one base cell is chosen to minimize the effect of impedance discontinuity on S-parameter simulation results. The simulation box uses eight layers of Perfect Matched Layer PML as the boundary conditions.

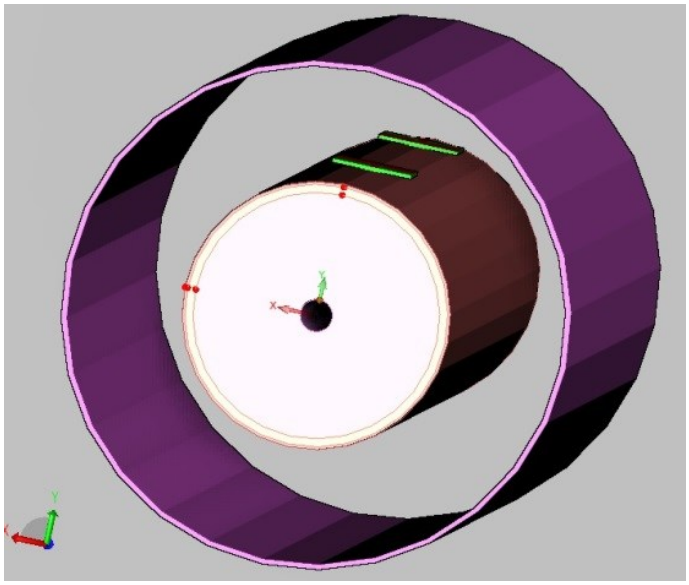

Figure 4.20 Simulation setup for two antennas placed on human arm inside a section of space suit

Keysight EMPro's FDTD-based solver is used to simulate S21 parameter according to each frequency, 433 MHz, 2.4 GHz, and 5.2 GHz, with the exception of the S21 simulation that used 433 MHz helical monopole antenna. Thanks to the curved structure of helical monopole, the FEM-based solver is more efficient for the 433 MHz helical monopole. In the FDTD simulation, the simulator automatically set the timestep based on minimum cell size in the entire simulation domain. In most cases, the fields of interest converge sufficiently for antennas applications, using a threshold of -30 dB in which undesired reflections from the perfect matched layer (PML)

boundary conditions are excluded. Results of FDTD simulations are obtained by taking a Fourier Transform of transient fields excited by a pulse waveform.

The following sections present simulated forward transmission gain (S21) curves for four cases for each antenna at specific frequencies. The four cases corresponded to four distances between the transmit and receive antennas, (1) 100 cm, (2) 115 cm, (3) 130 cm, and (4) 145 cm, in order for 433 MHz and 2.4 GHz antennas investigate the S21 profile in the far-field and avoid near-field effects. However, distances chosen for transmission gain simulations using 5.2 GHz antennas are 15, 30, 45, and 60 cm, which are sufficient for far-field region at this short wavelength.

Simulations are repeated for four distances in order to accurately estimate path loss per 15 cm of arm length via differencing. Differencing of explicit path loss values helps isolate other loss effects and antenna gains that are not of direct interest in this work.

433 MHz Microstrip Patch Antenna

Figure 4.21 demonstrates the S21 curve using helical monopole antenna for three scenarios; antennas in free space, antennas on body with zero body distance, and antennas on-body but inside the aluminum tube simulating the TMG layers of space suit segment.

The path loss when the antennas are in free space is 145 dB whereas it equals to 140 dB when antennas on-body environment. Finally, the path loss is further reduced by 80 dB when the intra-space suit propagation environment is utilized.

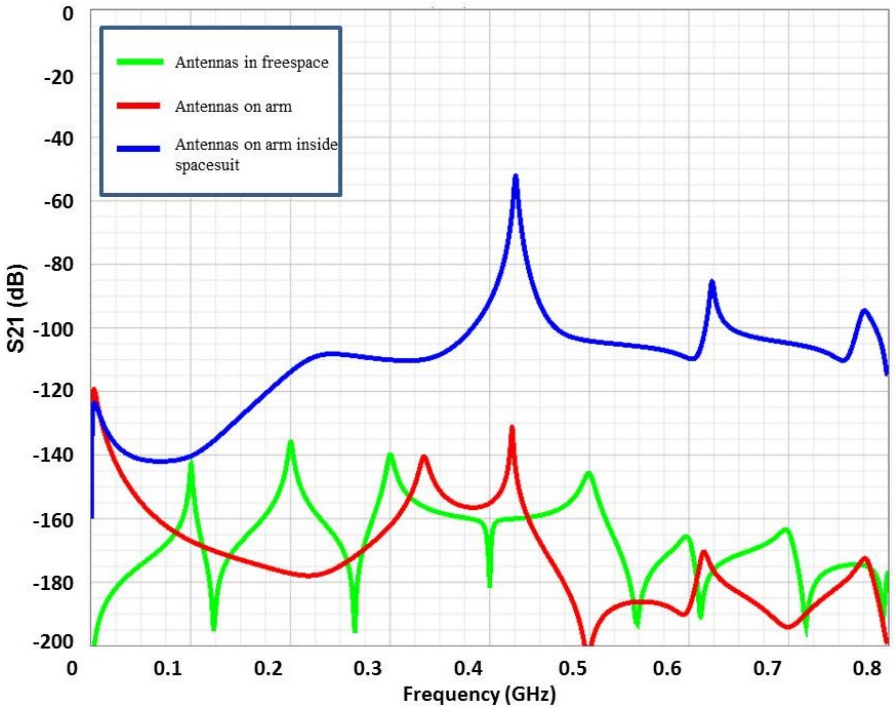

Figure 4.21 S21 graph for 100 cm separation with two 433 MHz patch antennas for three cases: free space (green), on arm (red), and on arm with suit (blue) (145, 140, and 60 dB)

Path loss within an intra-space suit arm segment is observed for varying Tx-Rx distances, as shown in Figure 4.22. Results show that path loss for the first 15 cm arm length (calculated as the difference between 115 cm simulated loss (54.5 dB) and 100 cm simulated loss (47.5 dB)) equals 7 dB. Similarly, path loss for the second 15 cm arm length (calculated by taking the difference of simulated loss for 130 cm (57 dB) from simulated loss for 115 cm distance (54.5 dB)) equals 2.5 dB. In addition, path loss for the third 15 cm arm length is 4.6 dB and average path loss is approximately 4.7 dB/15 cm.

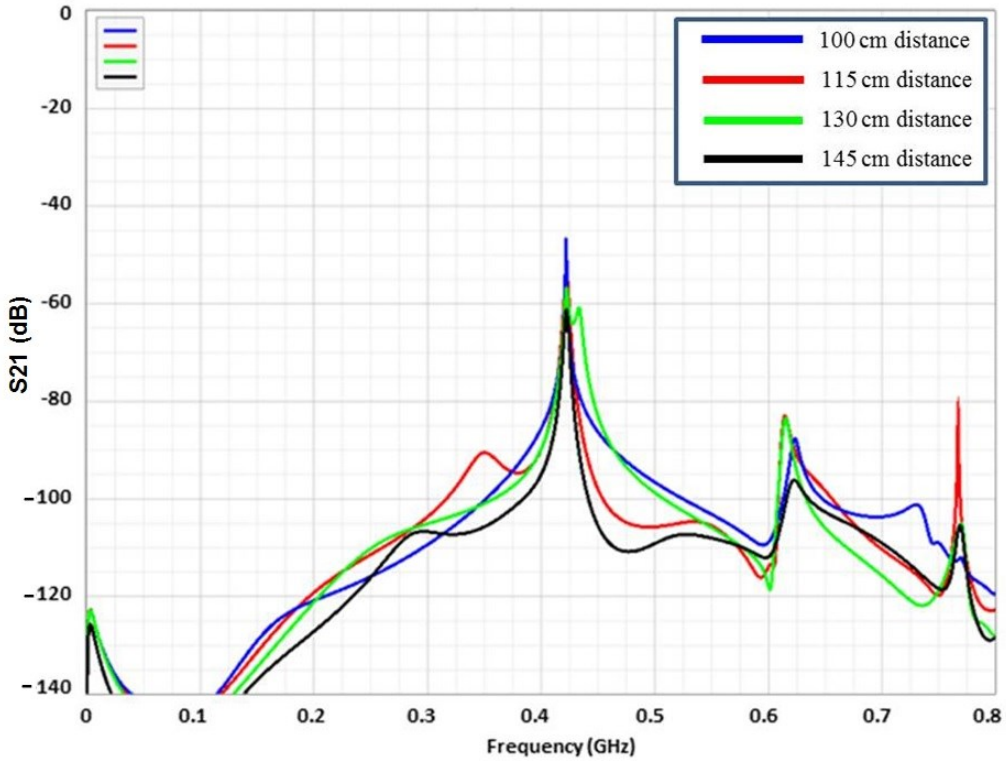

Figure 4.22 S21 curve for two 433 MHz patch antennas for four antenna distances: 100, 115, 130, and 145 cm with corresponding values of 47.5, 54.5, 57, and 61.6 dB, respectively

Comparison of path loss produced using 433 MHz monopole and patch antennas reveal that path loss produced using monopole antenna is approximately 2.3 dB lower for 15 cm arm length. This observation is expected because monopole antennas produce vertical polarization, resulting in stronger received electric field that equals the sum of direct wave and reflected waves from the aluminum tube surface. However, insertion into the suit environment made the monopole more susceptible to detuning, a potentially problematic behavior.

433 MHz Helical Monopole Antenna

Propagation characteristics are initially evaluated with 433 MHz helical monopole and patch antennas. Spacing between the arm and space suit is approximately 4.5 cm (approximately 0.5 cm greater than monopole height). Figure 4.23 demonstrates the forward transmission gain (S21) curve using helical monopole antenna for three scenarios; antennas in free space, antennas on body with zero body distance, and antennas on-body but inside the aluminum tube simulating the TMG layers of space suit segment.

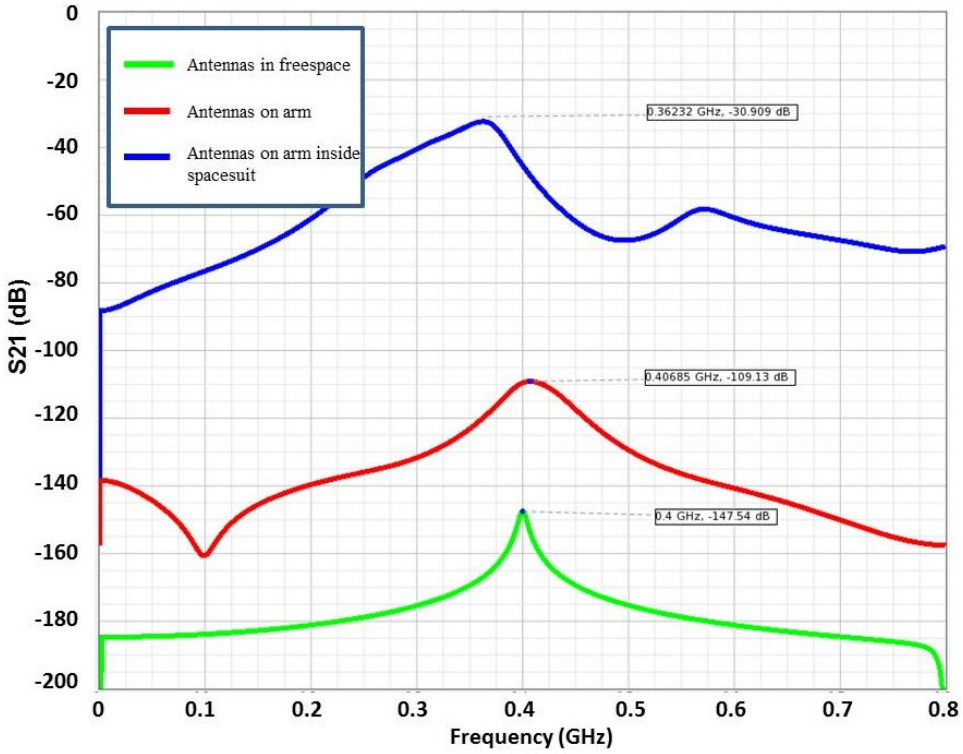

Figure 4.23 S21 graph for 100 cm separation with two 433 MHz helical monopoles for three cases: on free space (green), on arm without suit (red), and with suit (blue) (147, 109, and 31 dB)

It can be noticed that the resonance frequency is detuned to 360 MHz due to change in antenna impedance resulting from the contact of helical monopole ground plane with the human

body. Also, the path loss when the antennas are in free space is 147 dB whereas it equals to 109 dB when antennas on-body environment. Finally, the path loss is further reduced to 31 dB when the intra-space suit propagation environment is utilized.

Next, the purpose is to quantify the path loss in dB per cm arm length. Thus, to get an insight, we need to simulate the path loss in the far-field between Tx-Rx path. For example, 100 cm is adopted which is greater than $\lambda/2$ in free space medium and it can be noticed that the path loss for the first 15 cm arm length (simulated loss of 115 cm minus simulated loss of 100 cm case) is 2 dB whereas the path loss for the second 15 cm arm length is 3.1 dB as can be seen in Figure 4.24.

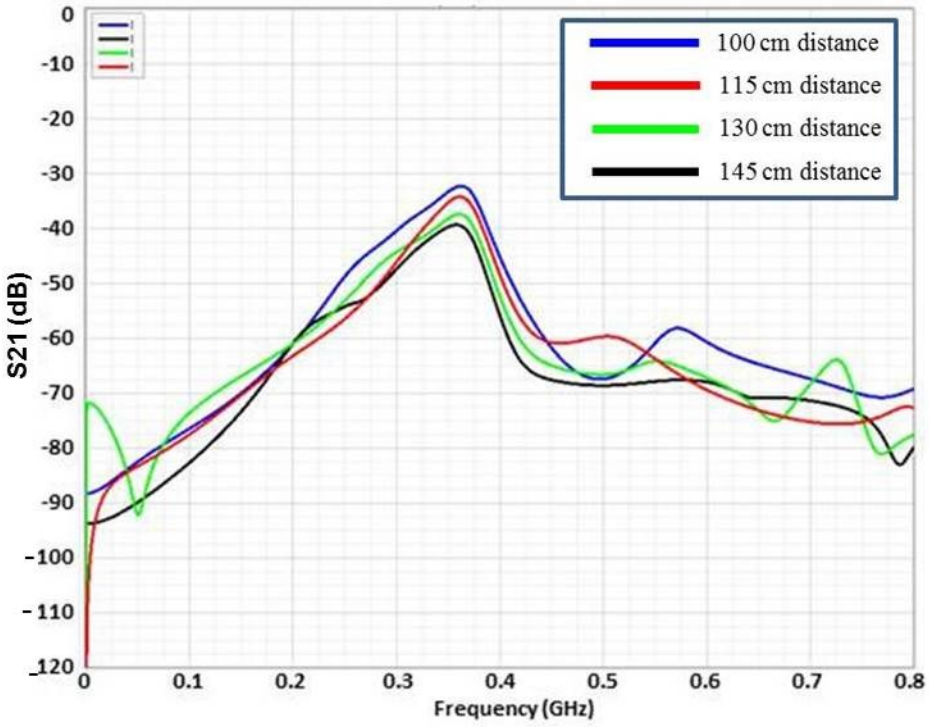

Figure 4.24 S21 curve for 30 cm separation with two 433 MHz helical monopole antennas for four antenna separation distances: 100, 115, 130, and 145 cm with corresponding values of 32.2, 34.2, 37.3, and 39.3 dB, respectively

However, path loss for the third 15 cm arm length is 2 dB. Mean path loss of the three values is approximately 2.4 dB/15 cm.

2.4 GHz Microstrip Patch Antenna

Intra-suit propagation characteristics of 2.4 GHz radio channel using a patch antenna is shown in Figure 4.25. The figure shows that path loss for the first 15 cm (calculated as the difference between simulated loss at 115 cm (30.5 dB) and simulated loss at 100 cm (25.8 dB)) equals 4.7 dB/15 cm.

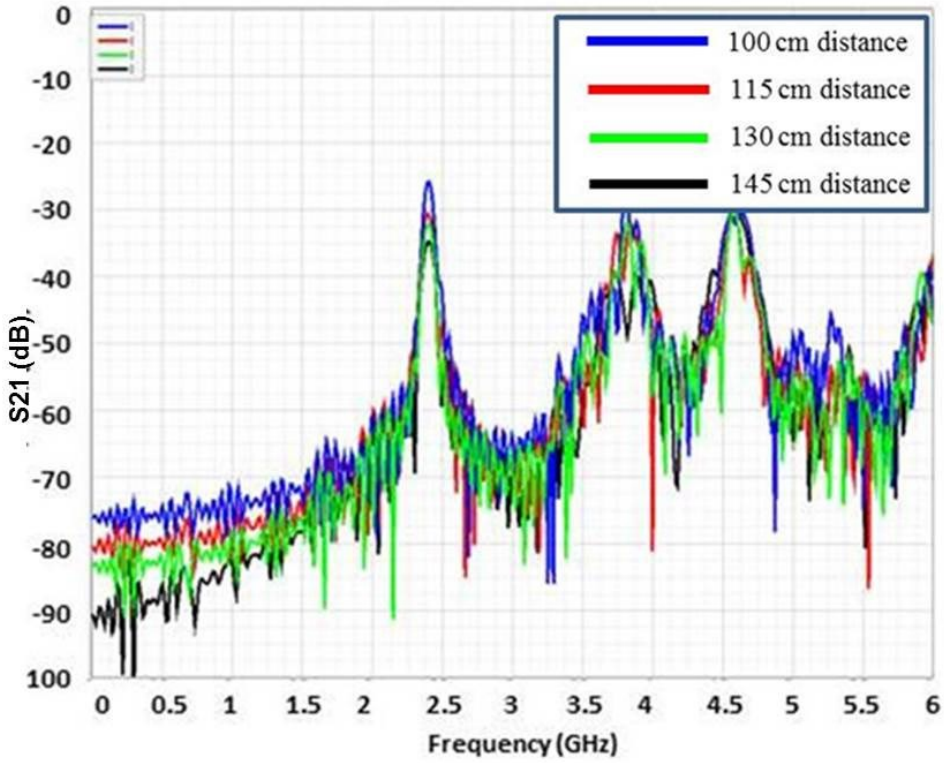

Figure 4.25 S21 curve for two 2.4 GHz patch antennas for four antenna distances: 100, 115, 130, and 145 cm with corresponding values of 25.8, 30.5, 32.2, and 34.7 dB, respectively

Similarly, path loss for the second 15 cm arm length (calculated as the difference between 32.2 dB and 30.5 dB, equaling 1.7 dB, and path loss for the third 15 cm arm length) is 2.5 dB. Mean path loss is approximately 3 dB/15 cm.

5.2 GHz Microstrip Patch Antenna

As seen in Figure 4.26 (green curve), the path loss with patch antennas in free space for 30 cm antenna-separation distance is 52 dB at 5.2 GHz. However, path loss reduces by 10 dB when antennas are positioned on the arm with zero antenna body separation (see red curve). Path loss is further reduced by 12 dB when antennas are on the body but inside the space suit structure, proving that the space suit material benefits the propagation environment.

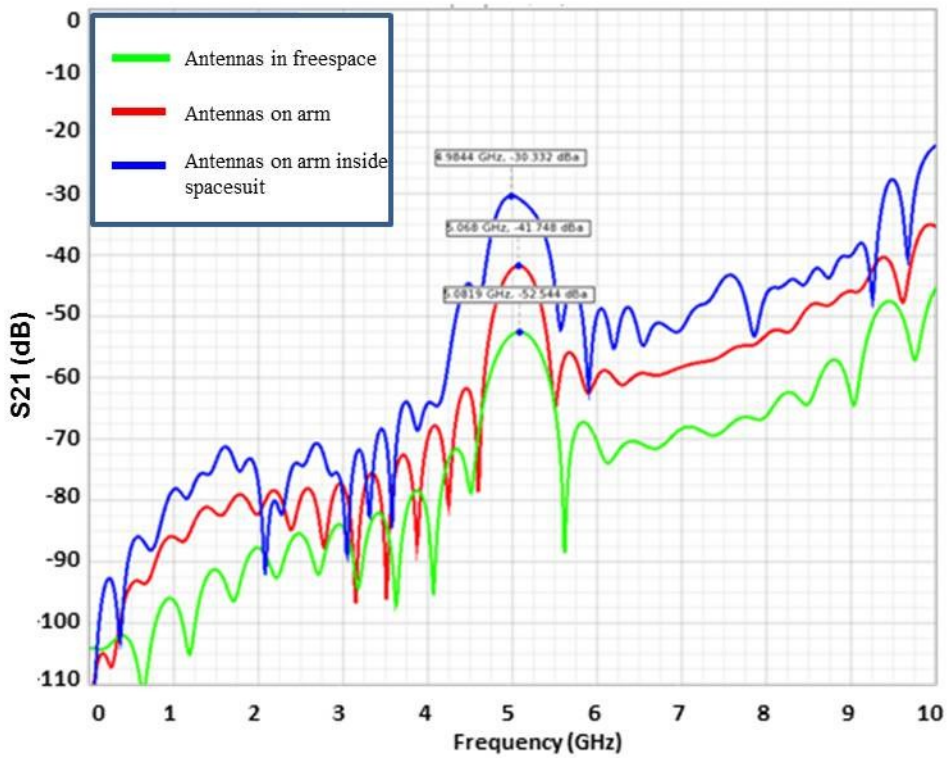

Figure 4.26 S21 graph for 30 cm separation with two 5.1 GHz patch antennas for three cases: in free space, on arm, on arm with suit (52, 42, 30 dB)

The impact of using a 5.2 GHz patch antenna to launch signals within a space suit is evaluated and shown in Figure 4.27. Results show that path loss for the first 15 cm (difference

between simulated absolute loss of 30 cm and absolute loss of 15 cm distance) is approximately 8.4 dB. Loss for the second 15 cm arm length is 6 dB and loss for the third 15 cm arm length is 2.3 dB leading to an average path loss of 5.6 dB/15 cm.

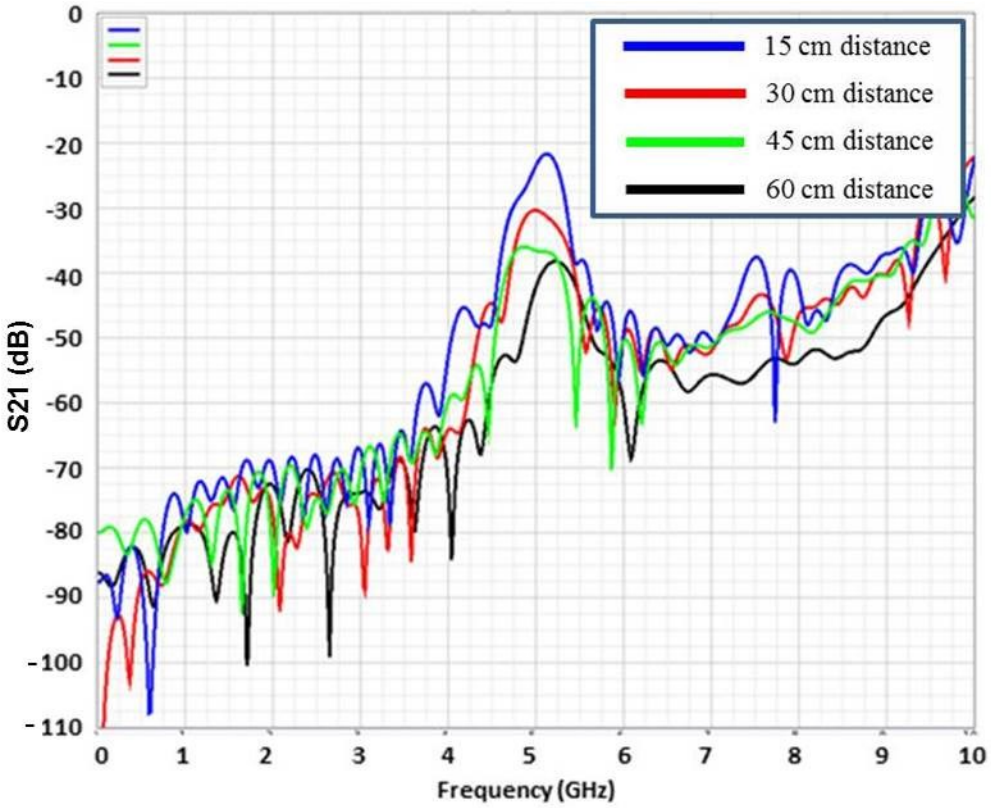

Figure 4.27 S21 curve for two 5.2 GHz patch antennas for four antenna separation distances: 15, 30, 45, and 60 cm with corresponding values of 21.6, 30, 36, and 38.3 dB, respectively

5.2 GHz Helical Monopole Antenna

For a 5.2 GHz helical monopole, path loss in free space is 38.5 dB (Figure 4.28, green curve) and decreases to 32 dB when antennas are mounted on arm model as shown in Figure 4.28 (red curve). Path loss further reduces to an average of 25 dB when the arm is inserted into a section of space suit (blue curve).

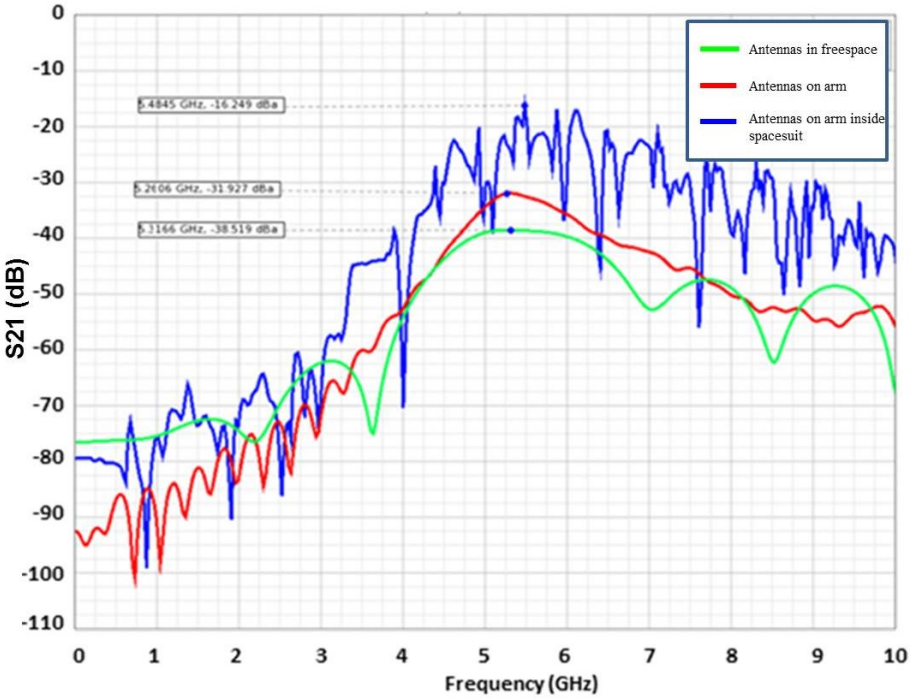

Figure 4.28 S21 graph for 30 cm separation with two monopole antennas for three cases: in free space, on arm, on arm with suit (38.5, 32, 25 dB)

Path loss in intra-space suit environment for the first 15 cm (loss at 30 cm minus loss at 15 cm) corresponds to 2.4 dB, as shown in Figure 4.29. Loss for the second 15 cm segment is 7 dB which leads to an average path loss of 4.7 dB per 15 cm distance. However, given the large variance with shifts in frequency, this value is only a guide. In general however, the 5.2 GHz frequency is seen to provide good propagation performance with minimal losses except within the deep fades.

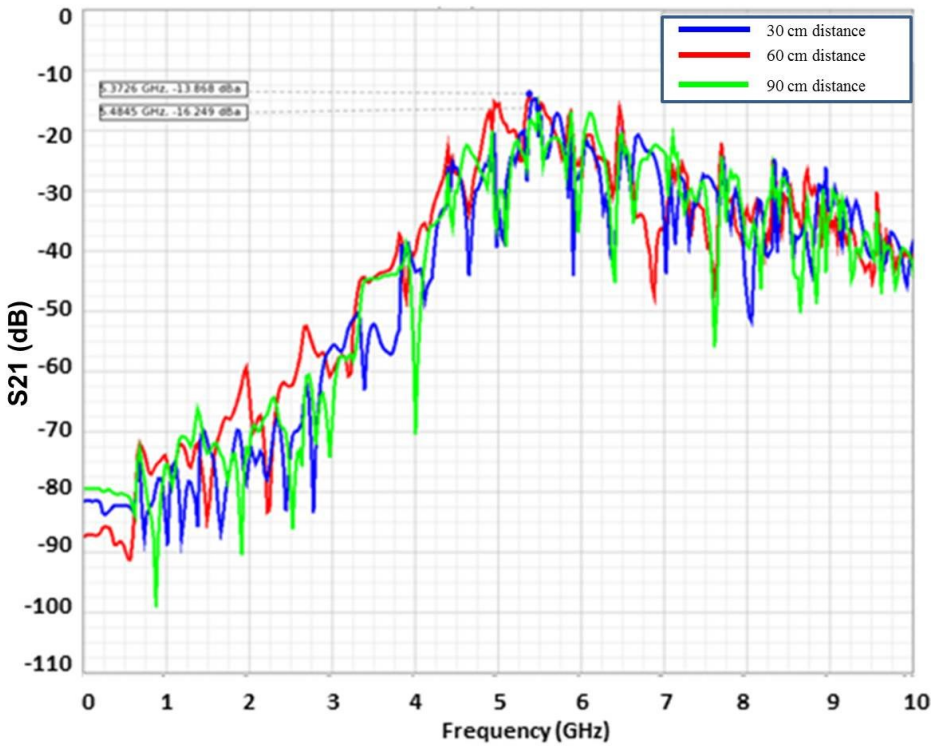

Figure 4.29 S21 graph for two 5.25 GHz helical monopole antennas for three antenna separation distances: 15, 30, and 45 cm (13.8, 16.2, 16.4 dB)

Path loss values using all described antennas for three scenarios: Total loss for antennas in free space, on-body, and on-body but inside space suit segment are summarized in Table 4.6. It should be noted that the simulated total loss for 433 MHz antennas is 100 cm whereas the Tx-Rx distance is only 30 cm.

It can be noticed from Table 4.5 that the total loss is 145 dB when 433 MHz patch antenna is placed in free space whereas it is 147 dB when helical monopole is used whereas it equals 52 dB for 5.2 GHz patch and 38 dB for 5.2 GHz helical monopole. This excessive loss observed for 433 MHz patch antenna is expected due to having the antenna placed conformal to human body which forms a maximum radiation pattern vertical to the surface of body and a null on the surface parallel to the body surface. For the case of 433 MHz helical monopole, the

excessive loss seen can be partially attributed to the small size counterpoise (3.5 cm × 2 cm shown in Figure 4.19 (right)) compared to the wavelength (i.e., 692 cm). In other words, effectively, there is no counterpoise point which means that the helical monopole is practically not radiating.

It can be notice that total loss is reduced when the 433 MHz patch antenna is placed on arm segment by 5 dB. On the other hand, the total loss is reduced by 38 dB for the case of 433 MHz helical monopole. Then, the total loss is further reduced by 80 dB when the 433 MHz patch antennas with arm are inserted inside a space suit segment. However, the total loss is reduced by 78 when the 433 MHz monopole placed on arm are both inserted into space suit segment.

Conversely, for case of 5.2 GHz patch antenna, the total loss decreases by 10 dB when antennas are positioned directly on the arm whereas it decreases by 6.5 dB when 5.2 GHz monopole antennas are positioned on the arm.

On the other hand, the loss reduction is 12 dB when the 5.2 GHz patch antenna is placed in intra-space suit environment while the loss decreases by 7 dB when the 5.2 GHz helical monopole is used in intra-space suit structure as summarized in Table 4.5.

Table 4.5 Total loss values for free space, on-body, and intra-suit environment

Antenna and Frequency	Total loss for Free space (dB)	Total loss for On-body (dB)	Total loss for intra-space suit (dB)
433 MHz Patch	145	140	60
433 MHz Helical Monopole	147	109	31
5.2 GHz Patch	52	42	30
5.2 GHz Helical Monopole	38.5	32	25

In addition, path loss values per 15 cm unit length for intra-space suit propagation environment are summarized in Table 4.6.

Table 4.6 Path loss values for intra-space suit environment at various frequencies

Antenna and Frequency	Path loss per 15 cm arm length (dB)
433 MHz Monopole	2.4
433 MHz Patch	4.7
2.4 GHz Patch	3
5.2 GHz Patch	5.6

Discussion

In Section 4.1.2, we hypothesized that the electric and magnetic fields will follow TEM mode as illustrated in Figure 4.9 where the electric field will be normal to the arm (inner conductor) and the magnetic field will be is tangential to the surface of the arm. This hypothesis is later validated in Section 5.3 of Chapter 5 using a top-hat monopole antenna. We hypothesize that the electric and magnetic field will also follow TEM coax structure in the far-field as shown in Figure 4.30.

However, the simulation results for the 5.2 GHz monopole shown in Figure 4.29 appear to deviate significantly from those at lower frequencies. This could be due to high order multi-modes in which the signal is now mostly propagating in the space between the body and the metal shield, reducing the path loss per unit length in this case.

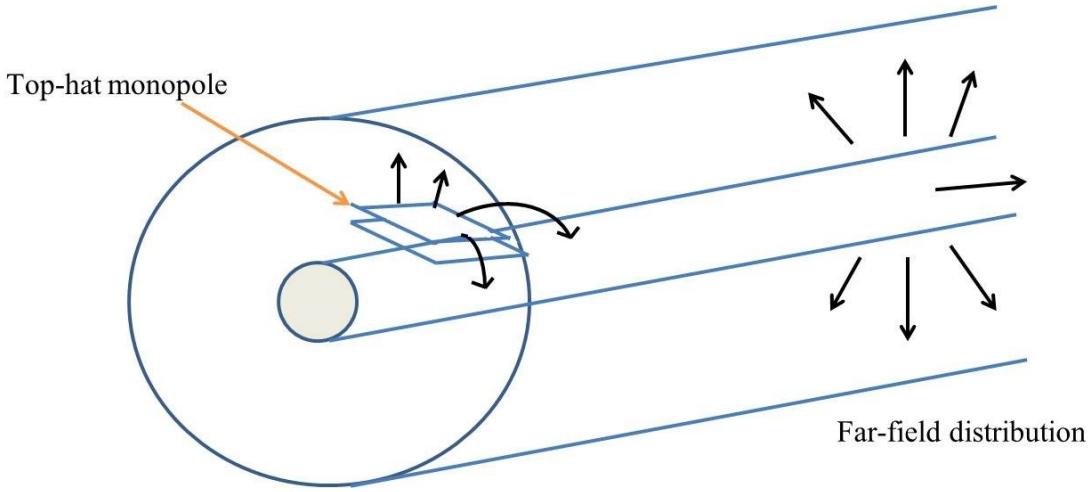

Figure 4.30 Anticipated electric and magnetic field distribution of antenna in the far-field originated from the top-hat monopole on the left

Simulation results suggest the following:

a) Path loss decreases when antennas are placed on the human body due to the conductive nature of body tissues especially muscle that containing high percent of water.

b) Path loss is further reduced when the antennas with the human arm model are both encapsulated with its space suit segment.

c) Path loss within a space suit generally increases with higher frequency channels. However, simulated path loss using 433 MHz patch antenna did not agree with this conclusion, as shown in Table 4.5. Since the path loss calculation method implicitly removed antenna mismatch losses, the disagreement may be due to the mismatch between horizontal polarization of the patch and vertical polarization of the channel below the multi-mode frequency. Electrically small antennas

also suffer from narrow bandwidths (-3 dB reflection coefficient and 1 MHz bandwidth), so the simulation graphs may be misleading.

d) Helical monopole antennas that use vertical polarization produce less channel loss but show more detuning inside the suit. Path loss is 2.3 dB lower for the 433 MHz helical monopole than the 433 MHz patch antenna because the helical monopole is able to launch signals that followed TEM mode in a coaxial transmission line. However, the benefit of using the 433 MHz monopole is negated by impracticality. In order to decrease intrusiveness for the astronaut, it might be preferable to use an antenna that is conformal to the body.

e) The results for the 5.2 GHz helical monopole are encouraging, suggesting this antenna may provide a good solution if it could fit within a sensor without being too tall.

4.3.2 Experimental Validation

In order to validate results obtained using simulation, experiments performed in the laboratory utilized an HP network analyzer to measure signal attenuation versus frequency. Tx-Rx antenna distances used in the experiments differ from distances used in the simulations. In the experimental environment, distances are limited by dimensions of the human body. A real human arm is used for subject measurements and experiments are performed with the person's arm inserted into a metal tube, as shown in Figure 4.31. The purpose of simulations in the far-field was to determine if channel loss follows a similar trend for dB per 15 cm length of arm.

Path loss measurements with a patch and monopole for 433 MHz and patch for 2.4 GHz and 5.2 GHz frequencies are presented. Within the experimental setup described earlier, two holes are drilled to allow cables to be inserted into the tube, one for each antenna. These two holes are separated by 30 cm for the initial case and then separated by various distances for

subsequent cases. The center-lead of each cable is connected to the desired antenna and the shield is connected to the outer aluminum tube to avoid significant radiation from the coax. Antennas are mounted directly on the human body.

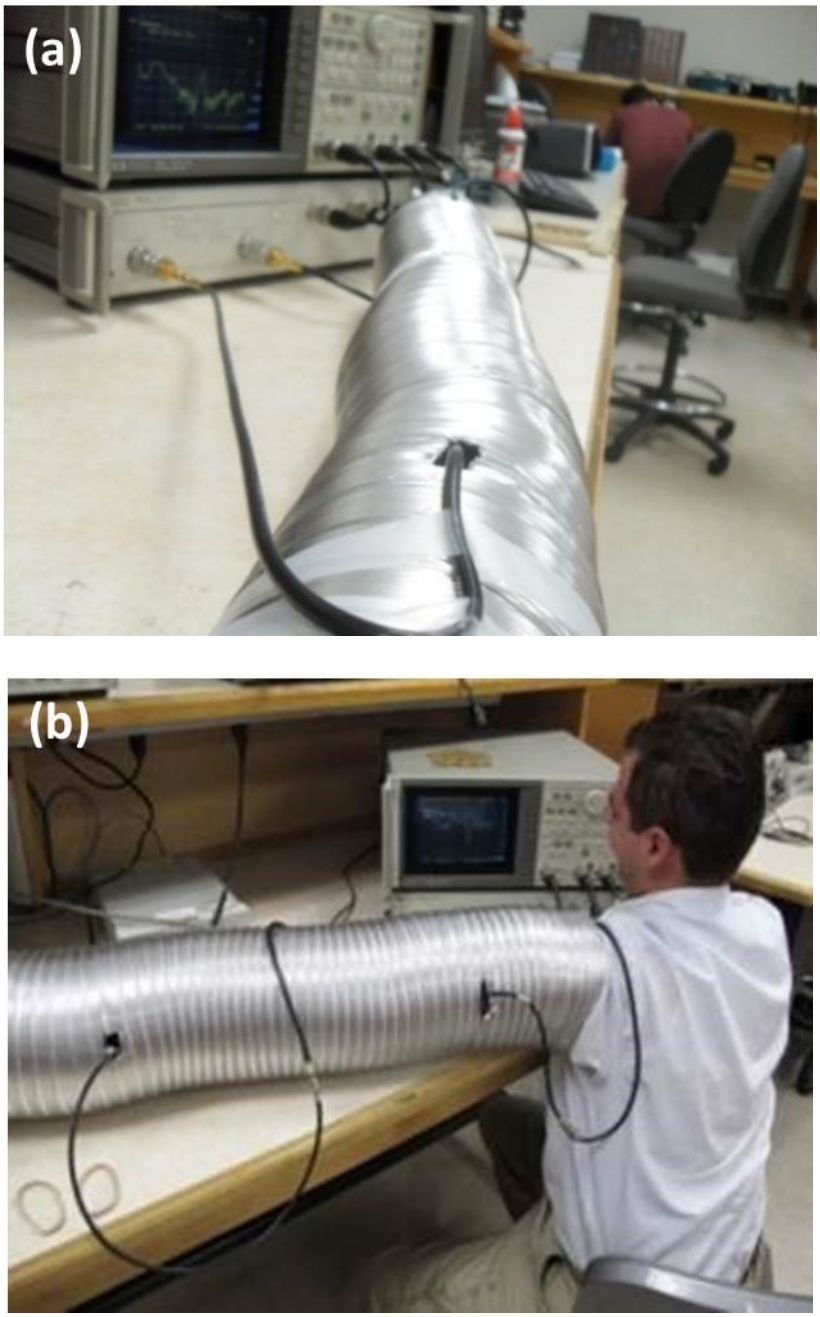

Figure 4.31 (a) Measurement setup with feeding cables orthogonal to each other, (b) inserting arm with small antennas mounted directly on arm

Path loss compared to the absolute value of S21 parameter when S21 was negative. Tables 4.7 and 4.8 present measurements results for four scenarios: (1) antennas on arm with separation distance of 30 cm, (2) antennas on arm and inside a section of space suit with a distance of 30 cm, (3) antennas on arm and inside a section of space suit with a separation distance of 15 cm and (4) antennas on arm and inside a section of space suit with a separation distance of 45 cm. Path loss for 60 cm could not be measured because this distance exceeds the length of typical human arms.

First, path loss for radio channel with 433 MHz antennas is presented. Table 4.7 shows measured median total loss values for monopole and patch antennas, respectively. The median path loss is recorded since it represents the most typical loss. However, mean loss does not represent, as with respect to loss in on-body wireless propagation that can be skewed by large instantaneous path loss values. Measured total loss when antennas are on the arm is 33 dB for helical monopole and 46 dB for patch antenna. Total loss is reduced by 8 dB when the arm is inserted into a section of space suit with helical monopole and total loss is reduced by 11 dB for patch antenna. Table 4.7 shows that total loss values using monopole antenna are approximately 10 dB lower relative to a patch antenna with separation distance of 30 cm. In order to isolate secondary effects and better estimate path loss due to channel, we take the difference of total loss values of 30 cm and 15 cm distance as 2 dB for helical monopole and 7.3 dB for patch antenna. For the next 15 cm distance, path loss values obtained by subtracting values for 45 cm and 30 cm distances is presented. Specifically, the difference in absolute loss between 45 cm and 30 cm is 5 dB for helical monopole and 2.5 dB for patch antenna.

Table 4.7 Measured median total loss for 433 MHz monopole and patch antennas

Separation distance and propagation environment	433 MHz Helical Monopole (Measured)	433 MHz Patch (Measured)
30 cm on arm	33 dB	46 dB
30 cm in intra-space suit	25 dB	35 dB
15 cm in intra-space suit	23 dB	27.7 dB
45 cm in intra-space suit	30 dB	37.5 dB

Previous experiments are repeated using 2.4 GHz patch antenna and the results are presented in Table 4.8.

Table 4.8 Measured median total loss for 2.4 GHz and 5.2 GHz antennas

Separation distance and propagation environment	2.4 GHz Patch Antenna (Measured)	5.2 GHz Patch Antenna (Measured)
30 cm on arm	39 dB	43 dB
30 cm in intra-space suit	27 dB	29.7 dB
15 cm in intra-space suit	22 dB	19.5 dB
45 cm in intra-space suit	34 dB	39 dB

Compared to 433 MHz antennas, total loss values are lower with a 2.4 GHz patch antenna. Use of 433 MHz antennas should produce coaxial propagation structure (TEM mode), but losses resulted from the use of 433 MHz patch was not less than loss of 2.4 GHz patch antenna. This is because 433 MHz patch antennas have very lossy dielectric material and resonant frequency is massively detuned due to reflections from the surface inside the space suit. Antenna bandwidth at low frequency is narrow, thereby producing sharp peaks in S21 curves.

Next, Path loss in 5.2 GHz radio channel is investigated based on 5.2 GHz patch antenna and results are presented in Table 4.8 (last column). A comparison of total loss produced when antennas are mounted on arm without suit and with suit reveal that absolute loss is lower (by nearly 13.3 dB) when the arm with antennas is inserted into the cylindrical model of the space

suit. However, these values do not include other loss effects. Therefore, path loss for the first 15 cm distance is computed by subtracting total loss for the 30 cm distance from the value for the 15 cm distance, resulting in 10.2 dB/15 cm. Similarly, path loss for the second 15 cm distance is calculated as 9.3 dB. Compared to measurements with 2.4 GHz antennas, total loss values are much higher when higher frequencies are used. For example, measured total loss of antennas inside the suit is 29.7 dB with 5.2 GHz patch antenna, whereas it is 27 dB with 2.4 GHz patch antenna.

It is also important to alert the reader that although coaxial cables of the transmitter and receiver were set orthogonal to each other and cylindrical ferrite rods were inserted in the cable, experiments demonstrated that coaxial cables became a part of the antenna and changed the electric field pattern near the antenna.

In summary, experimental results agreed fairly well and confirmed findings from simulations:

1) Total loss decreases when the arm is inserted into a section of space suit. Therefore, the space suit supports launching coaxial signal propagation modes below the cutoff frequency.

2) Path loss using patch antenna with horizontal polarization generally increases with increase in frequency.

3) Use of vertical polarization to launch electromagnetic waves results in lower total loss compared to using horizontal polarization because vertical polarization complies with TEM propagation mode in coaxial transmission lines.

4.4 Chapter Summary

The first section of this chapter proposed two propagation structures inside the space suit arm segment with a human arm: loaded circular waveguide and coaxial cable model.

Simulation and experimental results show that the intra-space suit environment supports TEM propagation mode, but the hypothesized circular waveguide model was not valid. The second section of this chapter described an evaluation study of radio channel performance on a small-scale model consisting of an arm model with a corresponding arm segment of space suit at various frequencies and two types of antenna polarization.

Results indicate that channel performance, characterized primarily by path loss metric, improves when antennas are on-body compared to free space because of the partially conductive nature of the human body. Moreover, the intra-space suit environment is superior to the free space and on-body antenna scenarios.

Chapter 5 -Full Scale Intra-Space Suit Propagation

In this chapter, the small-scale investigation conducted in Chapter 4 is expanded into full-scale space suit model that incorporates an astronaut's entire body with space suit segments and partial breaks at body joints.

The goal of this chapter is to document the intra-space suit radio propagation channel in various frequency bands. In addition to studies of simplified paths to determine basic dB per unit length attenuation factors versus frequency, the full-scale propagation environment inside the space suit is investigated, taking into account changes in propagation behavior at astronaut body joints and at multi-port junctions such as where arms and legs meet the astronaut's torso. Path loss is once again used again as the primary evaluation metric because multi-path is minimal in this guided-wave environment. Simulation results from a simplified astronaut model with space suit are compared with experimental data taken from humans within a full-scale model suit.

5.1 Antenna/Transducer[6]

Launching and receiving intra-suit signals requires development of a suitable antenna/transducer for this unique intra-space suit WBAN environment because the environment can differ significantly from free space.

We utilized a top-hat monopole antenna/transducer is proposed in [8] (Figure 5.1) because of its design simplicity and conformability to the human body. As indicated in Chapter 4, vertically polarized antennas are preferred for on-body communications, especially within this environment. This transducer shown in Figure 5.1 creates this polarization and consists of a thin

[6] *Copyright 2013 IEEE*. Portions of section 5.1 are reprinted with permission from Taj-Eldin, M.; Kuhn, B.; Hodges, A.; Natarajan, B.; Peterson, G.; Alshetaiwi, M.; Ouyang, S.; Sanchez, G.; Monfort-Nelson, E., "Wireless propagation measurements for astronaut body area network," *Wireless for Space and Extreme Environments (WiSEE), 2013 IEEE International Conference on* , vol., no., pp.1,7, 7-9 Nov. 2013

wire 8 mm long. The wire connects two circuit boards, each 50 mm wide and 65 mm long. This antenna/transducer is not tuned to a certain frequency; instead it has a wide frequency response for coupling transmitted and received fields out of and into radios used in this chapter. Although it is not tuned to achieve optimum results at a specific frequency, this design offers desirable characteristics for path loss measurements over very high frequency (VHF) to ultra-high frequency (UHF) bands.

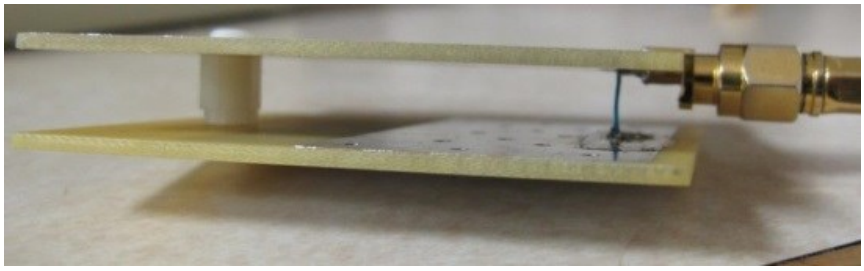

Figure 5.1 Top-hat monopole antenna

5.2 Antenna Mismatch and Circuit Board Loss Calculation

Before measuring and interpreting path loss values for various links as described earlier, it is important to isolate the losses associated with antenna mismatch and other factors. That is, it is important to acknowledge that measured path loss values include losses other than propagation loss. So, the total measured loss $L_{measured}$ can be expressed as:

$$L_{measured} = L_{path\ loss} + L_{additional} \tag{5.1}$$

where $L_{path\ loss}$ is the path loss, $L_{additional}$ is the additional loss which includes two terms: $L_{antenna-mismatch}$ and $L_{circuit\_loss}$. The term $L_{antenna-mismatch}$ is the loss due to impedance mismatch between the antenna impedance and impedance of the radio transceiver used which is typically 50 Ohm. $L_{circuit\_loss}$ refers to loss due to an attenuator (added to the 916 MHz board only) to change the range of signal levels that can be captured during experiments.

To estimate the additional losses involved, we perform a small scale test. In this experiment, the transmitter and receiver are mounted directly on the same side of the arm as shown in Figure 5.2. Then, the arm is inserted inside an aluminum tube that has electrical properties similar to that of a real space suit (Figure 5.3). The tube is 0.70 m long and has radius of 0.095 m. The air gap between the skin and the inner surface of tube is around 0.045 m, which is comparable to the space-suit.

Figure 5.2 Transmitter and receiver are mounted directly on arm with initial distance of 30 cm before the arm is inserted inside the tube.

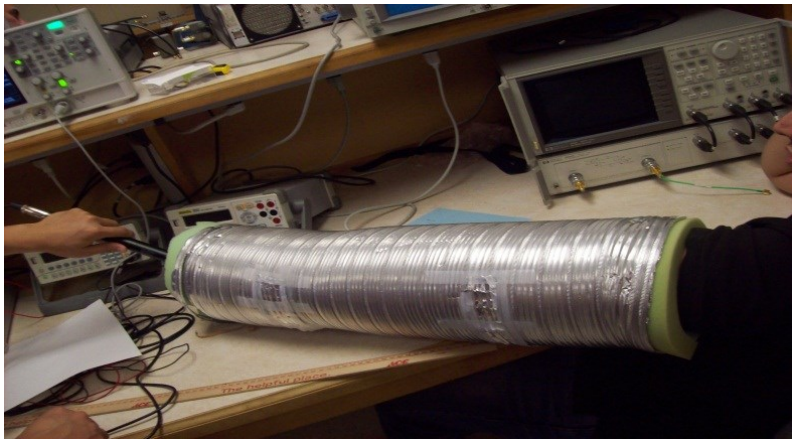

Figure 5.3 Measuring the total loss in small scale (arm).

We measure the total loss for Transmitter-Receiver distances of 15, 30 and 45 cm and then calculate the path loss ($L_{path\ loss}$) for 30 cm of arm length as the difference between the total measured loss ($L_{measured}$) for 45 cm distance and the total measured loss for 15 cm distance. The results of this experiment are presented in Table 5.1. (It can be noticed that the measured total loss for 315 MHz channel at 15 cm and 30 cm is the same. This happens due to the near-field effects.)

Table 5.1 Measured Total Loss and Path Loss

Frequency	$L_{measured}$ for 15 cm distance (dB)	$L_{measured}$ for 30 cm distance (dB)	$L_{measured}$ for 45 cm distance (dB)	$L_{path\ loss}$ for 30 cm arm length (dB)
315 MHz	37	37	41.3	4.3
433 MHz	38.4	41	45	6.6
916 MHz	34	45	56	22

The additional loss ($L_{additional}$) is computed in Table 5.2 using Eq. (5.1) as the difference between the measured total loss for 30 cm distance and the path loss computed for 30 cm arm length in the last column of Table 5.2. It should be noted that the additional loss (23 dB) for 916 MHz channel in Table 5.2 results from the difference between the measured loss (45 dB) and the 30 cm path loss (22 dB) since the attenuator loss (16 dB) is inherently present in the total loss measurement for 30 cm separation distance.

Table 5.2 Antenna Mismatch and Circuit Losses

Frequency	Measured total loss for 30 cm distance (dB)	Path loss for 30 cm of arm length (dB)	Additional loss (dB)
315 MHz	37	4.3	32.7
433 MHz	41	6.6	34.4
916 MHz	45	22	23

5.3 Intra-Suit Propagation Environment[7]

5.3.1 Small-Scale Model

As discussed in Chapter 4, a coaxial propagation structure is created for a small segment of space suit with a human arm in which the inner conductor is the human body and the outer conductor is formed by the multiple layers of TMG aluminized mylar.

5.3.2 Full-Scale Space Suit Model

In order to understand the propagation environment within a full-scale space suit, one must realize that the EMU suit is basically an assembly of multiple sections that can be connected for astronaut customization. This EMU suit has couplings at arm and leg joints, as shown in Figure 5.4. This subsection investigates the effects of couplings in EMU space suits in relation to coaxial structure impedance and radio propagation.

[7] *Copyright 2014 IEEE*. Portions of subsection 5.3.2 are reprinted with permission from Taj-Eldin, M.; Kuhn, W.B.; Fowles, A.H.; Natarajan, B.; Peterson, G.; Alshetaiwi, M.; Shuo Ouyang; Sanchez, G.; Monfort-Nelson, E., "Study of Wireless Propagation for Body Area Networks Inside Space Suits," *Sensors Journal, IEEE* , vol.14, no.11, pp.3810,3818, Nov. 2014

Figure 5.4 Sizing rings to customize the space suit

1) *Effects of breaks in TMG layer at space suit couplings*

Since TMG cover layer materials are laced to coupling rings and do not make electrical contact with them, capacitive coupling occurs between outer shields of two connected sections when EM waves propagate inside the space suit. Figure 5.5 demonstrates capacitance (C_b in Figure 5.8) between two space suit sections in which outer-conductor TMG layers and metal couplings overlap; Capacitive reactance Xc can be compared to coax characteristic impedance Zo in order to understand the effects of this non-zero impedance connection in the coaxial structure shield.

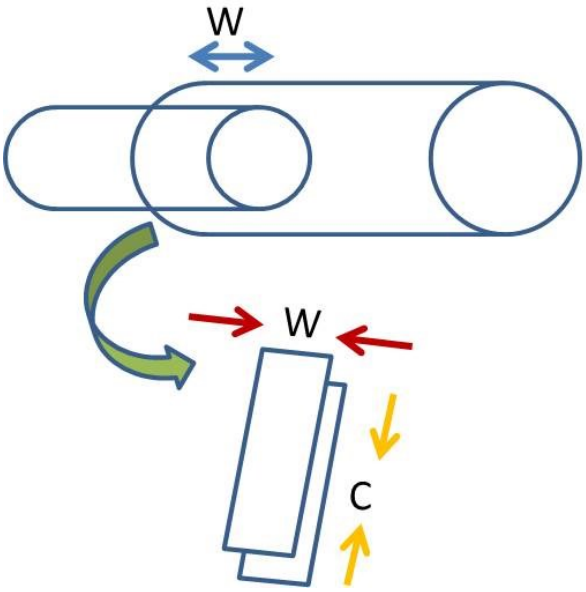

Figure 5.5 Capacitance created by the vertical break at the arm section of space suit with circumference *C* and overlapping section with width *W*

Characteristic impedance of the coax can be calculated [90] from

$$Z_0 \cong \frac{138}{\sqrt{\varepsilon_r}} \log_{10}\left(\frac{d_1}{d_2}\right) \tag{5.3}$$

where d_1 is the diameter of outer conductor, d_2 is the diameter of inner conductor, and ε_r is the relative permittivity of dielectric between conductors. Substituting 0.19 meter for d_1, 0.1 meter for d_2, and relative permittivity of air in Eq. (5.3) results in a characteristic impedance of 38.5 Ohms. The impedance looking from one section to the next section of the coax model can be approximated as $Z_l = 38.5 - jXc$, assuming no reflections within the following section. Values of Xc can be calculated using outer diameter dimension d_1 and overlap width (W). Substituting a value of 0.19 m for d_1 and 0.02 m for W in the equations for capacitance and reactance results in

$$Xc = \frac{1}{2\pi f C} \ . \tag{5.4}$$

where $C = \varepsilon_0 \varepsilon_r \left(\frac{A}{d}\right)$, ε_0 is the permittivity of air in free space, ε_r is the relative permittivity of the material, A is the area, and d is the distance between two surfaces. Reactance Xc is

approximately 40 at 400 MHz and proportionally less at higher frequencies. Therefore, the reflection coefficient is approximately 0.44, corresponding to approximately -7 dB of reflection coefficient. Resulting mismatch losses are small compared to basic losses of 28 dB per meter in lossy coaxial segments found in [15]. Experimental data taken from the space suit mockup with and without breaks in the shield layer confirms that the reflected wave was sufficiently small.

2) Effects of body joints

In addition to coupling effects, signal propagation behavior that creates impedance discontinuities at body joints (shoulder, elbow, etc.) is studied. This behavior results in a portion of the signal being reflected back to its origin rather than carried to the end of the transmission line. For example, for a shoulder joint in which the arm diameter is 10 cm and the space suit section diameter is 30 cm, characteristic impedance of 65.8 Ohm for Z_{arm} can be obtained by substituting values in Eq. (5.3). However, impedance from the torso side, Z_{torso}, with an approximate inner conductor diameter (astronaut chest) of 20 cm, is approximately 24.3 Ohms. Therefore, the reflection coefficient in this case is 0.46 and mismatch losses small compared to other losses, such as in the case of coupling sections.

3) Propagation in helmet, glove, and boots

The helmet in the EMU space suit uses a clear plastic bubble covered by the Extravehicular Visor Assembly, as shown in Figure 5.6 (left). This assembly has a thin layer of gold that protects the astronaut from harmful space waves [91]. For intra-suit propagation, the front face of the bubble may not be completely radio-opaque for signals in VHF and UHF bands due to the thin layer of gold used to achieve desired attenuation at optical wavelengths. However, based on simulation conducted with and without the helmet, similar path loss profiles are observed in both cases.

Figure 5.6 EMU space suit helmet (left) and EVA gloves (right) [91]

EVA gloves (Figure 5.6 (right)) and boots (Figure 5.7) are special cases in which portions may not be completely radio opaque. For example, the bottom of the boots may not include TMG layers or aluminized mylar layers. Therefore, similar to the helmet section, these portions of the suit could be modeled as partially open transmission lines.

Figure 5.7 EVA boots can be attached to the pant via rings [91]

The transmission line model incorporating basic series resistive losses of body tissue and capacitances of space suit couplings as well as additional losses incurred at body joints is depicted in Figure 5.8.

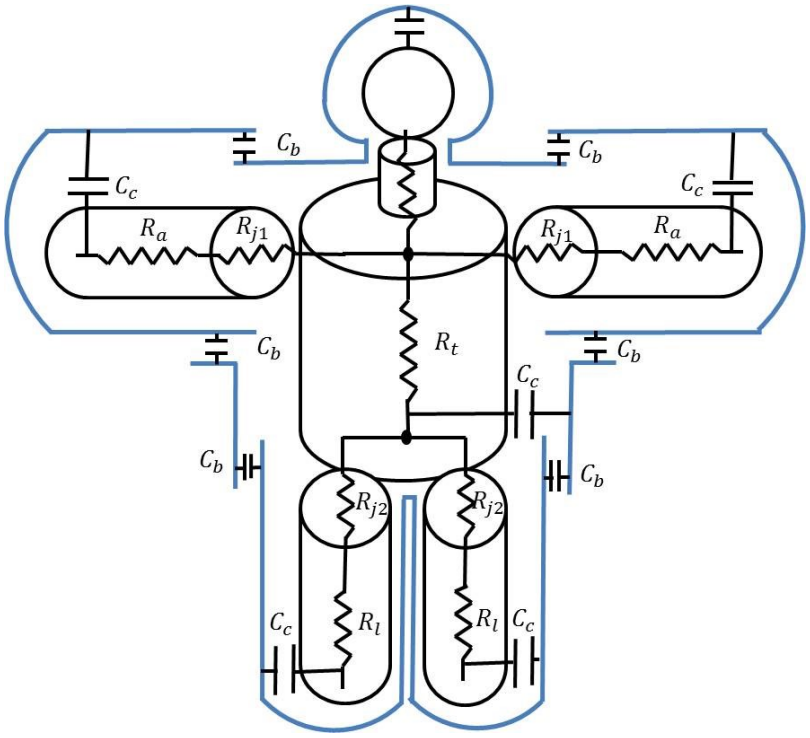

Figure 5.8 Transmission line model of the human body with space suit

Figure 5.8 is an abstract model designed only to illuminate primary factors that impact path loss in the intra-suit environment. In reality, the human body has a complex structure and geometry, requiring 3D electromagnetic simulation and experimental validation to obtain more effective and reliable quantification of resulting path loss. In the following, summary results of small- and full-scale models using these two techniques are provided.

5.3.3 Simulation and Experiments

5.3.3.1 Small-Scale Model

For this model, annular rings are replaced with an antenna/transducer that could efficiently launch a TEM wave. The top-hat monopole described earlier was chosen because it creates vertical polarization and is conformal to the human body.

The reflection coefficient magnitude is simulated in order to understand how well this antenna launches signals into the coax structure.

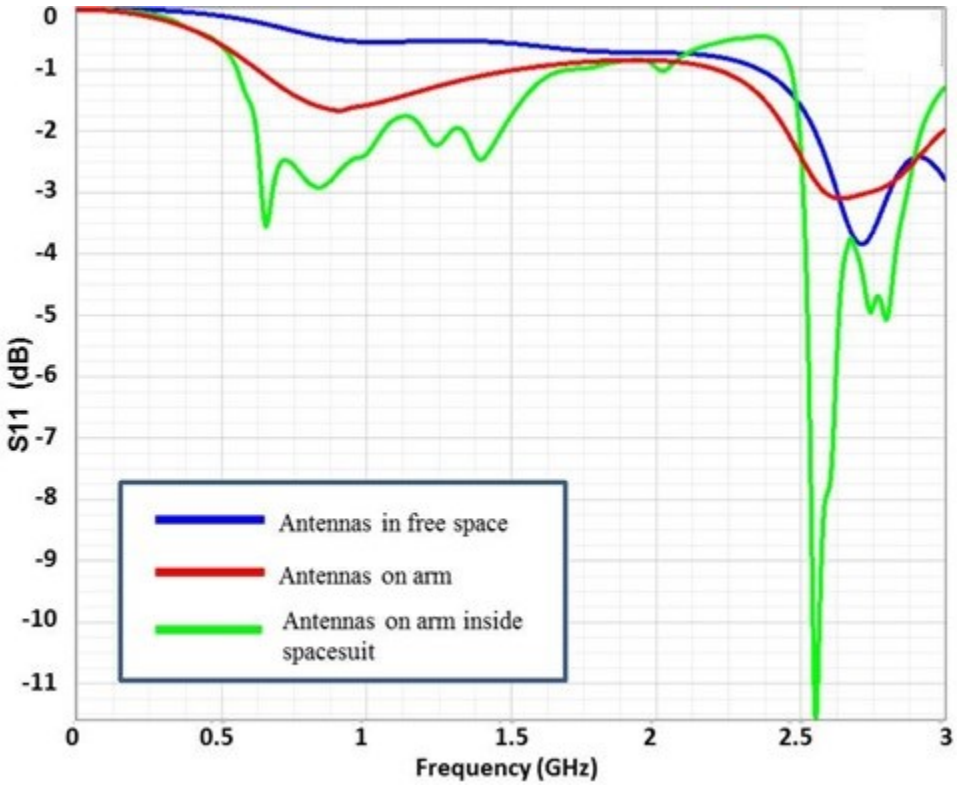

Figure 5.9 S11 for top-hat monopole on free space, on arm, and (3) on arm inside the space suit section

As shown in Figure 5.9, return loss (opposite sign of reflection coefficient (S11)) is low over a wide range of frequencies up to 2.45 GHz, especially when the antenna is used outside the suit. Inside the suit, however, return loss improves around 2.5 GHz due to coupling of one plate

of the antenna to the outer shield of the excited coax. Although the mismatch loss is high, techniques elaborated in [17] can help alleviate these factors.

As shown in Figure 5.10, forward transmission gain is simulated for two top-hat monopoles separated by 60 cm for three cases: (1) antennas in free space; (2) antennas mounted directly on arm model, and (3) antennas on arm but inside the aluminum hollow cylinder with 2 mm thickness. Loss in free space is significantly higher, especially at low frequencies, and decreases when antennas/transducers are mounted on the arm. Attenuation is also reduced when antennas are inside the cavity of the space suit, reaching values as low as 25 dB for the simulated 60 cm distance. Therefore, mismatch losses of the chosen antenna are not as excessive as expected. The guiding structure of space suit materials significantly enhanced propagation over the free space case.

As suggested in the S11 curve of the top-hat monopole, the S21 curve shows a peak around 2.8 GHz. The reduced mismatch loss implied by the S11 dip at this frequency partially offsets additional attenuation that is observed at high frequencies in previous studies. Therefore, for the small-scale arm model, all frequencies above approximately 400 MHz are well supported by the proposed antenna/suit system.

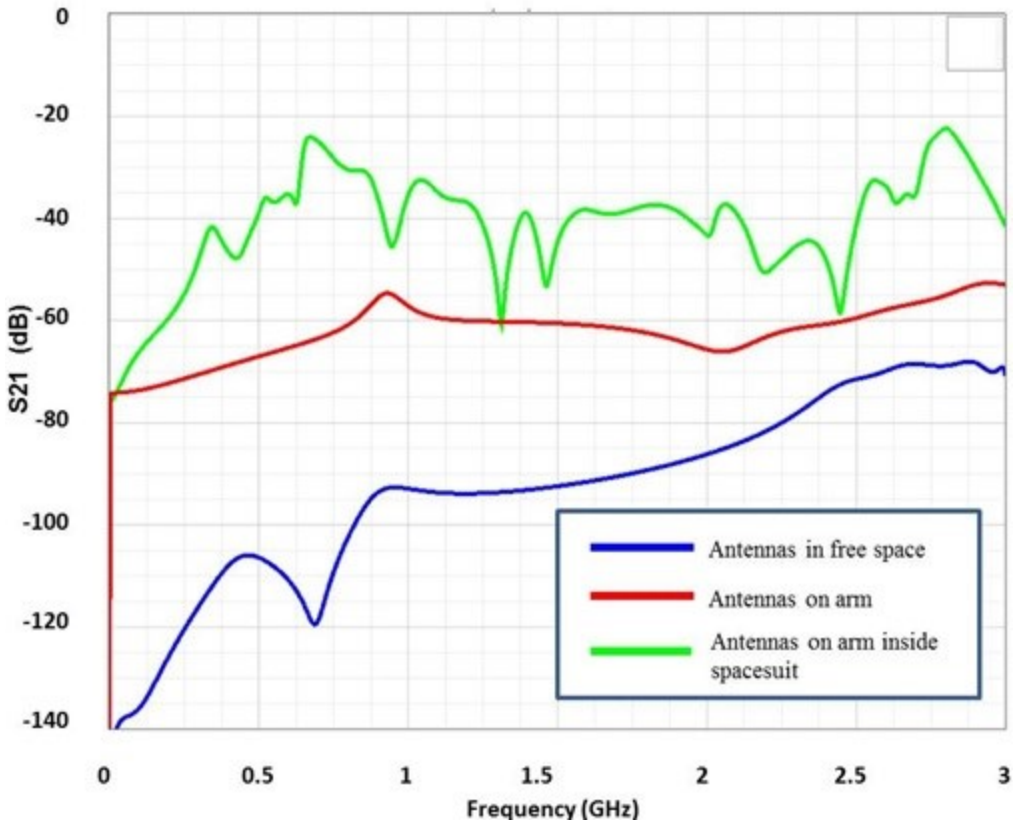

Figure 5.10 S21 for two top-hat monopoles separated by 60 cm on (1) free space, (2) on arm, and (3) on arm inside a space suit section

The EM simulator is also used to plot field distribution for intra-suit radio wave at 400 MHz to determine if the EM wave continues to follow the TEM mode. Resultant electric (E) and magnetic field (B) distributions are shown in Figure 5.11. Field direction is radial for E and annular for B as expected, leading to the conclusion that, using top-hat antennas, the created fields follows a TEM mode when operating below the multi-mode frequency.

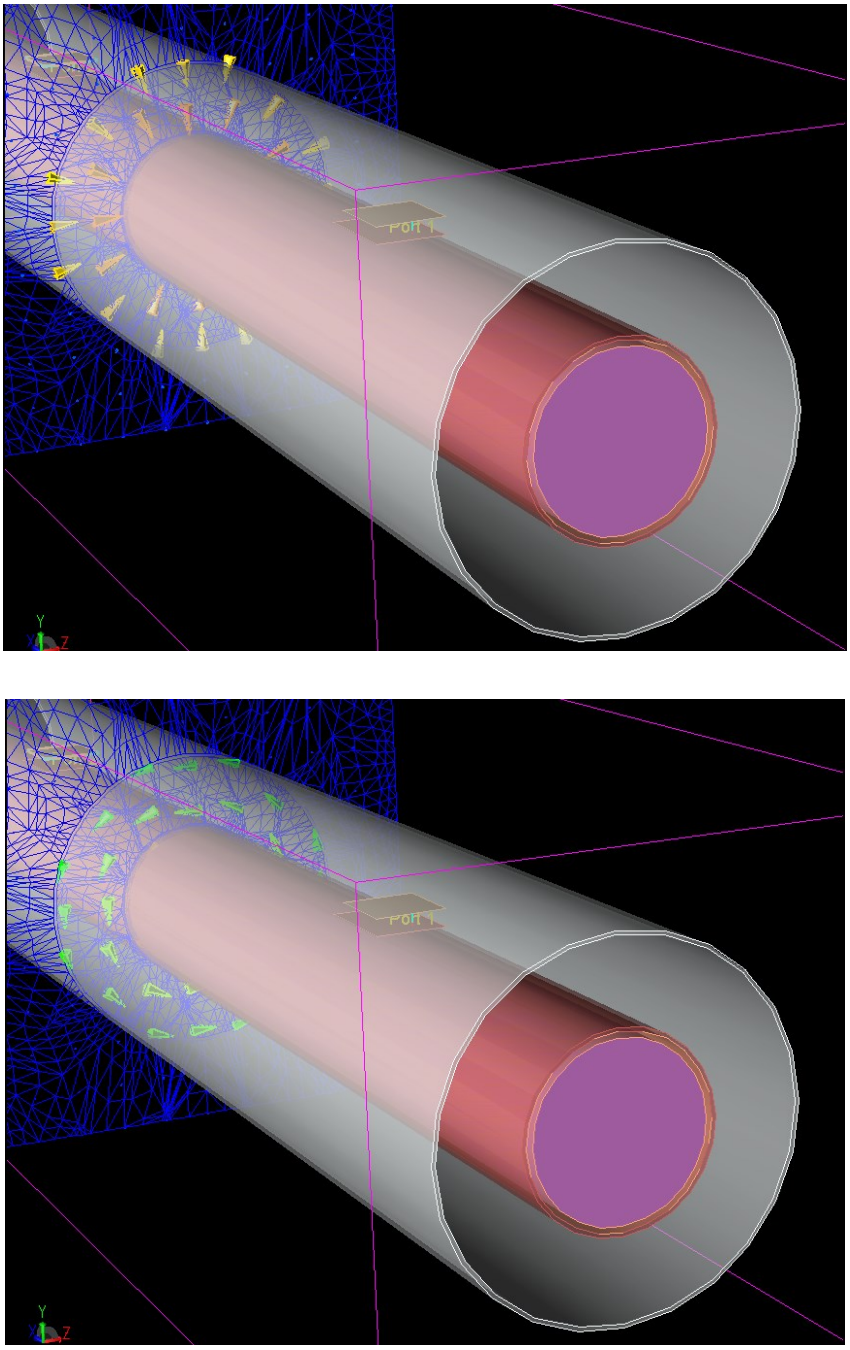

Figure 5.11 Electric (top) and magnetic (bottom) field distribution at distance slightly less than lamda/4 (34 cm) from the transmitter at 400 MHz

5.3.3.2 Full-Scale Space Suit Model

5.3.3.2.1 Received Signal Strength Assessment

While performing in-suit path loss measurements, it is a challenge to read the received signal level from a radio inside the suit. Using coaxial cables between the antenna and network analyzer is not a viable solution because coaxial cables' outer shields couple with and become part of the antenna structure, resulting in incorrect received signal strength readings on a network analyzer. Maintaining perpendicular configuration of coaxial cables inside the space suit is not guaranteed. Therefore, several alternatives are considered:

(1) Programming a microcontroller to convert the radio-board's Received Signal Strength Indicator (RSSI) output voltage to the equivalent power and display it on an LCD display. However, this alternative is not feasible as the space suit fabric will prevent the displayed data from being visible.

(2) Having a microcontroller store the data. The reading can be taken out after the experiment is finished.

(3) Converting the RSSI to an audio signal in which the frequency of the new signal can be mapped to a signal power. This option is adopted because of its ability to provide valuable real-time feedback [17].

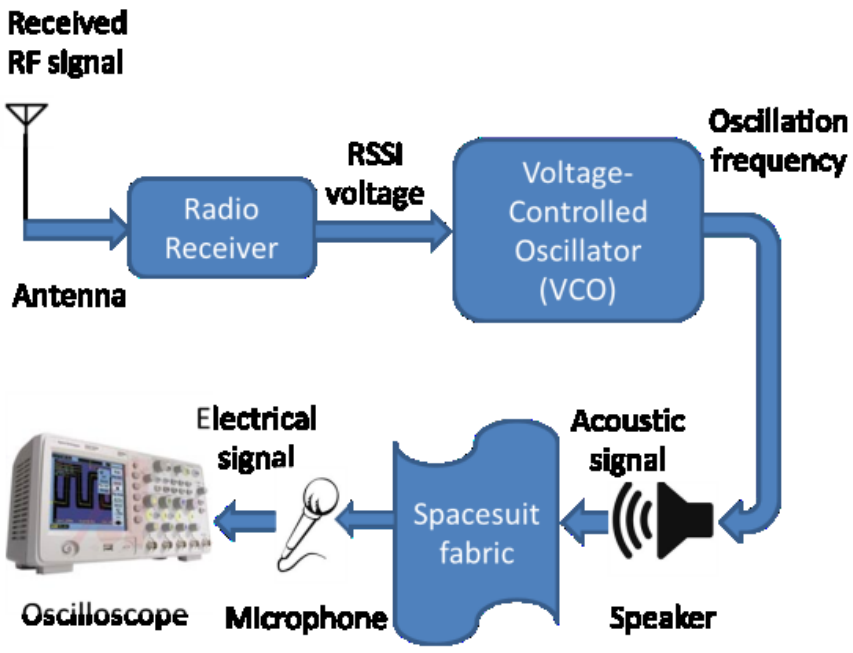

Figure 5.12 Block diagram showing how received RF signal is converted to an audio signal

As shown in Figure 5.12, an audio voltage-controlled oscillator (VCO) is connected to the radio's received signal strength indicator (RSSI) so that the output audio tone frequency changes according to RSSI level. Then, the audio signal is transmitted outside the space suit via a small speaker. Care is taken to keep the wires short and close to the receiver ground plane to avoid interaction with antenna/transducer function.

Before performing RF path loss measurements, a mapping table of RF signal strength to audio tone frequency is performed for each radio. During measurements, audio signal frequency was observed on an oscilloscope with Fast Fourier Transform (FFT) mode, as demonstrated in Figure 5.12 and the audio tone is mapped back to RF signal strength with a resolution of approximately 2 dB.

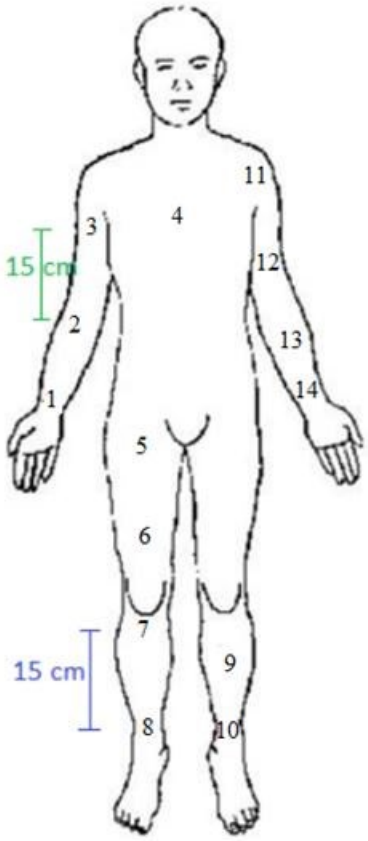

Figure 5.13 Radio locations for intra-suit wireless propagation

Table 5.3 Radio location reference

Radio Location	
TX	RX
right leg (8)	left leg (10)
left wrist (14)	right wrist (1)
left wrist (14)	left ankle (10)
ankle (8)	leg measurements (5)
ankle (8)	leg measurements (6)
ankle (8)	leg measurements (7)
shoulder (11)	chest (4)
mid upper arm (12)	chest (4)
mid lower arm (13)	chest (4)
mid calf (9)	chest (4)
right wrist (1)	chest (4)

5.3.3.2.2 Measurement Setup

The components described above are depicted in Figures 5.14 and 5.15 with space suit conductive fabric, microphone, and oscilloscope.

Figure 5.14 Transmitter and receiver placement

In order to conduct path loss measurements, the radios are initially placed on the body with zero antenna-body separation (one plate touching the body) at recommended locations as shown in Figure 5.13. Figure 5.14 demonstrates how bubble wrap is utilized to create a gap between the body and outer layers of the suit in order to model the air gap created by inflation of a real suit.

Figure 5.15 Measurement setup for full-scale mockup space suit

5.3.3.2.3 Kansas State University Space Suit Path Loss Results

Figure 5.16 demonstrates the full-scale measurement setup.

Figure 5.16 Taking path loss measurements for various intra-suit links

Path loss measurements are first calibrated to remove additional loss incurred by the presence of circuit and antenna-mismatch losses. Table 5.4 presents extracted path loss values for the full-suit case after removing additional loss.

Table 5.4 Median path loss measurement results for various frequency bands [18]

Tx Location	Rx Location	315 MHz	433 MHz	916 MHz	2.4 GHz
right ankle (8)	left ankle (10)	41.3	48.6	67.5	47.4
left wrist (14)	right wrist (1)	64.3	52.6	63	50.3
left wrist (14)	left ankle (10)	87.3	64.6	70	50.3
ankle (8)	leg measurements (5)	26.3	22.6	37	26.8
ankle (8)	leg measurements (6)	25.3	18.6	30	14.8
ankle (8)	leg measurements (7)	25.3	15.6	25	15
shoulder (11)	chest (4)	27.3	16.6	44	23.8
mid upper arm (12)	chest (4)	37.3	28.6	49	31.8
mid lower arm (13)	chest (4)	40.3	29.6	57	40.8
mid calf (9)	chest (4)	47.3	40.6	56	23.8
right wrist (1)	chest (4)	44.3	35.6	60.5	43.9

A person 173 cm tall and weighing 77 kilograms, is utilized for the measurements. These RSSI readings were taken multiple times in order to minimize reading variation; the median path loss is recorded. Measurements generally varied by approximately 5dB depending on body geometry of the person utilized in the experiments and his/her height and weight. However, the same experiment conducted on the same person resulted in slightly varying measurements for several reasons: (1) The transmit and receive antenna were not aligned in co-pole polarization, (2) Air cavity distance changed between the copper fabric representing the TMG layer of space suit (outer coaxial conductor) and the skin of the body (inner coaxial structure).

Lower path loss values are mostly observed for 2.4 GHz radio channel than for 916 MHz radio channel. We believe that because of using the top-hat monopole antenna with reflection coefficient characterized in Figure 5.9 that shows resonance at 2.5 GHz. This might give an

interpretation of why the top-hat monopole is radiating efficiently at 2.4 GHz which results in much path loss than expected. Using other types of antennas may better decouple the antenna effects from radio channels observed in the experiments.

Highest path loss values are observed for left wrist-to-left ankle link (87.3 dB for 315 MHz, 64.6 dB for 433 MHz, 70 dB for 916 MHz, and 50.3 dB for 2.4 GHz radio channel). The worst signal attenuation for wrist-to-ankle link, shown in Table 5.4, is due to the relatively long propagation distance compared to other on-body links. This link, depicted in Figure 5.13, proves that the signal transitions between various body parts (e.g., arm-to-torso, torso-to-leg). These body parts have different impedances due to varying dielectric properties of tissues within each part and tissue thicknesses, thereby causing additional loss in wireless signal strength. Moreover, the torso represents an N-port junction leading to substantial loss for paths involving transition through this region (i.e., mismatch losses at shoulder and leg joints) expectedly occurred. However, losses for paths proceeding from an arm or leg into the torso but do not leave were relatively low. For this situation, mid-UHF range of 433 MHz is generally favored, although all path loss values are low compared to typical off-body WBAN links.

5.4 Safety Study of Radio Transmitters on Astronaut Body[8]

This Section briefly describes the safety of low-power transmitters related to astronaut health. The FCC recommends investigation of the SAR, or most commonly used metric, in order to estimate the RF exposure level [92]. Therefore, SAR limits should be evaluated for sections of

[8] *Copyright 2014 IEEE*. Portions of Section 5.4 are reprinted with permission from Taj-Eldin, M.; Kuhn, W.B.; Fowles, A.H.; Natarajan, B.; Peterson, G.; Alshetaiwi, M.; Shuo Ouyang; Sanchez, G.; Monfort-Nelson, E., "Study of Wireless Propagation for Body Area Networks Inside Space Suits," *Sensors Journal, IEEE* , vol.14, no.11, pp.3810,3818, Nov. 2014

human body composed of skin, fat, and muscle tissues with 1 mm, 3 mm, and 40 mm thickness, respectively, as shown in Figure 5.17.

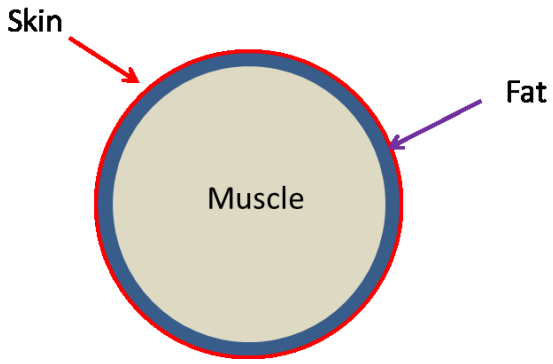

Figure 5.17 Human body model

The most commonly used SAR safety limits, defined by the IEEE [92], correspond to 1.6 mW/g for 1 g of tissue. These guidelines are adjusted for maximum mass-normalized rates of EM energy deposition for any 1 g or 10 g of tissue [93].

The top-hat monopole antenna described in Section 5.1 is placed directly on the arm body model shown in Figure 5.17. A total of 1 mW of input power is applied at the antenna port. An EMPro FDTD-based solver is used to estimate values of averaged 1 g SAR value. Maximum SAR values are recorded across all cell grids for frequencies of interest and presented in Table 5.5.

Table 5.5 Maximum specific absorption rate values using 1- g SAR sensor

Frequency	315 MHz	433 MHz	916 MHz	2.4 GHz
1 g SAR (mW/g)	0.0017	0.0023	0.0073	0.00077

As evident from Table 5.5, the maximum resulting SAR for 1 g of tissue is always well below the safety limit (1.6 mW/g) for all frequencies of interest This suggests that a radio with

higher power than 1 mW is reasonably safe as SAR for 1 g of tissue will of course be below the 1.6 mW limit at the 1 mW level.

5.5 Chapter Summary

This chapter included discussion of the performance of an intra-space suit radio channel. Similar to previous chapters, path loss was used as the main performance metric.

Study results revealed the following:

(1) Despite significant loss due to series resistance of body tissue, path loss is sufficiently low, demonstrating that the unique propagation environment formed by the cavity of space suit is quite conducive to wireless signal propagation.

(2) Radio signals suffer additional attenuation at body joints due to impedance change, but the additional loss is not excessive.

(3) Use of low-power 1 mW transmitters and wireless links in the VHF and UHF bands yield path loss values generally below 90 dB so that most commercial receivers can still capture the resultant received signal.

(4) Minimization of overall path loss is a complex tradeoff between optimizing frequency for the coaxial transmission-line medium and complications related to launching and receiving fields using a suitably sized “antenna” or transducer.

During characterization of the intra-space suit channel, we have seen that the choice of antenna is found to significantly impact determination of radio channel performance and frequency. Therefore, the following chapter investigates various antenna designs, particularly in the MedRadio band where the radio channel is most conductive. From a commercial perspective, this emerging band also has potential future applications due to the heavily crowded ISM band

(2.4 GHz, 915 MHz, etc.) and its adjacent medical body area networks band (i.e., 2360 to 2390 MHz and 2390 to 2400 MHz).

Chapter 6 -Wearable Textile Antennas for Body Area Networks

The previous chapters presented a comprehensive study for intra-space suit environment for small and full-scale space suit models. In the study presented up to now, we assumed that the space suit is fully or largely radio-opaque. However, through experiments conducted on EMU space suit materials, it has been found that radio opacity decreases with the age of the aluminized Mylar. Moreover, alternative suits being studied by NASA and others for possible future use may omit aluminized Mylar in the outer TMG layers [94]. This makes the development of wearable flexible antennas in general, potentially applicable to the intra-space suit environment as well. Thus, in this chapter, we evaluate the performance of several general-purpose wearable flexible antennas operating at the MedRadio band. We believe that developing antennas in this relatively newly licensed band is important and to the best our knowledge, there is a lack in research in this frequency range.

In section 6.1, we divide the problem of developing antennas for body-centric communications based on the wavelength or frequency used. The antennas are put into three categories: (1) antennas at low frequencies (<100 MHz), (2) antennas at frequencies falling in the transition region (200- 500 MHz), and (3) antennas at frequencies above 500 MHz, based on how wavelength compares with human body dimension.

After that, we conduct a comparative study for several proposed antennas operating in the MedRadio Band, which falls in the transition region band (200-500 MHz). We utilize our findings of antenna performances when they are worn to develop our own novel antenna where its performance overcomes the drawbacks found.

6.1 Antennas for Wireless Body Area Networks

Antennas play a key role in optimizing a radio system's performance as they are used to transmit/receive signals through free space, for example, as electromagnetic waves. In the literature, wearable antennas have been mostly designed to operate in GSM/PCS band [95], the unlicensed ISM band (2.4 GHz) [96], [97], licensed Medical Body Area Network Band (2.34-2.4 GHz) [98], and UWB (3.1 GHz – 10.6 GHz) [99], [100], [101], [102], [103], dual and multi band [40], [104], [105], [106], [107], [108], [109], [110], and more recently in the MedRadio band (4xx MHz) mostly for medical applications [111], [112], [113], [114], [115] . Commercial requirements for body-centric communication are that the radio system elements be small, conformal to human body and light in weight so that these elements can be integrated in individual's daily clothes. Moreover, for on-body antennas, they should ideally be immune to the effects of human body in order to get the optimal performance.

Miniaturizing antennas presents several design challenges especially in the lower bands such 400 MHz, since the performance of the antenna is related to the antenna size compared to wavelength. Therefore, design trade-offs between antenna characteristics will be present such as antenna efficiency, impedance bandwidth and radiation characteristics. In addition, in order to design good body-mounted antennas, understanding the effects of human body on the behavior of the antenna is essential prior to designing an antenna with good radiation characteristics.

Possible effects may include frequency detuning, changes in radiation pattern and antenna input impedance as well as variation in the bandwidth and realized gain and reduction in radiation efficiency. Those effects vary between different antennas, ground plane presence and size, antenna-body separation distances and near-field proximity coupling [43].

In the following section, antennas used for body-centric communications are classified according to the wavelength used relative to body size.

6.2 Classification of Antennas for Body-Centric Communication

In Chapter 2, Figure 2.1 and Figure 2.2 illustrated the relative permittivity and conductivity for various body tissues in the range of 10 KHz to 10 GHz. However, the important parameters of loss tangent and penetration depth were not. Thus, the real part of Eq. (2.2), Eq. (2.10), Eq. (2.7) are used to plot the real part of complex relative permittivity, loss tangent, and penetration depth, respectively in Figure 6.1 from 100 MHz to 10 GHz.

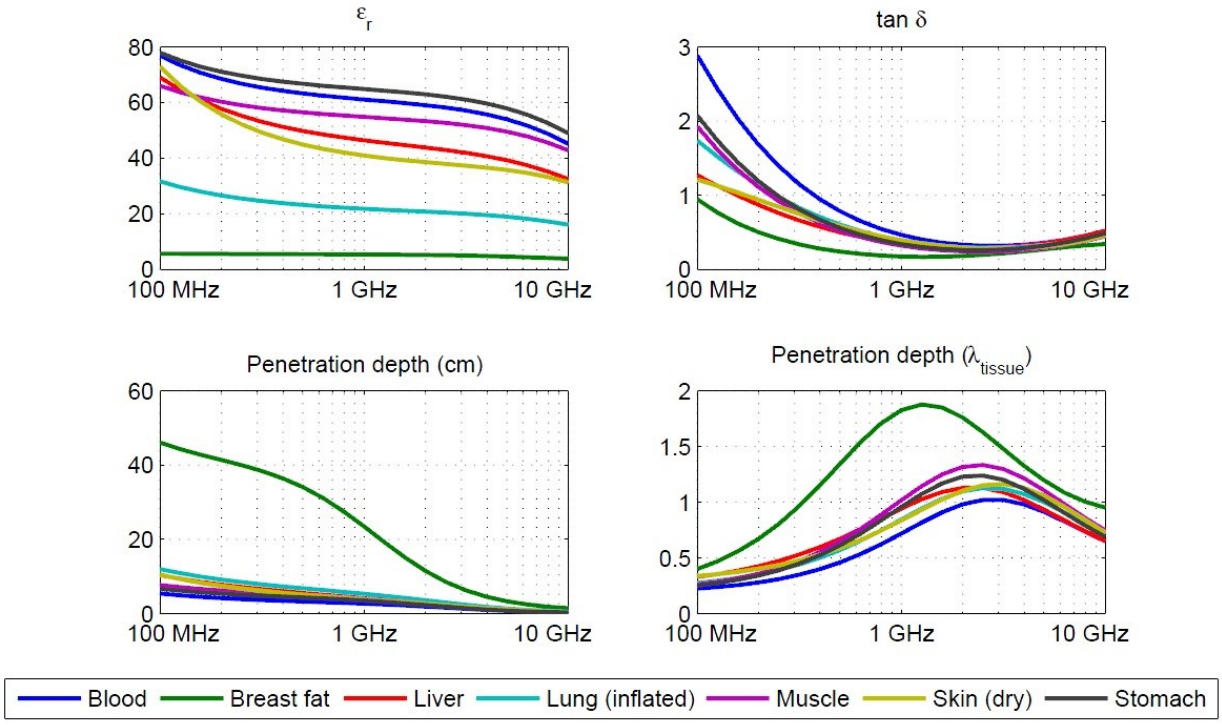

Figure 6.1 Tissue properties versus frequency, reproduced from [22]

For study purposes, the wearable antenna design problem is divided according to the wavelength (frequency) used; (1) antennas operating at frequencies lower than 100 MHz, (2)

antennas operating at frequencies that fall in the range of 200 to 500 MHz, and (3) antennas operating at frequencies above 500 MHz.

The free-space wavelength at 100 MHz is 3 m. Thus the size of the human body is comparable to this wavelength and significant interactions can be expected. It is known that the penetration depth is different for each body tissue and also the thickness varies from one body part to another. For example, the penetration depth for skin is 10 cm, and 8 cm in muscle, and 18 cm in bone. Therefore, the skin is very thin compared to wavelength and even muscle in arms and legs. However, the muscle penetration depth is comparable to wavelength at the torso section that can partially block radiation.

The transition region (200 MHz to 500 MHz) has additional issues where both the body posture and antenna-body distance play a significant role in determining the performance of on-body antennas [116]. Above the transition region, the antenna is less affected by position on the body, the size of the body, or the body posture. However, the antenna-body separation distance relative to wavelength may still play a large role on changing the antenna impedance [116].

In this study, we will focus on antennas operating in the transition region, specifically on the MedRadio band and several antenna types will be investigated.

6.3 Wearable Textile Antennas at MedRadio Band[9]

In the following pages, the designs of MedRadio antennas are presented for five geometries; monopole, patch antenna, planar inverted F (FIPA), small loop, and bow-tie antenna.

[9] Portions of Section 6.3 are reprinted with permission from M. Taj-Eldin, W. Kuhn, and B. Natarajan, "Wearable Textile Antennas: A Comparison of Antenna Performance Parameters versus Wear ability Issues at MedRadio Band", *under preparation*.

6.3.1 Monopole Antenna

A fabric-based monopole antenna with partial ground plane and feed line with length L_G is presented in Figure 6.2. The length of monopole is L_M, has width W_M and is mounted on the top of felt fabric as the substrate with thickness of 1.62 mm with relative permittivity of 1.22. This simple design derives its geometry from [117]. The monopole is made of the same material as the feed line; copper platted fabric of thickness 0.035 mm. Antenna parameters are summarized in Table 6.1. The effective wavelength in this case (using Felt Substrate) is nearly the same as the wavelength in free space (i.e.,$\varepsilon_r = 1$). So, the wavelength at center frequency of 433 MHz equals approximately 700 mm.

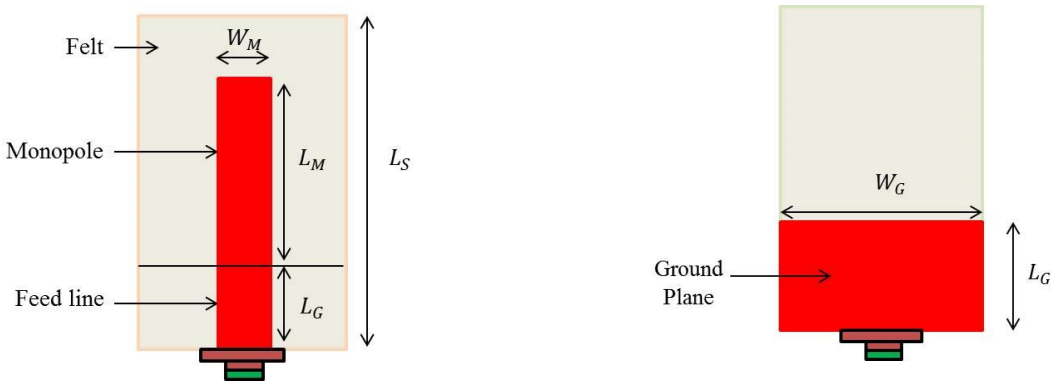

Figure 6.2 Microstrip Monopole Antenna, top view (left), and bottom view (right) [117]

Table 6.1 Dimensions of monopole antenna

Parameter	Dimension in mm
W_M	8.5
L_M	173
W_G	40
L_G	113
L_S	286
Relative Permittivity of Substrate	Felt (1.22)
Substrate Thickness	2

The design is then built in 3D electromagnetic simulator and illustrated in Figure 6.3.

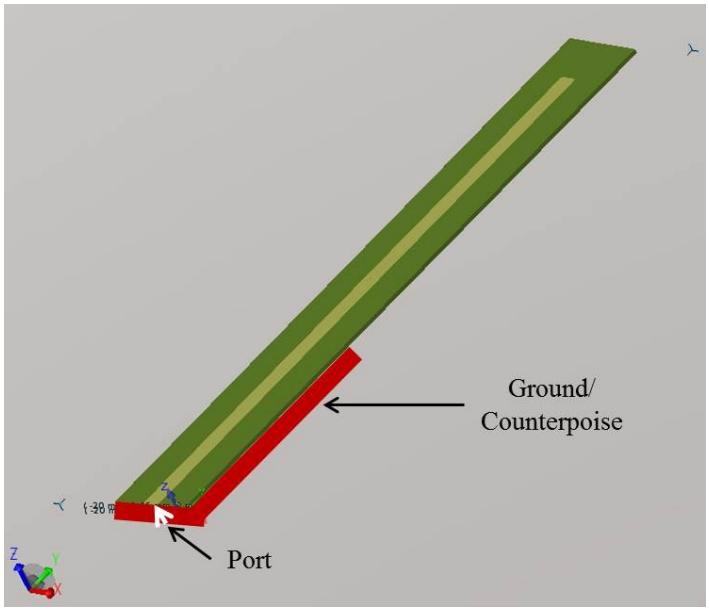

Figure 6.3 Simulated microstrip monopole antenna using EMPro

6.3.2 Microstrip Patch Antenna

A 433 MHz microstrip antenna is designed using the typical equations [37]. The dimensions of the patch antenna are summarized in Table 6.2.

Table 6.2 Dimensions for microstrip patch antennas

Parameter	Dimension in mm
W	329
L	311
W_G	341
L_G	323
Relative Permittivity of Substrate	Felt Fabric (1.22)
Substrate Thickness (h)	2

This design is then drawn in 3D simulator and a top-view of this antenna is shown in Figure 6.4.

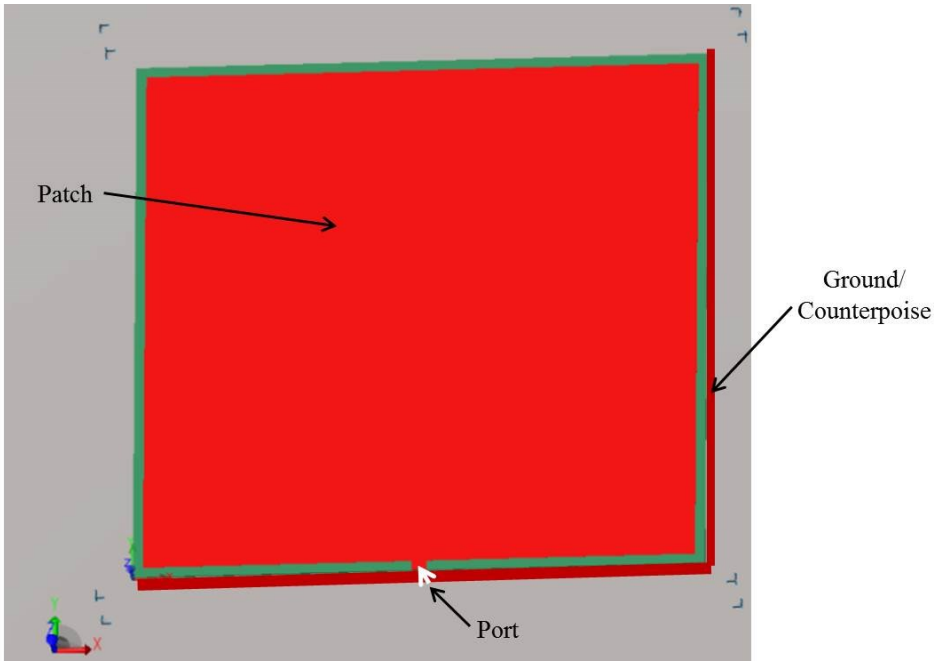

Figure 6.4 Microstrip Patch Antenna on the top of felt fabric antenna

6.3.3 Planar Inverted F Antenna

Next, a MedRadio planar inverted F antenna (PIFA) is designed where the antenna geometry [118] and simulated structure in 3D EM simulator are illustrated in Figure 6.5.

Also, the dimensions of this antenna are specified in Table 6.3 and are derived using empirical formulas used in [118].

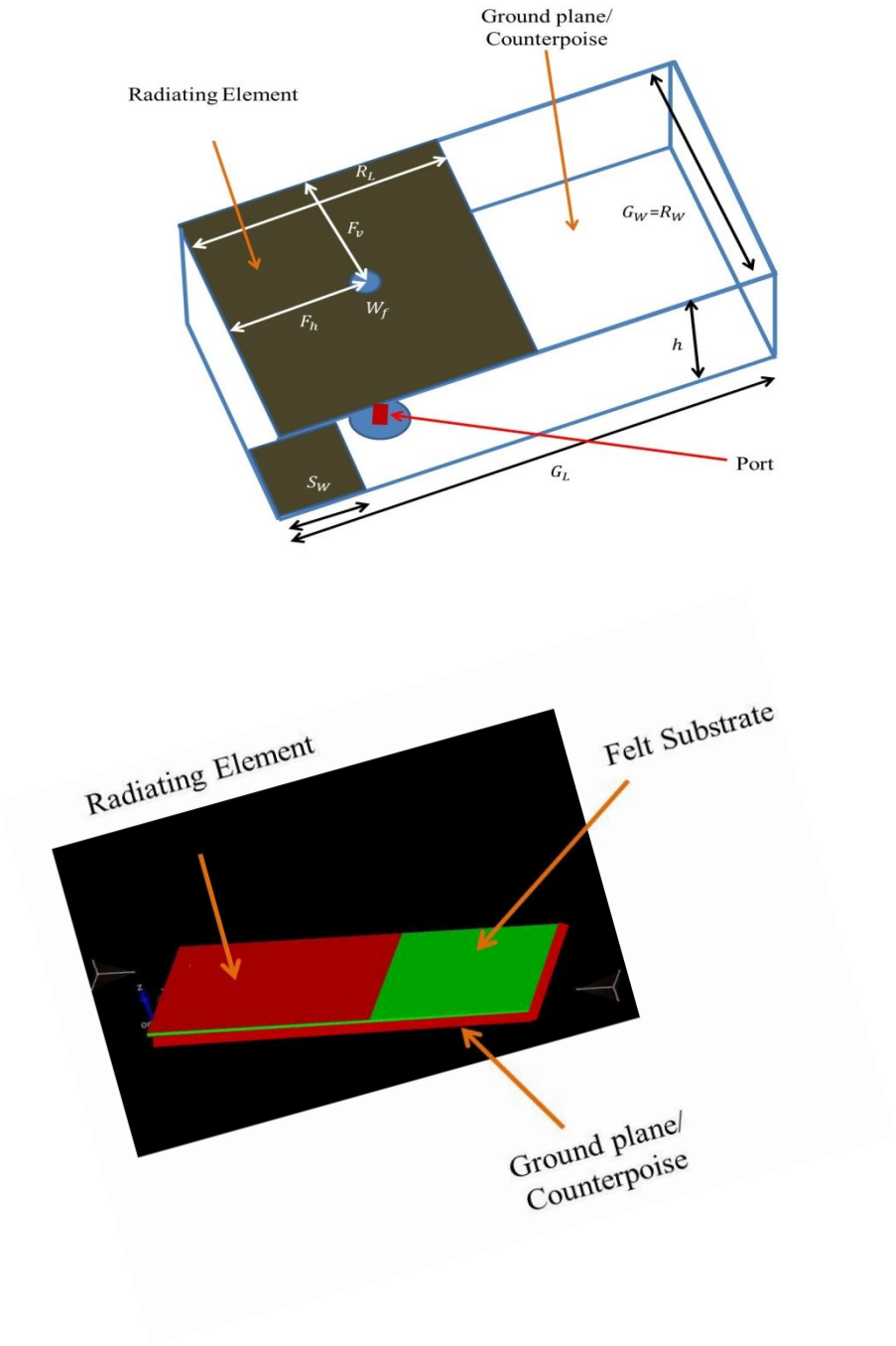

Figure 6.5 Planar inverted F antenna on the top of felt fabric antenna, antenna geometry [95] (top), and simulated antenna in EMPro (bottom)

Table 6.3 Dimensions for planar inverted F antenna

Parameter	Calculated Value (mm)
G_L	125
G_W	74
$R_L = L_1$	90
$R_W = W$	74
F_{h}	5
F_v	5
S_W	1
h	1.6
Fleece substrate material	1.26

6.3.4 Small Loop Antenna

The fourth type of antenna designed is small loop antenna which has a radius of 25 mm with conductor radius of 0.5 mm. It should be noted that this antenna is not tuned to a center frequency of 433 MHz as in the previous antennas. Such tuning would be done in practice using tuning capacitor. The purpose of the evaluation process is to calculate the radiation efficiency and other antenna parameters which are not affected by mismatching when evaluating with a simulator. Later, this antenna can be matched to the source impedance, 50 Ohm, for example, and enhance the reflection coefficient in a physical experiment.

The small loop antenna is drawn in Figure 6.6 where the feeding port is on the right and distance between two end points of port is 1 mm.

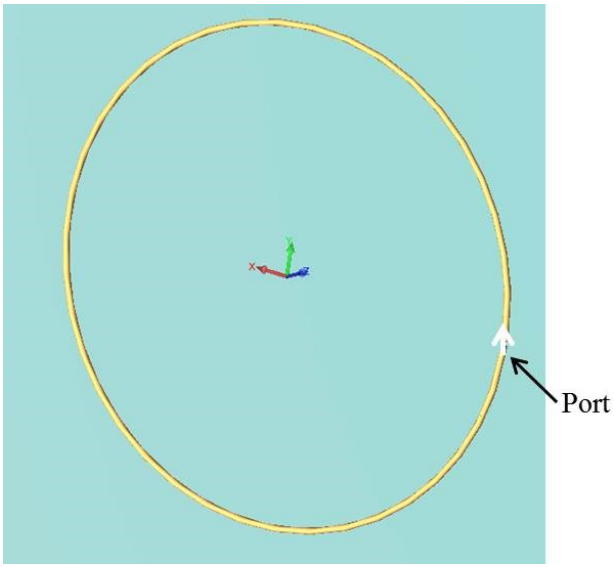

Figure 6.6 Small loop antenna with radius of 25 mm and conductor radius of 0.5 mm

6.3.5 Bow-Tie Antennas

Next, a bow-tie antenna is designed first in its conventional form. Then, a modified version called folded bow-tie antenna is presented. The folded bow-tie is presented in [119] and some improvements to widen the antenna bandwidth are proposed in [120] by adding some elements. Finally, we propose a different design that overcomes the drawbacks of the first two bow-tie antennas.

6.3.5.1 Conventional Bow-Tie Antenna

A conventional bow-tie antenna is developed to operate at a center frequency of 433 MHz. The geometry of this antenna is shown in Figure 6.7 where two triangular segments that are touching the port endpoints at each triangle tip. This fabric-based bow-tie antenna is placed on a thin layer of felt substrate with relative permittivity of 1.22 and thickness of 0.035 mm which prevents the conducting elements from touching the body.

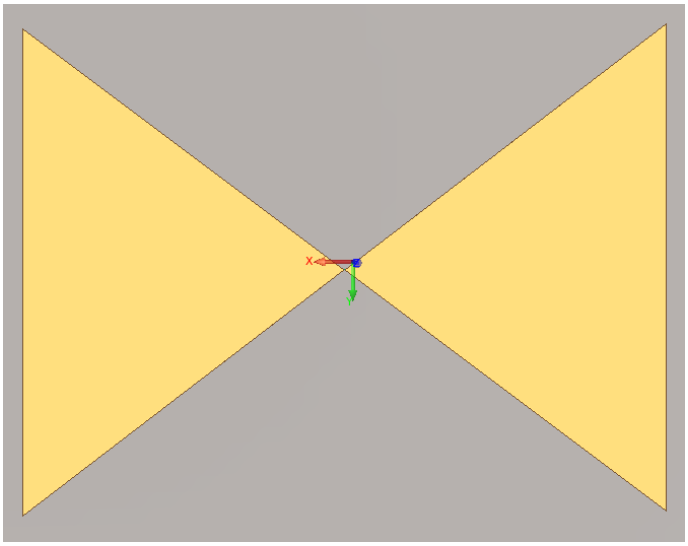

Figure 6.7 Conventional Bow-Tie Antenna

6.3.5.2 Folded Bow-Tie Antenna

Next, a modified version of bow-tie antenna is simulated where two microstrip lines are connecting the two triangles at each end. This geometry is derived from [119] and presented in Figure 6.8. The purpose for this modification was to widen the bandwidth of the bow-tie.

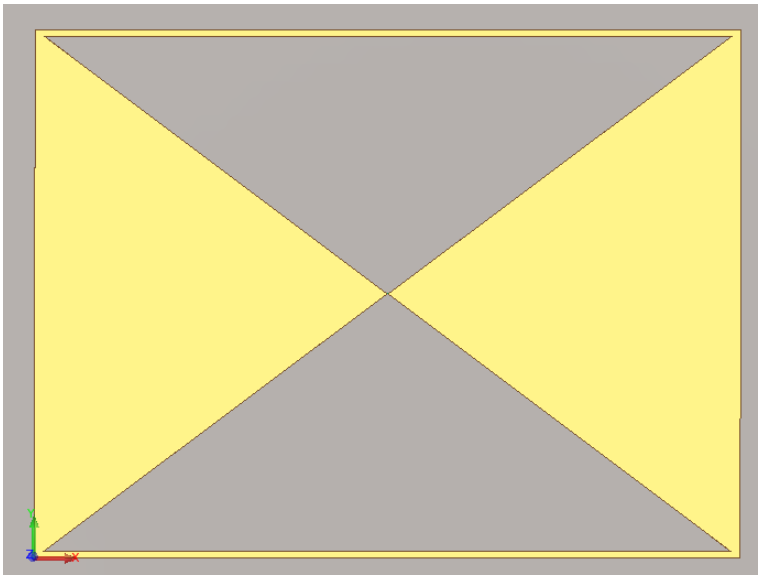

Figure 6.8 Folded Bow-Tie Antenna

6.3.5.2.1 Current Magnitude and Distribution

For folded bow-tie antenna, the current magnitude and distribution are visualized for comparison purpose with the proposed antenna in the subsection 6.3.5.4. After adjusting the settings of FEM solver according to those in 6.3.5.1 Simulation Setup with one volt applied voltage to a 200 Ohm source, the simulation is run. After delta error is reached to a value less than 0.01 for two consecutive passes of delta error, the current distribution is plotted in Figure 6.9.

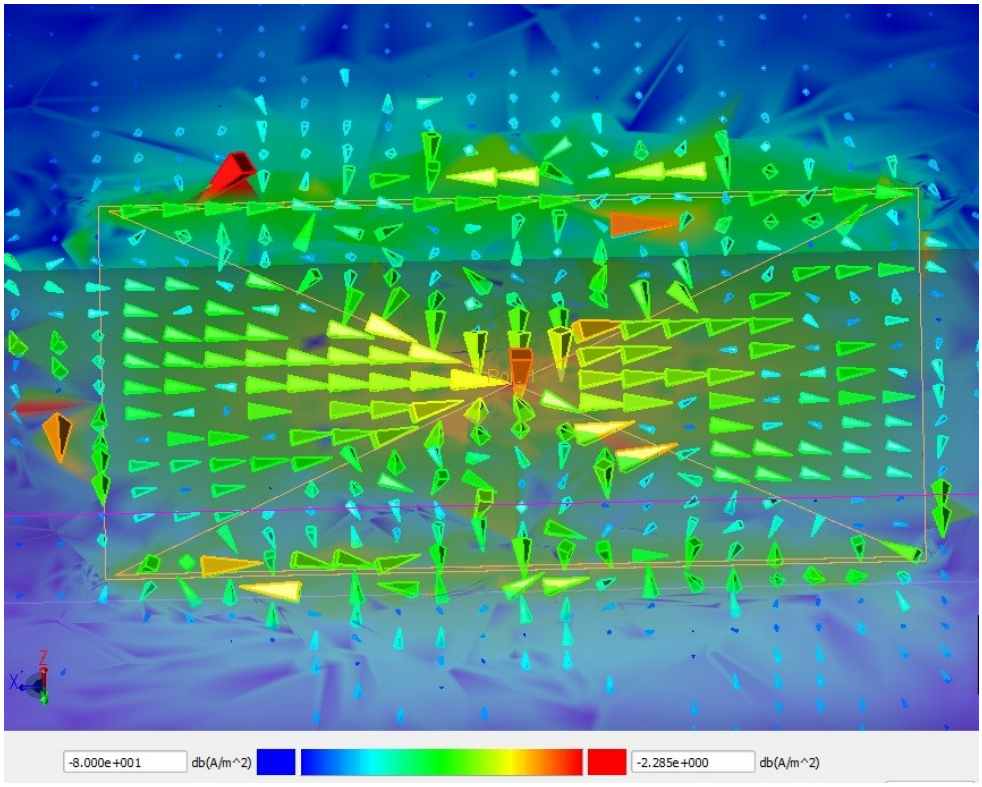

Figure 6.9 Logarithmic scale of current magnitude and distribution for folded bow-tie antenna at 433 MHz for on-body scenario with 5 mm antenna-body separation

6.3.5.3 Self-shielded Folded Bow-Tie Antenna

Finally, we present our proposed antenna that we call it "self-shielded folded bow-tie antenna". This antenna is basically a two-layer antenna as can be seen in Figure 6.11 (side view) where the two ends of two triangles on the bottom layer are shorted by a thin microstrip line. However, the top two triangles forming the bow-tie are not shorted the center but the two layer are shorted at the ends (left and right) by two microstrip lines of height 1.62 mm corresponding to the separation distance between the two layers.

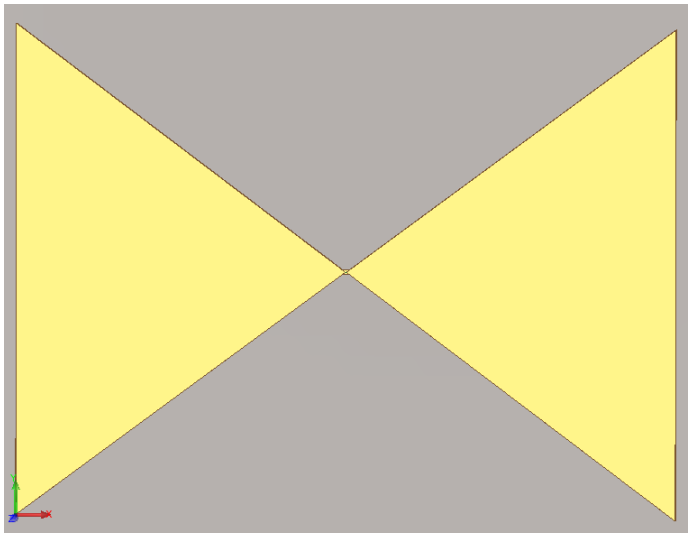

Figure 6.10 Self-Shielded Folded Bow-tie Antenna (Top view)

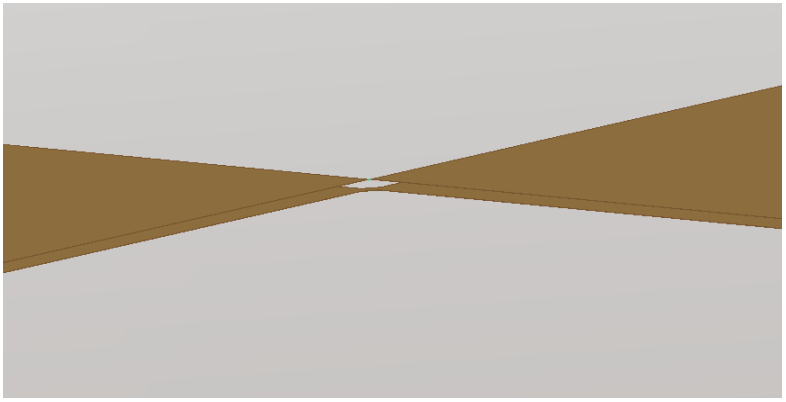

Figure 6.11 Self-Shielded Folded Bow-tie Antenna (side view)

6.3.5.3.1 Current Magnitude and Distribution

After adjusting the settings of FEM solver according to those in 6.3.5.1 Simulation Setup with one volt applied voltage to a 200 Ohm source, the simulation is run. After delta error is reached to a value less than 0.01 for two consecutive passes of delta error, the current distribution is plotted in Figure 6.12.

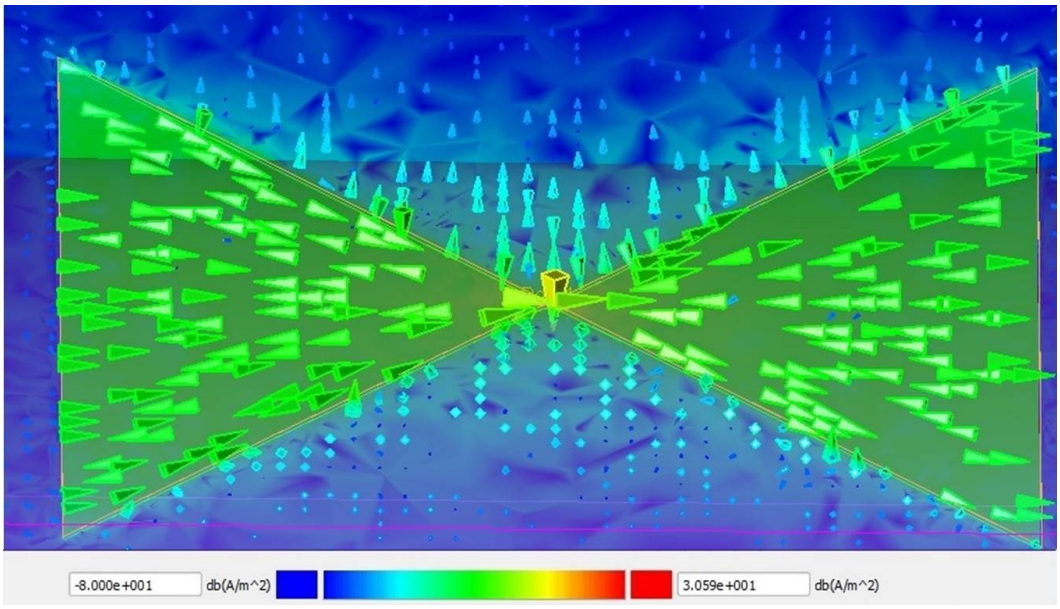

Figure 6.12 Logarithmic scale of current magnitude and distribution for proposed self-shielded folded bow-tie antenna at 433 MHz

We hypothesize that the electric and magnetic field distribution for self-shielded folded bow-tie antenna together with its geometry are depicted in Figure 6.13.

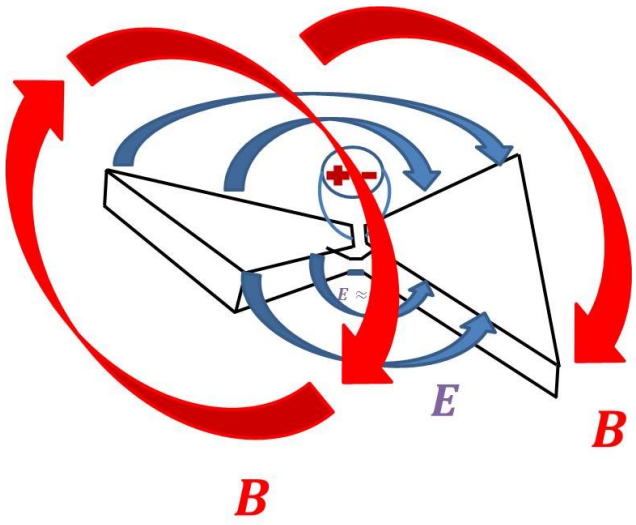

Figure 6.13 The geometry of Self-Shielded Folded Bow-Tie with its anticipated electric and magnetic field directions

To verify our hypothesis, electric and magnetic field directions can be plotted as planned in Future work of Chapter 7. The three antennas are drawn in Figure 6.14 for comparison purpose. These antennas have the same dimensions in terms of length and width but differ in shorting methods.

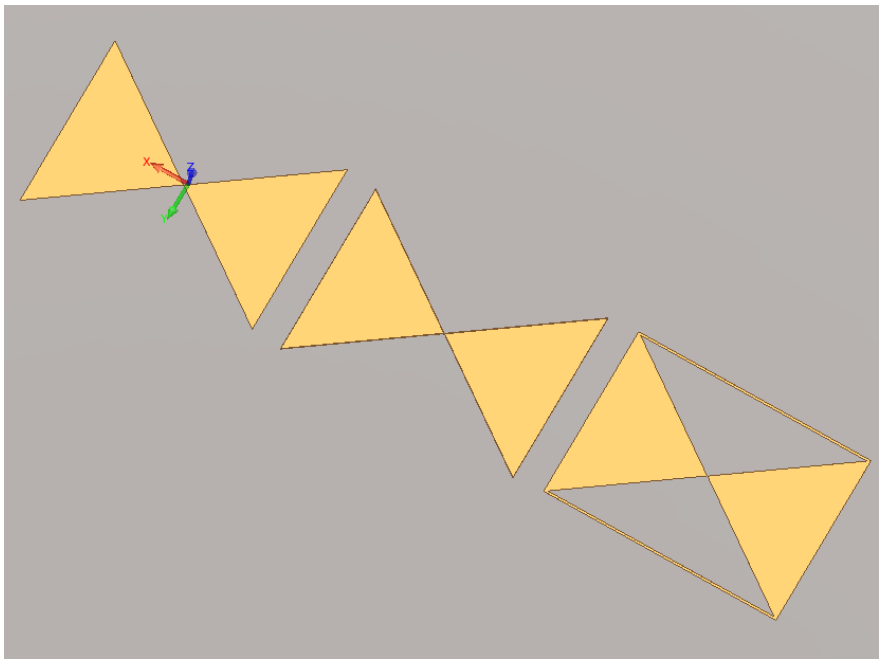

Figure 6.14 Dimensions: 32.05*24 cm, 32.05*24 cm with 1.62 mm gap, 32.05* 24 cm

6.4 Simulation Study of Antenna Performance in Free Space and on-Body

In the following, the performance of several antennas is simulated in two scenarios: free space and on-body case with 5 mm antenna body separation. For all antennas, the human body model used is an elliptical torso model made of muscle (Figure 6.15) except for the case of loop antennas.

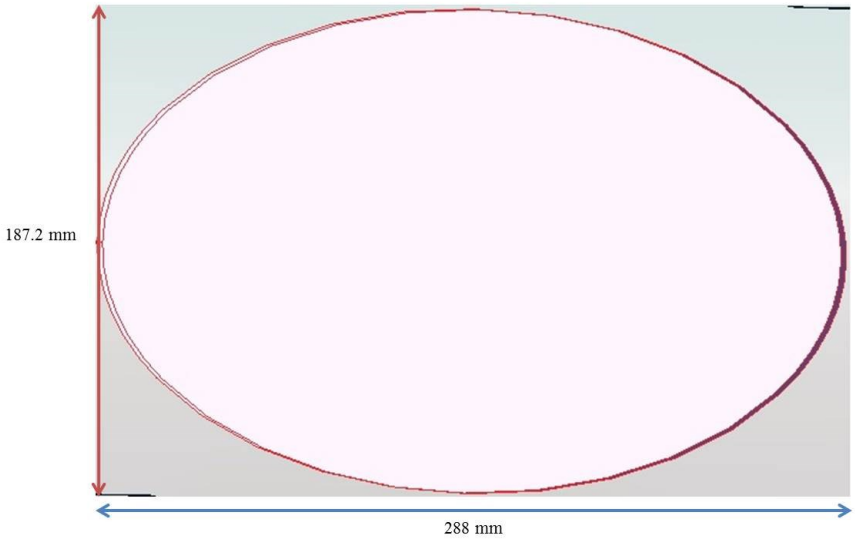

Figure 6.15 Top view of torso model of human body

For loop antenna, a human arm model is used consisting of five layers; skin, fat, muscle, bone and bone as illustrated in Figure 6.16.

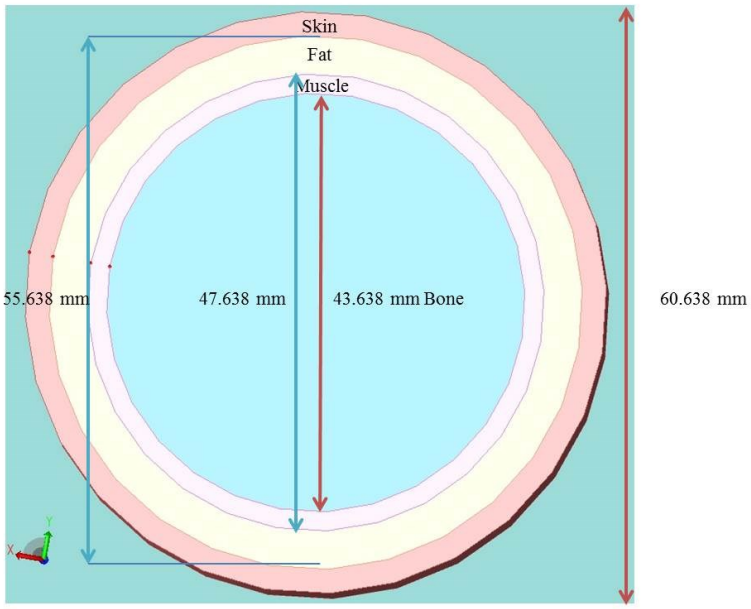

Figure 6.16 Arm model consisting of skin, fat, muscle, and bone layers

Antenna performance characteristics for several antennas are listed, namely reflection coefficient, antenna input impedance, resonant frequency shift, radiation efficiency, and realized gain for both free space case and on-body antennas. Some antennas are found to be more immune to effects from body tissue as expected when a ground plane shields the fields.

6.4.1 Simulation Setup

A one volt is applied to the input port of each antenna studied with 50 Ohm source impedance except for bow-tie antennas which use 200 Ohm source impedance. In Table 6.4, the simulation settings are set for the Finite-Element Method (FEM) solver to run EM simulation for all the three bow-tie antennas.

Table 6.4 Simulation settings for FEM solver for monopole, patch, PIFA, loop, and bow-tie antennas

Mesh/Discretization	
Delta error	0.01
Minimum number of adaptive passes	5
Maximum number of adaptive passes	25
Refining at highest frequency	1 GHz
Consecutive passes of delta error required	2
Mesh refinement percentage	25
Target mesh size	Automatic
Automatic Conductor Meshing	
Order of basis functions	2
Minimal Mesh Size	0.9375 mm
Merging object of same material	yes

After adjusting the FEM simulation settings and selecting automatic padding based on sever layers of Perfect Matched Layer (PML) absorbing boundary conditions to eliminate the effects of reflections from the radiating fields in the simulation domain. Then, a far zone sensor is added to quantify antenna radiation characteristics in the far-field. Finally, the simulation is run until the value of delta error shown between consecutive errors does not exceed 0.01 which is a reasonable value with the values of other parameters presented in Table 6.4 and mostly results in sufficiently accurate S-parameters at normal convergence rate.

6.4.2 Reflection Coefficient, Resonant Frequency shift, and Bandwidth

6.4.2.1 Monopole Antenna

The antenna is placed in proximity to elliptical approximation of torso model [121] made of muscle (5 mm antenna-body distance) as shown in the simulation setup in Figure 6.17. In Figure 6.18 and Figure 6.19, the magnitude and smith chart of reflection coefficient for fabric monopole antenna are plotted for free space and on-body case.

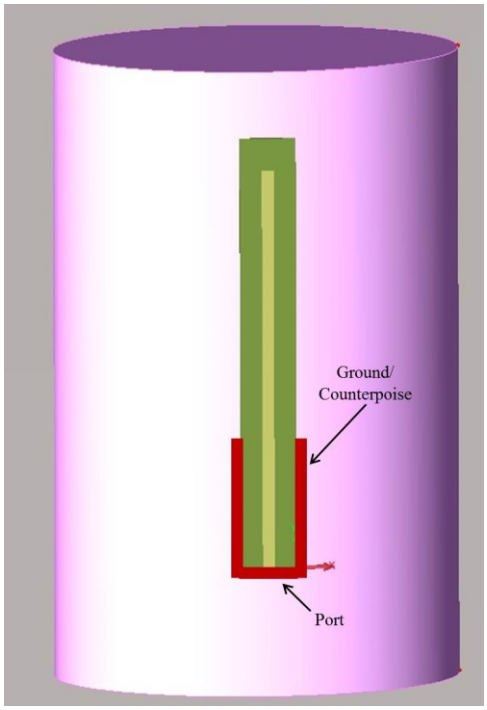

Figure 6.17 Simulation Setup for monopole antenna on torso model from [121] but made of muscle tissue

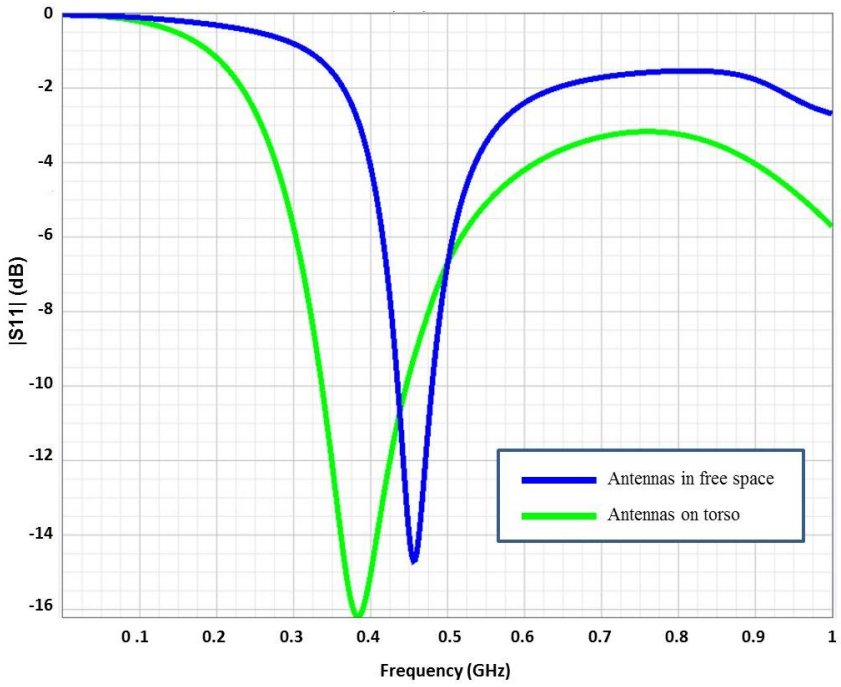

Figure 6.18 Magnitude of S11 for monopole antenna in free space and on-body

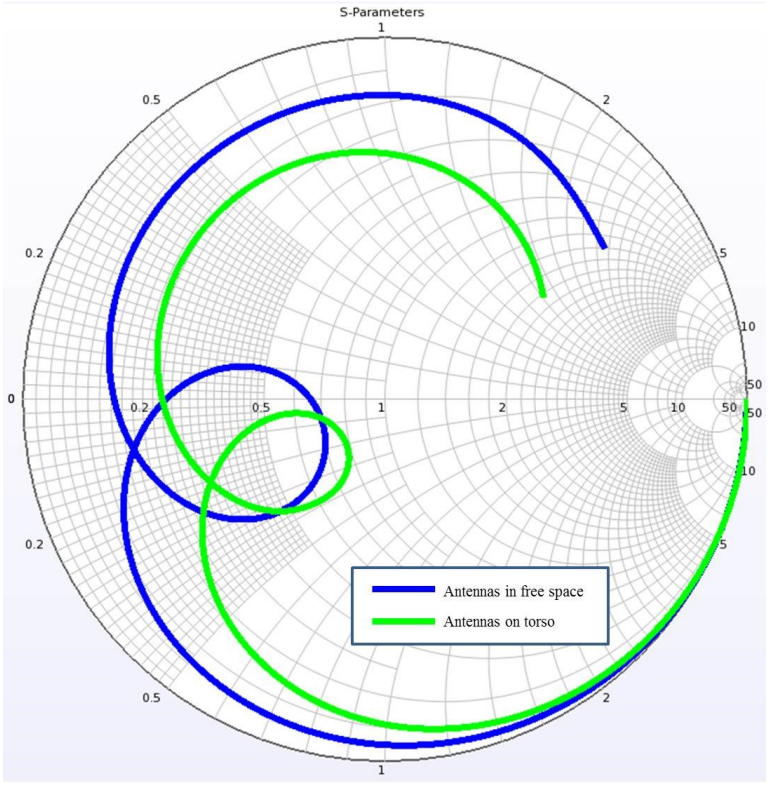

Figure 6.19 Smith Chart of S11 for monopole antenna in free space and on-body

It can be noticed that the resonant frequency is shifted from 458 MHz to 393 MHz in Figure 6.18. Also, the 10 dB bandwidth is widened when the antenna is placed on-body (113.3 MHz) compared to that of free space case (44.84 MHz).

6.4.2.2 Patch Antenna

The antenna is placed in proximity to body tissue (5 mm antenna-body distance) as shown in the simulation setup in Figure 6.20 (flat in the left and bent to fit the surface of the torso model on the right). In Figure 6.21 and Figure 6.22, the magnitude and smith chart of reflection coefficient for fabric patch antenna are plotted for free space and on-body case.

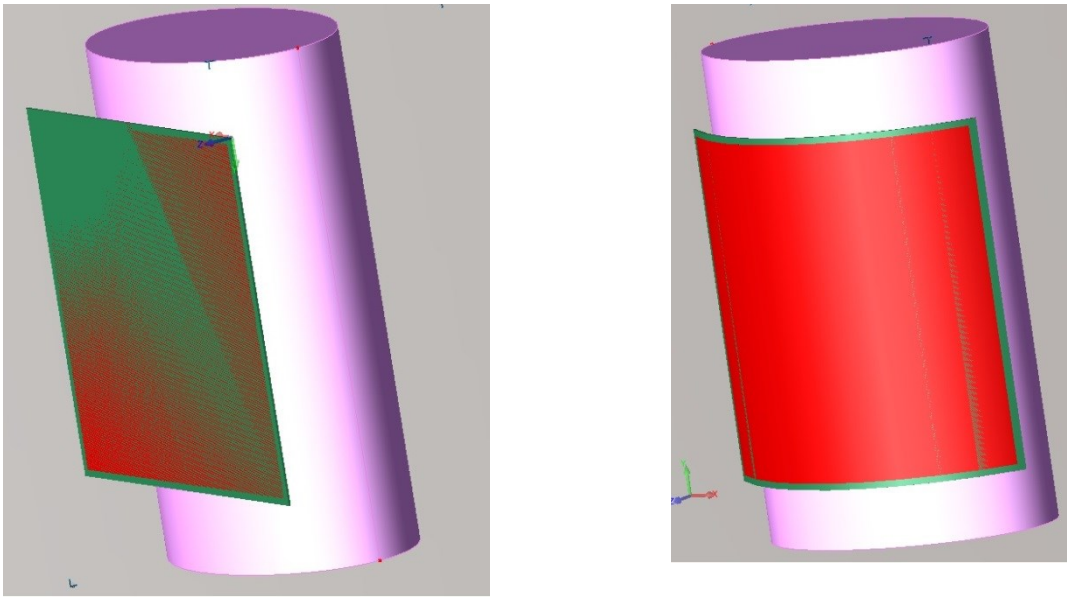

Figure 6.20 Simulation Setup for patch antenna on body with 5mm separation

It can be noticed from Figure 6.21 that resonant frequency and bandwidth are not significantly affected for this antenna. This can be expected since the ground plane shields the operation from the body effects.

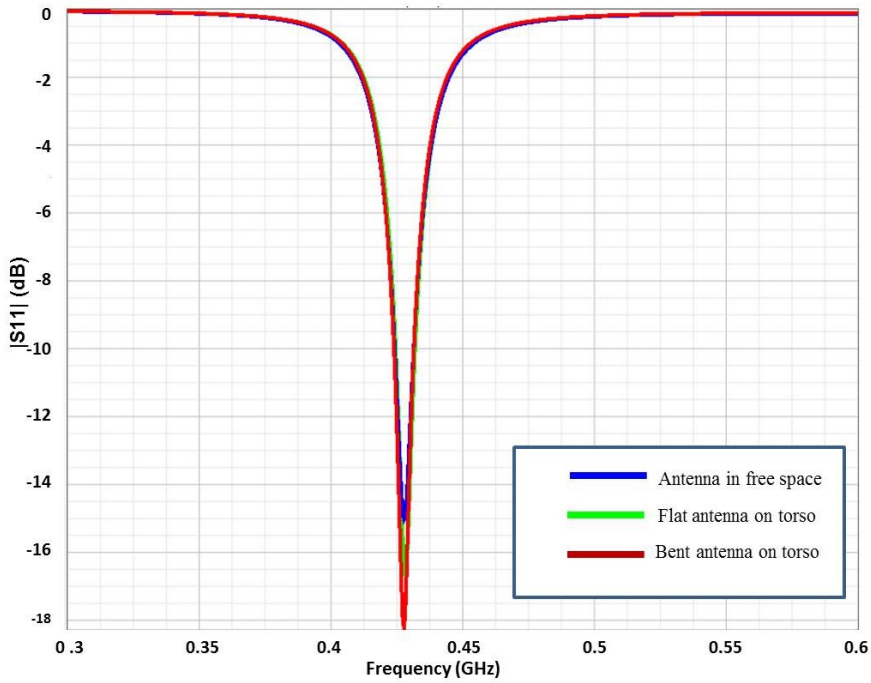

Figure 6.21 Magnitude of S11 for patch antenna in (1) Free space and (2) Flat antenna on-body, and (3) Bent on Body

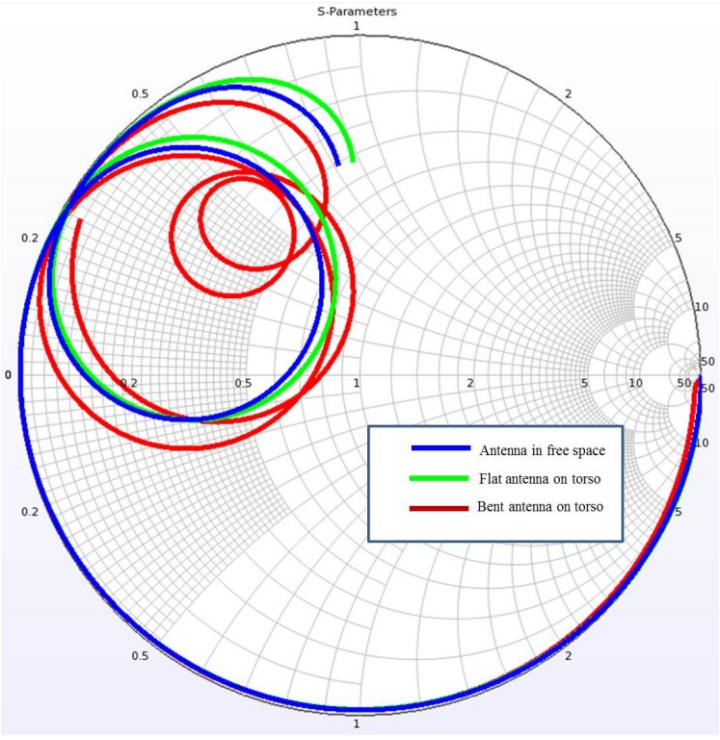

Figure 6.22 Smith Chart of S11 for patch antenna in free space (blue) and flat on-body (green) and bent on-body (red)

Table 6.5 Summary of S11 patch antenna performance characteristics

Parameters	Microstrip Patch Antenna
10 dB Bandwidth in Freespace	7.4 MHz
10 dB Bandwidth flat antenna on body	7.4 MHz
10 dB Bandwidth bent antenna on body	7.4 MHz

6.4.2.3 Planar Inverted F Antenna (PIFA)

The antenna is placed in proximity to body tissue (5 mm antenna-body distance) as shown in the simulation setup in Figure 6.23. In Figure 6.24 and Figure 6.25, the magnitude and smith chart of reflection coefficient for fabric monopole antenna are plotted for free space and on-body case.

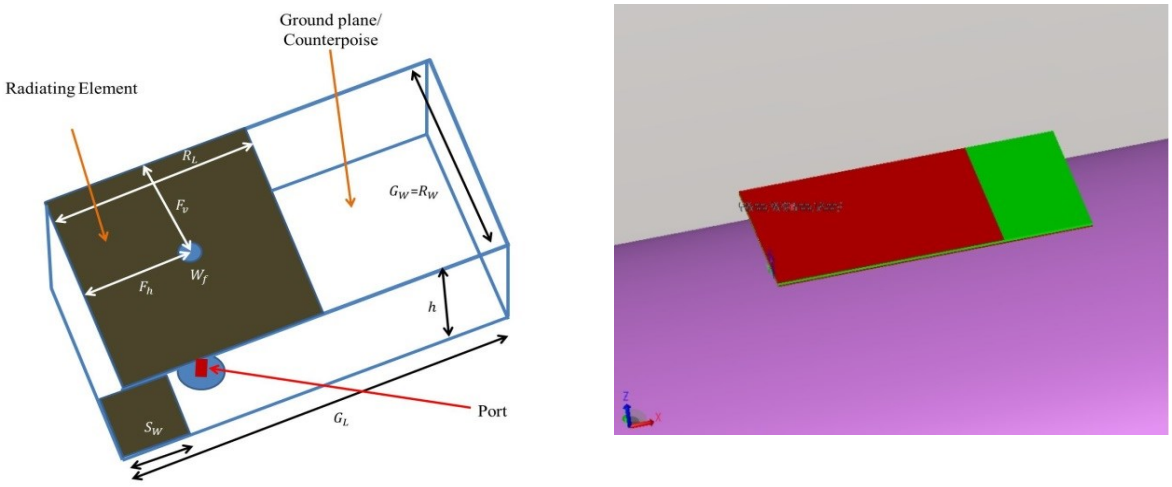

Figure 6.23 Antenna geometry (left) and simulation setup for PIFA antenna on body (right)

As in the case of the patch design, this antenna is shielded from the body by its ground plane.

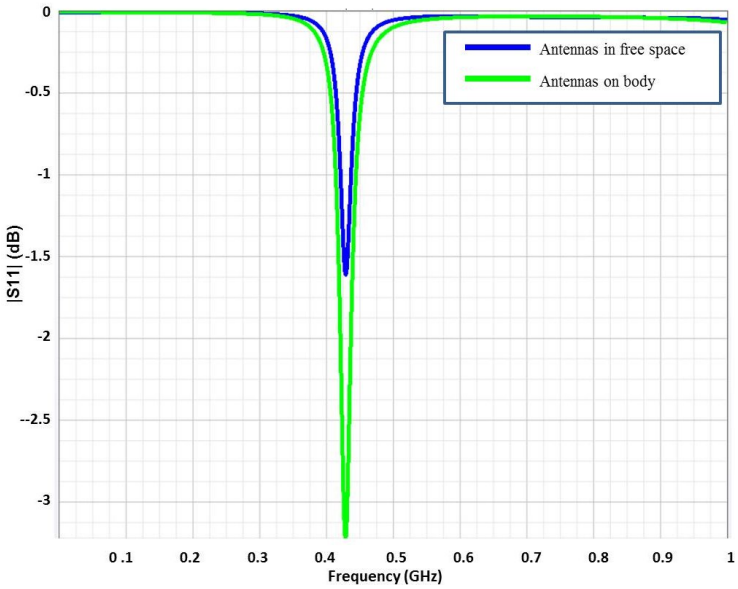

Figure 6.24 Magnitude of S11 for PIFA antenna in (1) Free space and (2) antenna on-body

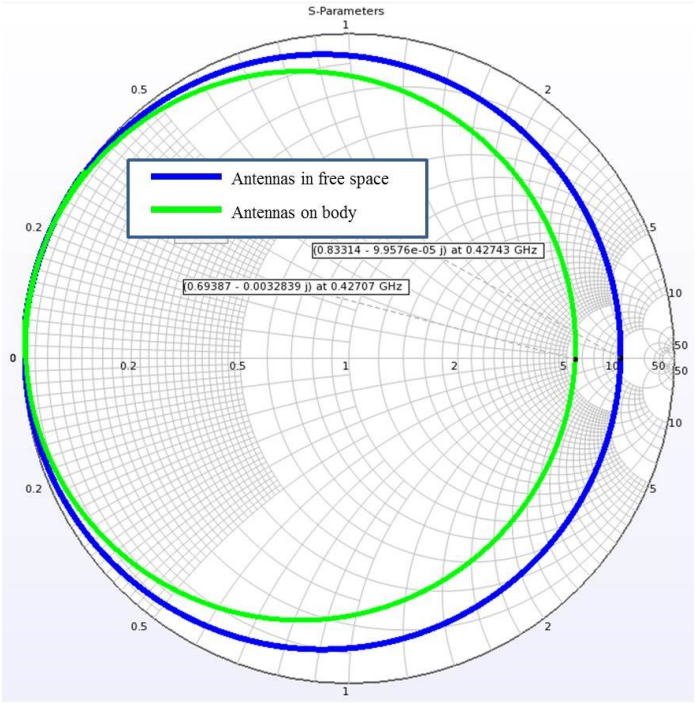

Figure 6.25 Smith Chart of S11 for PIFA antenna in (1) Free space and (2) Flat antenna on-body

6.4.2.4 Small-Loop Antenna

The antenna is placed in proximity to body tissue (5 mm antenna-body distance) as shown in the simulation setup in Figure 6.26. Figure 6.27 and Figure 6.28, the magnitude and smith chart of reflection coefficient for small-loop antenna are plotted for free space and on-body case.

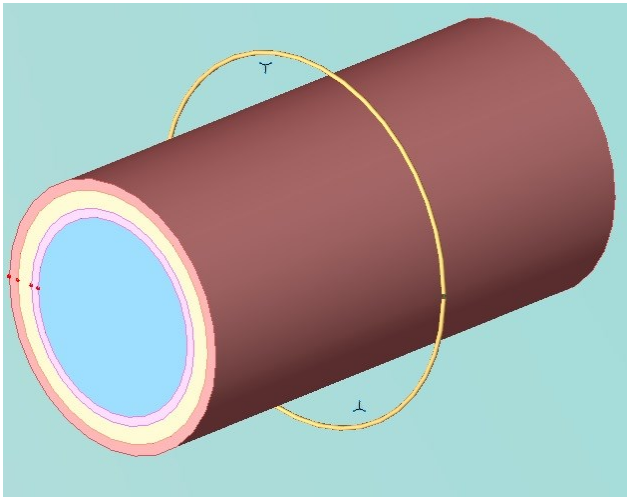

Figure 6.26 Simulation Setup for Small Loop antenna around wrist

We can notice from Figure 6.27 that there is no resonant dip at 433 MHz. This is expected since the circumference of the loop antenna equals 157 mm which does not form a fraction of wavelength at 433 MHz (wavelength at 433 MHz is 692 mm) but at higher frequency around 1.2 GHz. We can notice from Figure 6.28 that the curve for free space and on-body is almost identical up to 545 MHz and then it start to differ where a resonance can be observed at 716 MHz.

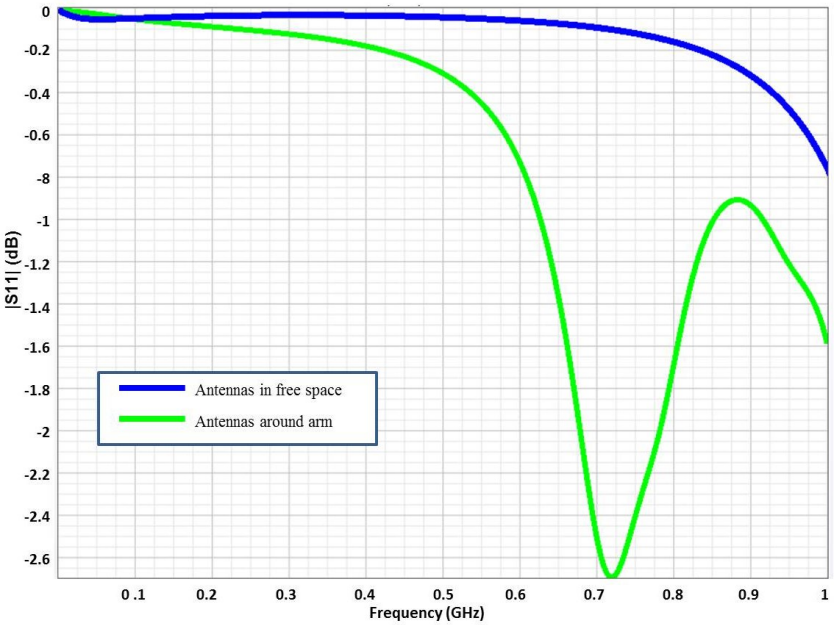

Figure 6.27 Magnitude of S11 for small loop antenna in free space and around arm

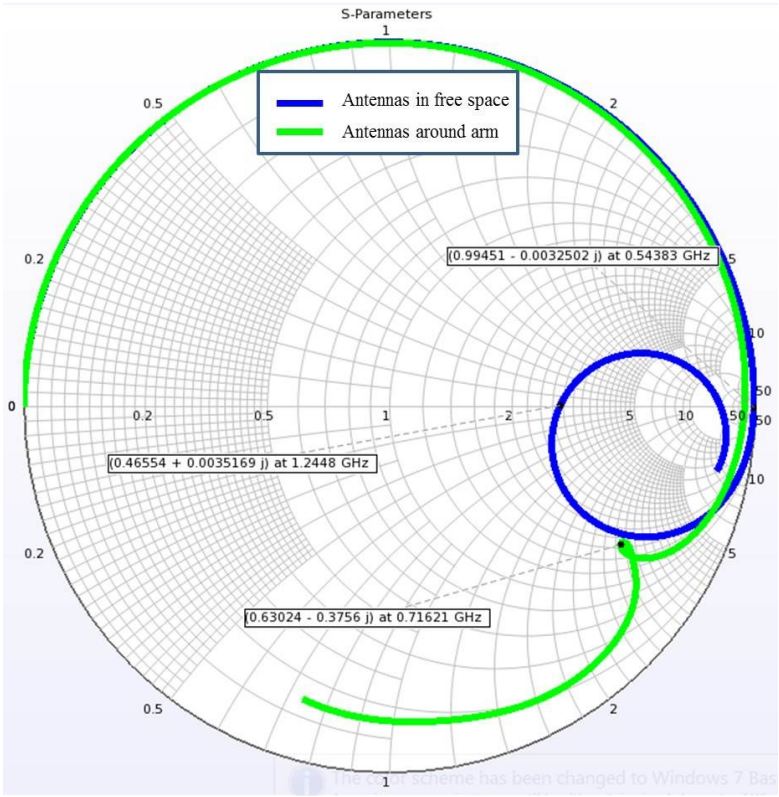

Figure 6.28 Smith Chart of S11 for loop antenna in free space and around arm

6.4.2.5 Bow-Tie Antennas

The antenna is placed in proximity to body tissue (5 mm antenna-body distance) as shown in the simulation setup in Figure 6.29. In Figure 6.30 and Figure 6.31, the magnitude and smith chart of reflection coefficient for fabric bow-tie antenna are plotted for free space and on-body case.

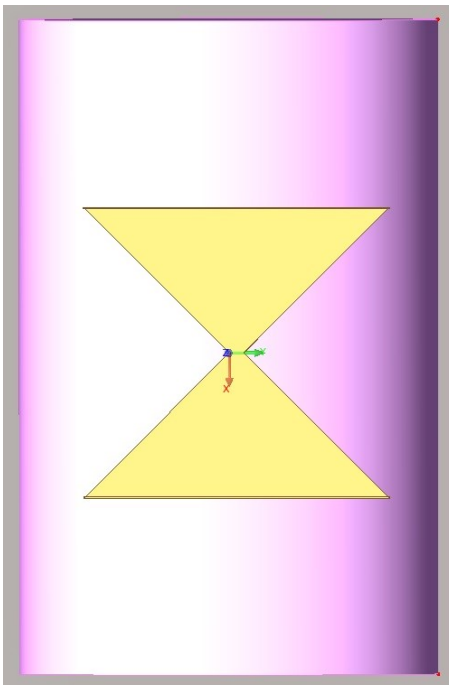

Figure 6.29 Simulation Setup for self-shielded folded bow-tie antenna on torso

In Figure 6.30, the smith chart of reflection coefficient for two bow-tie antennas are plotted for free space; the conventional bow-tie antenna and the folded bow-tie antenna in blue and green colors, respectively. Then, the smith chart representation of our proposed self-shielded folded bow-tie antenna is plotted in red curve. The antenna is placed in proximity to body tissue (5 mm antenna-body distance) as shown in the simulation setup in Figure 6.30. It can be noticed from Figure 6.31 that at DC, the conventional bow-tie is open circuit (blue curve) which is expected as the two triangles forming the bow-tie are disconnected. However, for case of folded

bow-tie and self-shielded folded bow-tie, the port is short-circuited since for both of these geometries, the two triangles are shorted.

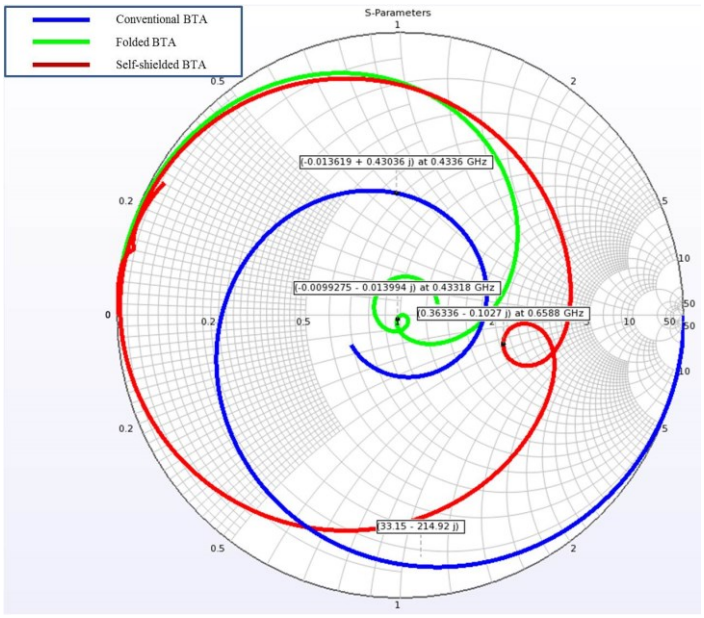

Figure 6.30 Smith Chart of S11 of three types of Bow Tie Antennas in free space 200 Ohm BTA (blue), 200 Ohm Folded BTA (green), and proposed 200 Ohm Self-Shielded Folded BTA antenna (red)

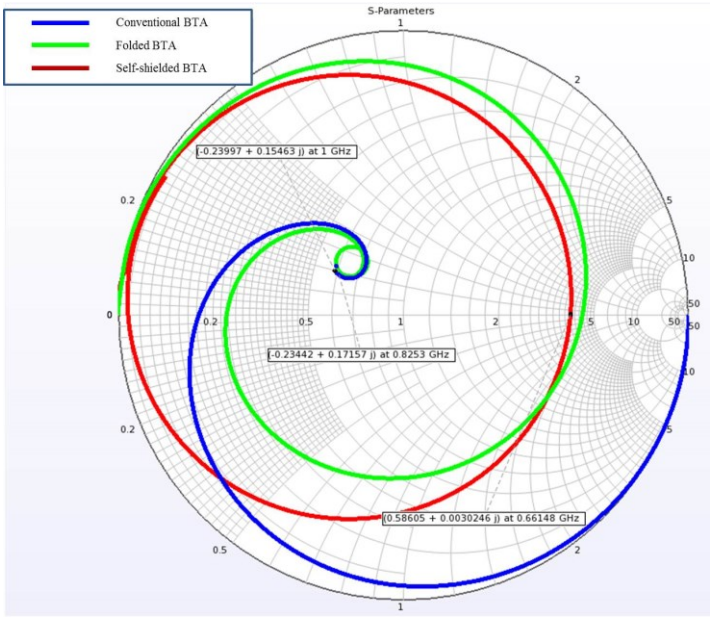

Figure 6.31 S11 of three types of Bow Tie Antennas on body with 5 mm antenna-body distance: Conventional BTA (blue), Folded BTA (green), Self-Shielded Folded BTA (red)

6.4.3 Radiation Efficiency

To simulate the radiation efficiency and later realized gain of the antenna in EMPro 2013.07, a far field sensor is used that collects data for all theta and phi angels (i.e., azimuth and elevation angles, respectively). This sensor will collect the actual antenna performance characteristics regardless of the antenna is match or not. For matching and obtaining maximum total efficiency of the antenna (i.e., e_0 in Eq. (2.16)), we can export the antenna geometry to another EM software to build a matching network.

6.4.3.1 Monopole Antenna

The radiation efficiency for fabric monopole antenna is listed in Table 6.6 for free space and on-body case. Also, the radiation efficiency is plotted for a range of 1 Hz to 1 GHz in Figure 6.32. It can be observed that a maximum radiation efficiency of 90% occurs at 450 MHz for free space case whereas it is very low (2.5%) for on-body case at least up to 1 GHz. This can be expected because most near-fields interact with the human body and will be absorbed due to having small partial ground plane.

Table 6.6 Radiation Efficiency of Monopole Antenna at 450 MHz

Environment of antenna placement	Radiation efficiency
Free space	90%
On-body (5 mm distance)	2.5%

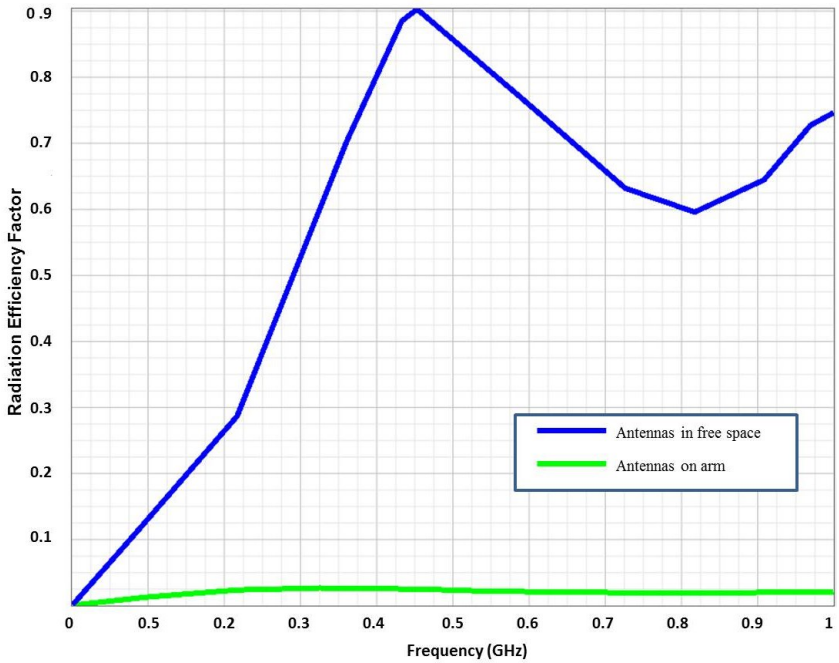

Figure 6.32 Simulated Radiation Efficiency Factor for Monopole Fabric Antenna

6.4.3.2 Patch Antenna

The radiation efficiency for fabric patch antenna is listed in Table 6.7 for free space and on-body case. The radiation efficiency is plotted for a range of 10 Hz to 1 GHz in Figure 6.33. It can be observed that the maximum radiation efficiency occurs at 548 MHz for free space case (61%) whereas it is at 396 MHz for on-body case (i.e. 42%). Compared with the degradation of radiation efficiency seen in monopole antenna, it can be observed that the radiation efficiency did not drop significantly. Rather, the antenna resists the effects of body tissues due to utilizing full ground plane.

Table 6.7 Radiation Efficiency of Patch Antenna at 433 MHz

Environment of antenna placement	Radiation efficiency
Free space	51%
Flat On-body (5 mm distance)	41%
Bent On-body (5 mm distance)	41%

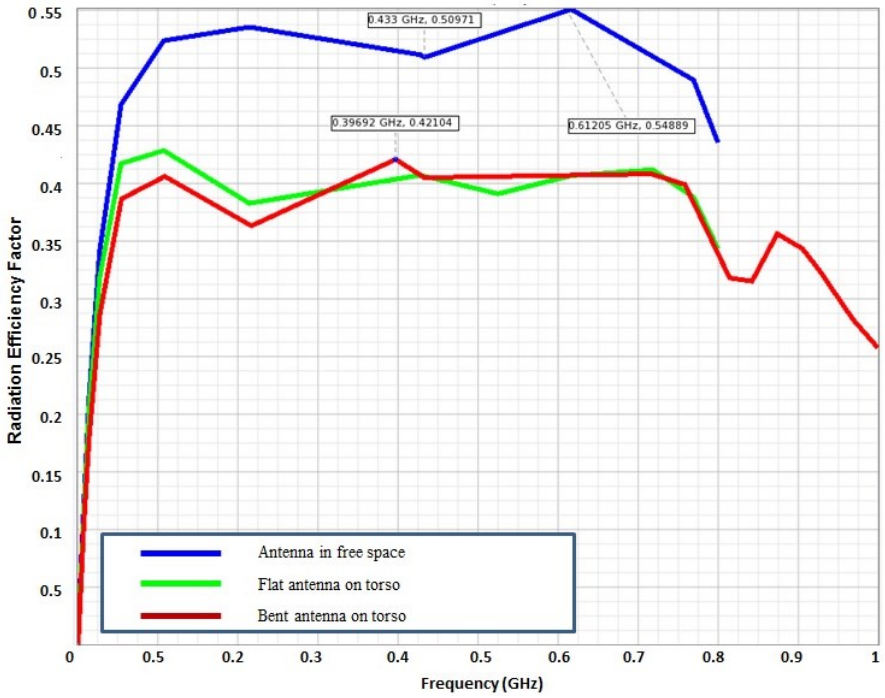

Figure 6.33 Simulated Radiation Efficiency Factor for Patch Antenna

6.4.3.3 Planar Inverted F Antenna (PIFA)

The radiation efficiency for fabric planar inverted F antenna (PIFA) is listed in Table 6.8 for free space and on-body case. Also, the radiation efficiency is plotted for a range of 100 MHz to 1 GHz in Figure 6.34. It can be observed that the maximum radiation efficiency occurs at 700 MHz for free space case (i.e., 80%) whereas it is at 1 GHz for on-body case in this range (53%).

Table 6.8 Radiation Efficiency of PIFA Antenna at 433 MHz

Environment of antenna placement	Radiation efficiency
Free space	41%
On-body (5 mm distance)	23%

It can be observed from Table 6.8 that the radiation efficiency drop from 41% for free space case to 23% for on-body case at 433 MHz. This drop is expected since the PIFA antenna still has some near-fields coupling with the body tissue and absorbing certain amount of the radiated power.

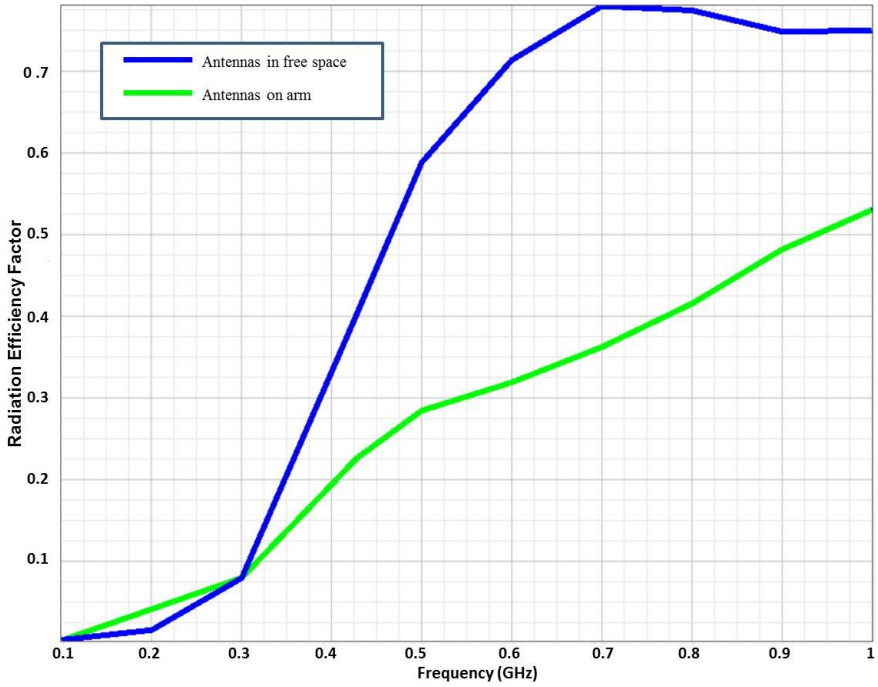

Figure 6.34 Simulated Radiation Pattern Factor for PIFA Antenna for free space (blue) and on-body scenario (green)

6.4.3.4 Small-Loop Antenna

The radiation efficiency for small loop antenna is listed in Table 6.9 for free space and on-body case. Also, the radiation efficiency is plotted in Figure 6.35 for a range of 1 MHz to 1 GHz. It can be observed from Table 6.9 that the radiation efficiency for free space case is high while it drops to 23% when the loop antenna is worn on the wrist model due to having electromagnetic field interaction with the body tissues.

Table 6.9 Radiation Efficiency of Small Loop Antenna at 433 MHz

Environment of antenna placement	Radiation efficiency
Free space	96%
On-body (5 mm distance)	23%

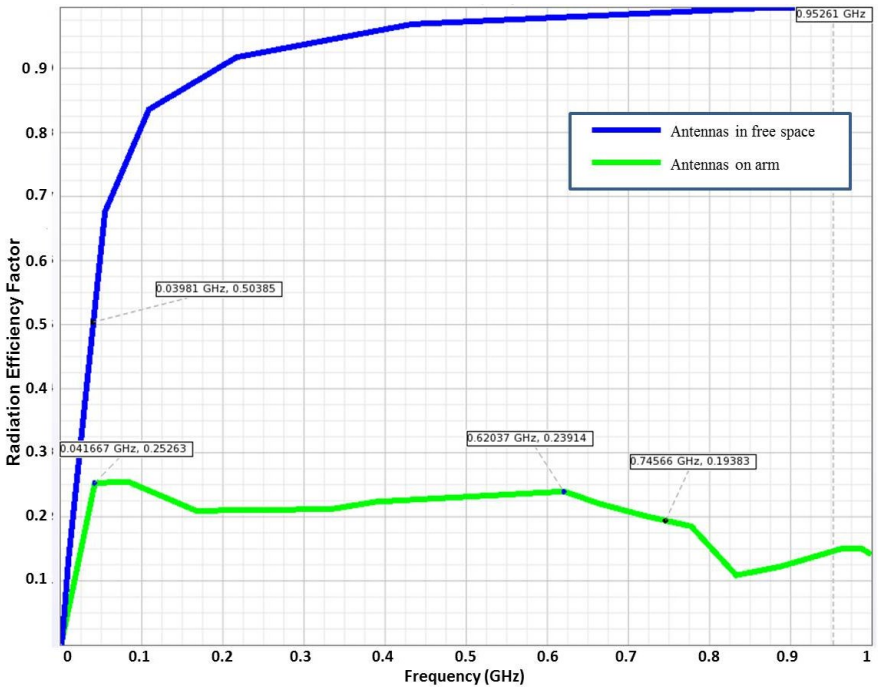

Figure 6.35 Simulated Radiation Efficiency vs. frequency for small loop for free space and around Wrist with N=1

6.4.3.5 Bow-Tie Antennas

The radiation efficiency is plotted for a range of 1 Hz to 1 GHz in Figure 6.36. It can be observed that the radiation efficiency is high (i.e., 95%) starting from occurs at 250 MHz for free space case whereas the maximum is at 700 MHz for on-body case (73%).

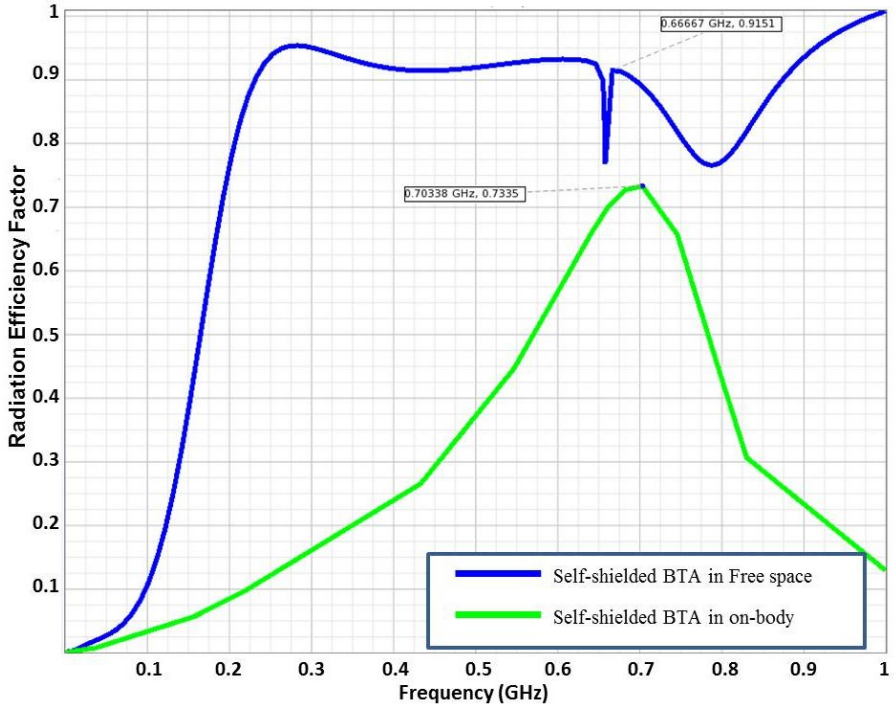

Figure 6.36 Simulated Radiation Efficiency Factor vs. frequency for proposed Self-Shielded Folded BTA at free space and on-body (5 mm ant body separation)

It can be noticed from Figure 6.37 that at 433 MHz that radiation efficiency of conventional bow-tie is 4.5% while there is insignificant improvement for the case of folded bow-tie (i.e., 6%). On the other hand, we can observe that the performance of proposed self-shielded folded bow-tie antenna is superior to both conventional and folded bow-tie antennas with regard to radiation efficiency. Specifically, the radiation efficiency is quadrupled (i.e., 26%)

compared to that for folded bow-tie antenna (i.e., 6%). These resulted are summarized in Table 6.10.

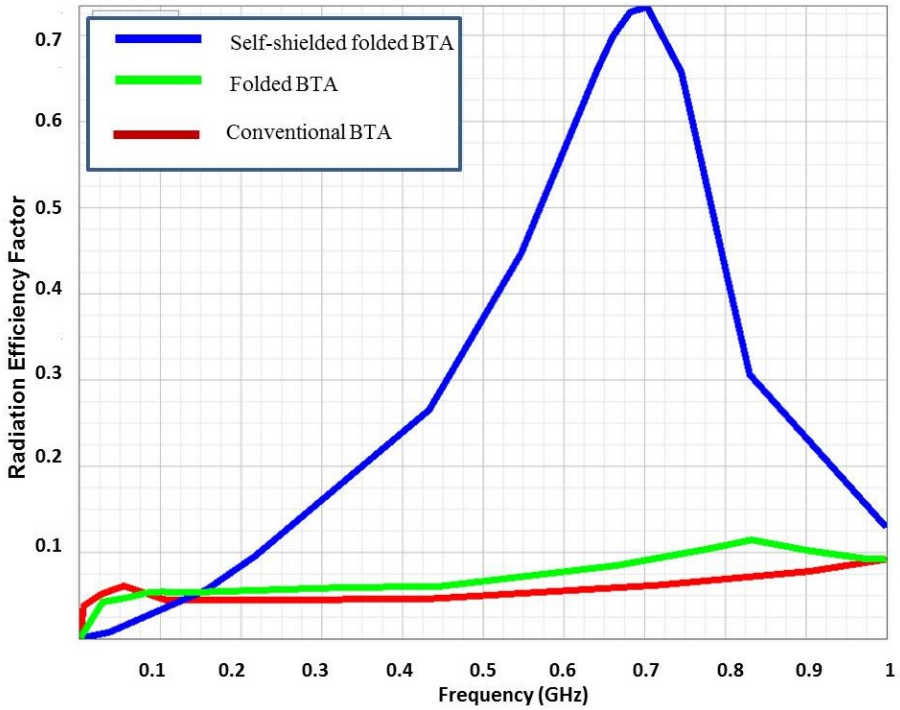

Figure 6.37 Comparision of Simulated Radiation Efficiency Factor vs. frequency for proposed Self-Shielded Folded BTA, Folded BTA, and conventional BTA for on-body Scenario (5 mm ant body separation)

Table 6.10 Radiation Efficiency of Bow-Tie Antennas

	Environment of antenna placement	Radiation efficiency
Conventional Bow-Tie Antenna	Free space	92% at 433 MHz
	On-body (5 mm distance)	4.5% at 433 MHz, 7.2% at 850 MHz
Folded Bow-Tie Antenna	Free space	100% at 433 MHz
	On-body (5 mm distance)	6% at 433 MHz, 9.2% at 1000 MHz
Self-Shielded Folded Bow-Tie Antenna	Free space	92.8% at 433 MHz, 92.3% at 658 MHz
	On-body (5 mm distance)	26.5% at 433 MHz, 70% at 661 MHz

We anticipate that by using a tuning capacitor, the peak radiation efficiency seen at 661 MHz can be adjusted to be produce antenna with radiation efficiency of the same order. Further improvements in the antenna design are discussed in Chapter 7.

6.4.4 Realized Gain

Realized gain by definition is the gain of antenna taking into account the impedance matching factor. Thus, the maximum value of realized gain is the gain value when the antenna impedance is matched to the port impedance.

6.4.4.1 Monopole Antenna

The realized gain for fabric monopole antenna is listed in Table 6.11 for free space and on-body case. Also, 3D pattern of realized gain radiation pattern is depicted in Figure 6.38 (right).

Table 6.11 Peak Realized Gain of Bow-Tie Antennas

Environment of antenna placement	Peak Realized Gain
Free space	0 dBi
On-body (5 mm distance)	-12 dBi

The significant gain drop seen in Table 6.11 by 12 dB is not consistent with the drop in radiation efficiency presented previously (from 90% to 2.5%). One possible interpretation is that since the realized gain takes into consideration the matching of the input impedance of the antenna whereas the radiation efficacy does not, the order of input impedance (mostly reactive part of the impedance) might have changed significantly when the antenna is mounted on-body which varies greatly with the impedance of the 50 Ohm port used.

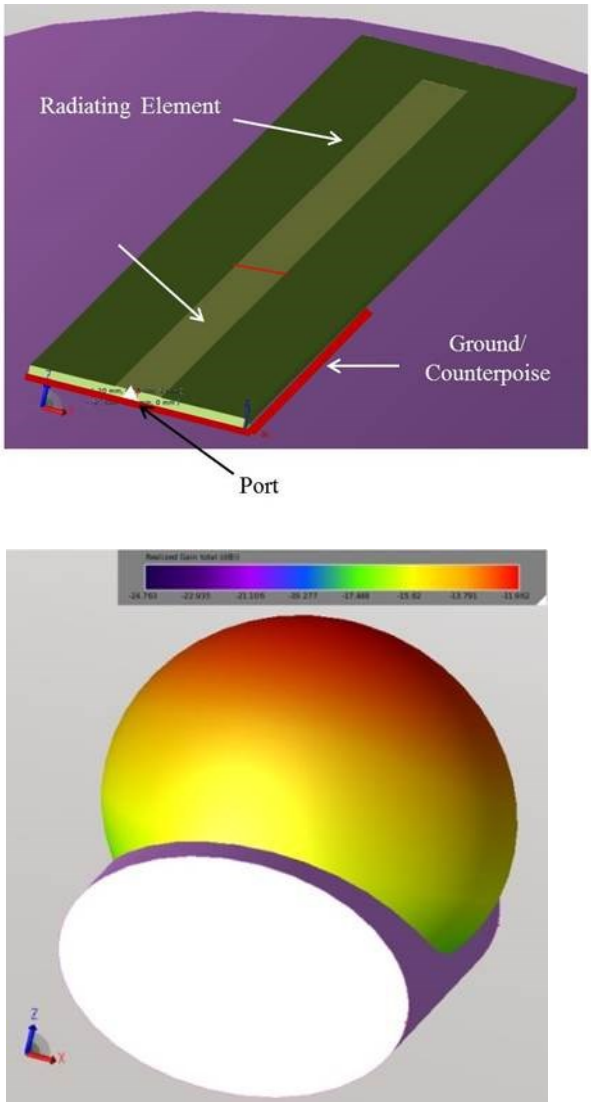

Figure 6.38 Fabric monopole on arm setup (top), simulated realized gain radiation pattern for on-body case (bottom)

6.4.4.2 Patch Antenna

The realized gain for fabric patch antenna is listed in Table 6.12 for free space and on-body case. Also, 3D pattern of realized gain or radiation pattern is depicted in Figure 6.39 (right).

Table 6.12 Peak Realized Gain of Patch Antenna

Environment of antenna placement	Peak Realized Gain
Free space	2.5 dBi
On-body (5 mm distance)	2.4 dBi

It can be observe from Table 6.12 that the peak realized gain basically maintained its good value even when the antenna is bent by around 80 degrees. One explanation is that having full ground plane minimizes the negative effects of body tissues on antenna performance.

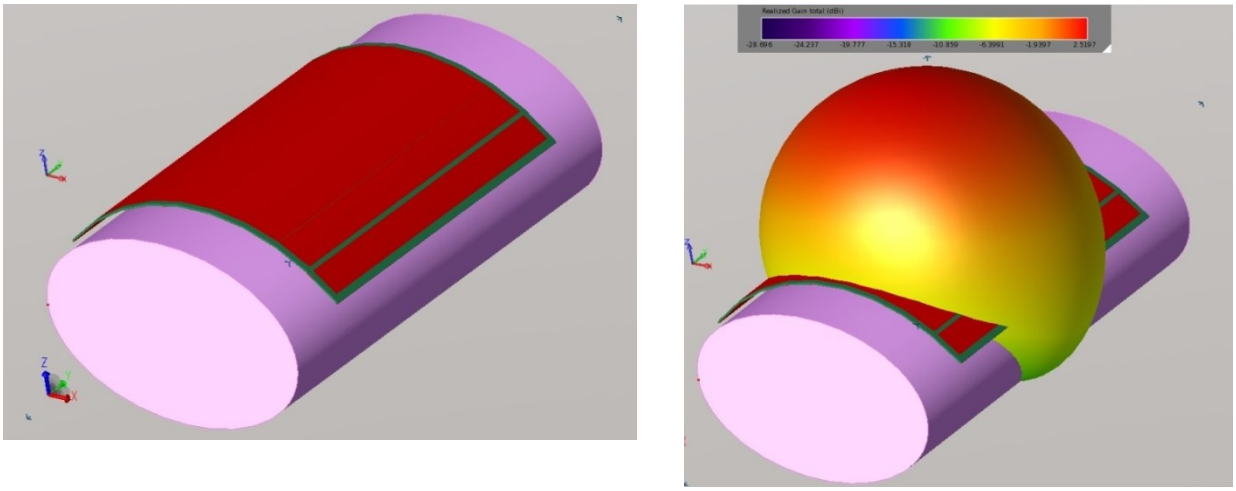

Figure 6.39 Fabric patch on torso setup (left), simulated realized gain radiation pattern for on-body case (right)

6.4.4.3 Planar Inverted F Antenna

The realized gain for fabric planar inverted F antenna (PIFA) is listed in Table 6.13 for free space and on-body case. Also, 3D pattern of realized gain or radiation pattern is depicted in Figure 6.40 (bottom).

Table 6.13 Peak Realized Gain of PIFA Antennas at 433 MHz

Environment of antenna placement	Peak Realized Gain
Free space	-8 dBi
On-body (5 mm distance)	-7.5 dBi

It can be observe from Table 6.13 that the peak realized gain is essentially low in free space case. After placing the antenna on body, the peak realized gain dropped by a half dB only.

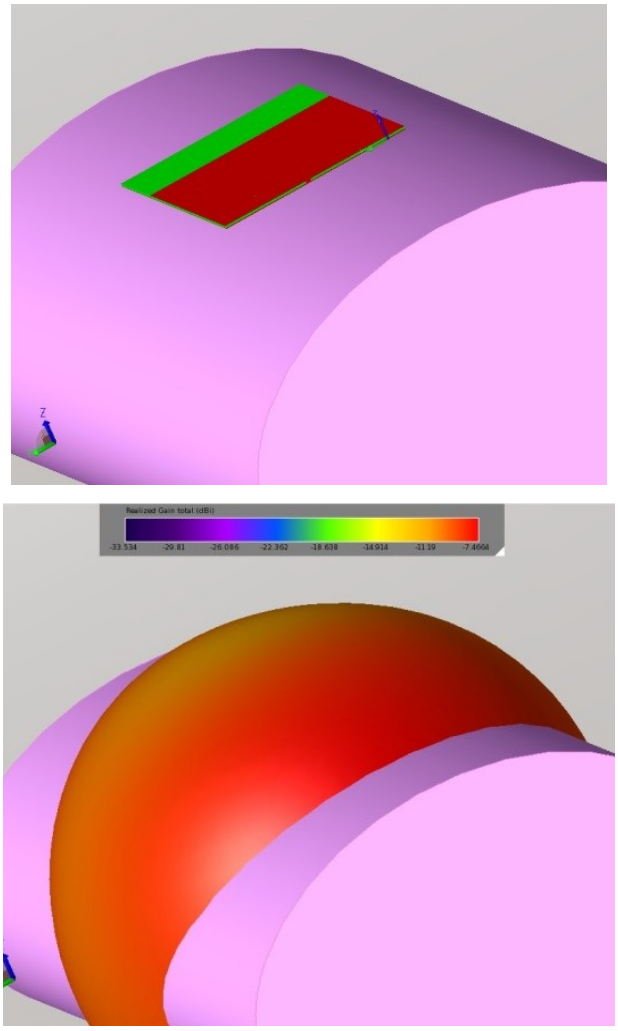

Figure 6.40 Fabric Planar Inverted F Antenna (PIFA) on torso setup (left), simulated realized gain radiation pattern for on-body case (right)

6.4.4.4 Small-Loop Antenna

The realized gain for fabric small loop antenna is listed in Table 6.14 for free space and on-body case at 433 MHz. Also, 3D pattern of realized gain or radiation pattern is depicted in Figure 6.41 (right).

Table 6.14 Peak Realized Gain of Small-Loop Antennas at 433 MHz

Environment of antenna placement	Peak Realized Gain
Free space	-14 dBi
Around Wrist	-18 dBi

It can be noticed from Table 6.14 that the free space gain is -14 dBi whereas it decreased by 4 dB when worn around the wrist model at 433 MHz. This can be attributed to not using a resonating capacitor at the antenna. As known, the loop antenna is basically inductive and if a tuning capacitor is used, the whole structure resonates at certain frequency. The realized gain drops by 4 dB.

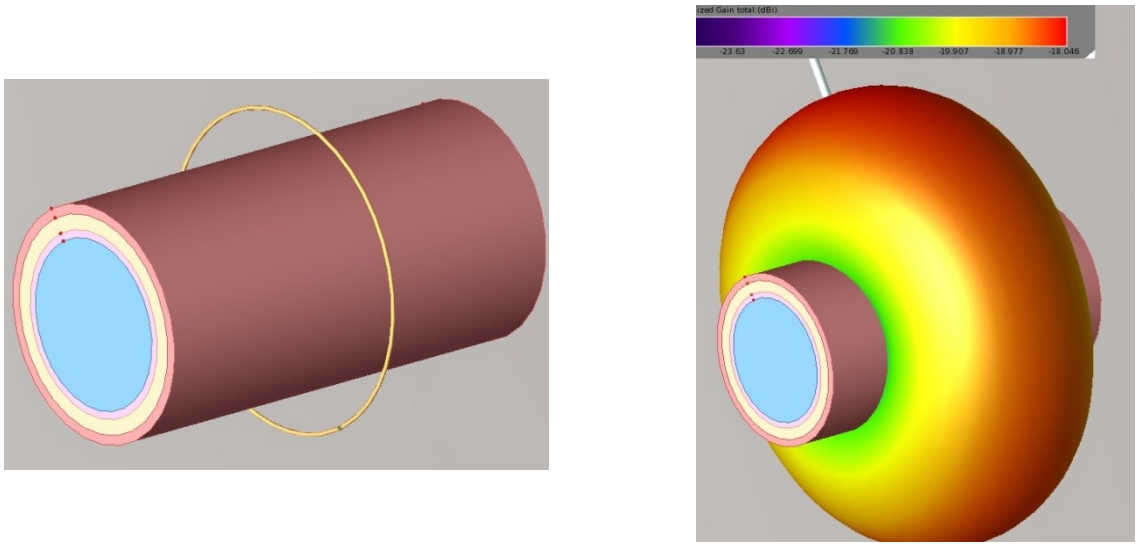

Figure 6.41 Fabric Small-Loop around arm setup (left), simulated realized gain radiation pattern for on-body case (right)

6.4.4.5 Self-Shielded Folded Bow-Tie Antenna

The realized gain for fabric self-shielded folded bow-tie antenna is listed in Table 6.15 for free space and on-body case. Also, 3D pattern of realized gain or radiation pattern is depicted in Figure 6.42 (right).

Table 6.15 Peak Realized Gain of proposed Self-Shielded Folded Bow-Tie Antenna

Environment of antenna placement	Peak Realized Gain
Free space	-11.7 dBi
On-body (5 mm distance)	-16 dBi

It can be observed from Table 6.15 that the realized gain in free space is basically low (i.e., -11.7 dBi). Then, it dropped by approximately 5 dB when placed on body. One interpretation is that since the realized gain takes into account the antenna mismatch loss with the 200 Ohm port impedance, the realized gain is low although the radiation efficiency is fairly good compared to conventional bow-tie and folded-bow-tie antenna as seen in efficiency calculation earlier. To solve this issue, designing a good matching network is anticipated to produce a good total antenna efficiency stated in Eq. (2.16).

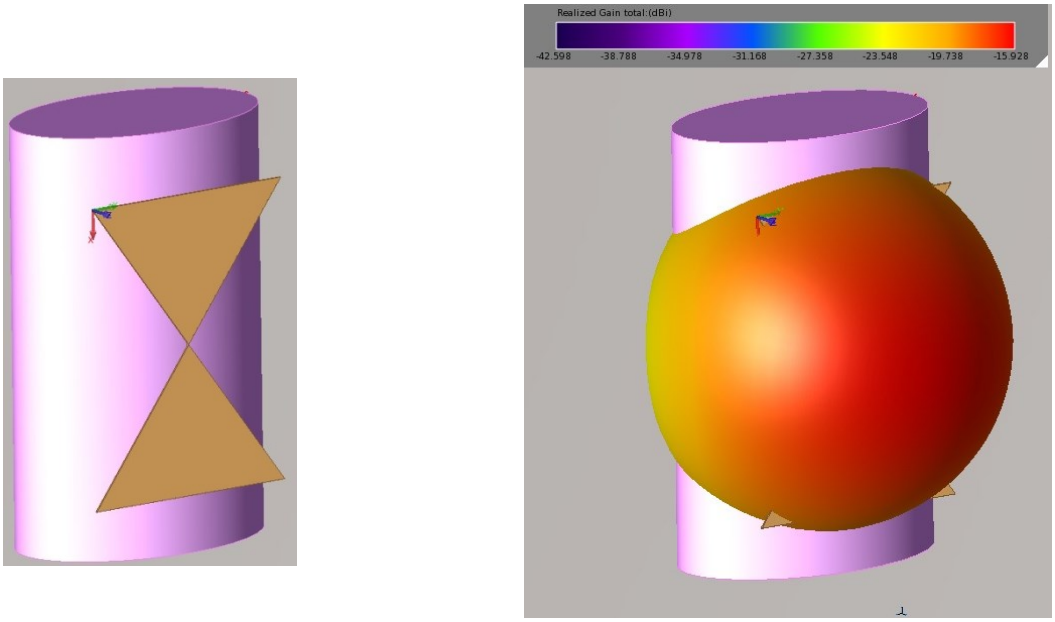

Figure 6.42 Fabric self-shielded bow-tie antenna on torso setup (left), simulated realized gain radiation pattern for on-body case (right)

6.5 Chapter Summary

In this chapter, we have reviewed several possible antennas for off-body communications. In particular, we studied the antennas for use in the MedRadio band as it falls within the transition region (200-500 MHz) for which limited interaction is available in the current literature. Finally, we presented a comparative study of performance in terms of return loss, bandwidth, and radiation efficiency, and proposed a novel antenna design that overcomes the shortcomings found in existing antennas. This new bow-tie design provides improved radiation efficiency in the presence of human body tissue absorption by employing a self-shielding design.

Chapter 7 - Conclusion and Future Work

7.1 Summary

Wireless body area networks have numerous applications in civilian, medical, military domains. An astronaut BAN for health monitoring represents a new application domain that requires a detailed study of intra-space suit propagation environment. In this dissertation, a thorough study of the intra-suit radio channel characteristics and human body effects was performed. We found that the intra-space suit propagation environment can be modeled as a coaxial cable propagation structure with the body serving as a lossy center conductor and the conductive suit material taking the role of the outer shield. We observe that at 433 MHz, 915 MHz, 2.4 GHz, and 5.2 GHz, when antennas with vertical polarization are mounted on the body, the resulting path loss is less compared to that resulting from the use of horizontally polarized patch antennas. This is consistent with the TEM wave model proposed. While the intra-space suit radio channel exhibits reasonable attenuation for all the frequency bands studied, the 433 MHz part of the MedRadio and 5.2 GHz bands provide the best path loss performance. However, designing practical antennas at 433 MHz is a challenge. Overall, the space suit is quite conducive to radio propagation. For example, the maximum path loss was measured to be approximately 90 dB path loss which is good for low data rate communication (200 kb/s) using BPSK modulation. Also, this level of attenuation is acceptable for most commercial receivers.

The last chapter of this research was devoted to the design and performance characterization of common antennas that may operate in the MedRadio band. A novel modified version of bow-tie antenna called self-shielded bow-tie antenna that minimizes the body tissue effects and maximizes the radiation efficiency was proposed.

7.2 Future Work

As a project funded by the NASA EPSCoR program to investigate technologies for future space related missions, applying the findings of this research to build a full prototype WBAN sensor system would be the natural progression for this project.

Some specific research aspects that would provide a natural progression include:

7.2.1 Propagation Modeling inside Space suit

- Shielding characteristics of the aluminized Mylar insulation was found to be affected by material age and physical stress that the space suit experiences. These aspects need further investigation.
- The excitation method used to excite TEM wave in coaxial mode is believed to be valid. However, the simulation model underlying this result (see Figure 4.5) can be improved. First, instead of using only one port at a certain point at the annular ring and the other end touching the outer conductor aluminum tube, infinite larger number of ports can be used along the circumference of each annular ring with the other pin of each port touching the outer conductor. This approach can help create an ideal TEM wave.
- Another improvement can be done in the simulation model in Figure 4.5 where each of the two ends of the coax structure can be terminated with the characteristic impedance for the coax model. This characteristic impedance may however be frequency-dependent due to the variation in the body tissue acting as the center conductor.
- Although the coax cable propagation model described in Subsection 4.1.2 is useful to get an idea about the propagation environment, this model is

deterministic and has some drawbacks. First, the path loss changes for small perturbations of the location and orientation of the transmit and receive antennas. Second, the coax model is not valid for channels operating at frequencies higher than the multi-mode frequency. Thus, we need to develop stochastic models to predict the received signal strength taking into consideration the variation of the received signal strength caused by several factors.

- Studying the radio channel at 13.5 MHz and the launching mechanism (magnetic field excitation) using RFID tags may be useful for a system that can accept the restricted modulation bandwidth this would imply. This approach may be sufficient for low rate data transfer that relies on the concept of inductive coupling.
- More thorough investigation of the motion effects of body parts such as arm or leg. For example, movement can result in polarization misalignment between the transmit and receive antennas, as illustrated in Eq. (2.22), which may degrade the quality of the received signal.
- Investigation of the effects of various body postures and activities such as walking, jogging, climbing on the intra-space suit radio channel performance should be done. In particular, the variability of received signal strength indicator (RSSI) due to fading and shadowing effects that may happen at higher frequencies could be quantified.
- Investigation of ultra-wideband off-body radio channels could be studied. Future space suits will likely integrate cameras that allow astronauts to capture images and videos and share them with scientists in the base habitat.

7.2.2 MedRadio Wearable Antennas

Future directions in the context of MedRadio wearable antenna designs are listed below:

- Designing matching networks for the un-matched antenna input impedances once for free space case and for off-body (which degraded the realized gain) case.
- Conducting a detailed analysis and comparison of the performance of our proposed self-shielded folded bow-tie antenna with that of the more conventional bow-tie and folded bow-tie antennas. This might include comparing the electric and magnetic field intensity and distribution on the surface of the antenna, the radiated power at a certain point in the far-field, radiation pattern and distortion of antennas in the vicinity of body section, realized gain of antennas after matching, the absorbed power by the torso body section in addition to the radiation efficiency used in our investigation. The findings of all these factors/parameters together should lead to more concrete evidence of the superiority of one antenna over the other.
- Building the wearable monopole, patch, planar inverted-F (PIFA) and bow-tie antennas using conductive copper fabric and felt substrate.
- Conducting antenna radiation measurements inside an RF anechoic chamber for off-body applications for the previous antennas. These can be worn/mounted on torso to measure their radiation efficiency, realized gain, radiation pattern, and compare the findings with simulation results obtained.
- Although the presented MedRadio antennas work well in an off-body environment, researching miniaturization techniques for these relatively big antennas is a research opportunity for enabling practical implementations.

Bibliography

[1] "A Profile of Older Americans: 2012, the Administration on Aging (AoA), U.S. Department of Health and Human Services," 2012. [Online]. Available: http://www.aoa.gov/Aging_Statistics/Profile/2012/docs/2012profile.pdf.

[2] "World Health Organization (WHO)," [Online]. Available: http://www.who.int.

[3] "Project: IEEE P802.15 Working Group for Wireless Personal Area Networks (WPANs)," April 2006. [Online]. Available: https://www.google.com/url?sa=t&rct=j&q=&esrc=s&source=web&cd=1&cad=rja&uact=8&ved=0CB4QFjAA&url=https%3A%2F%2Fmentor.ieee.org%2F802.15%2Fdcn%2F06%2F15-06-0217-00-0ban-ban-usage-scenarios-and-applications.ppt&ei=FuUhVZawDI7zoASJ7YHABw&usg=AFQjCNEI4SnLWW-u.

[4] M. G.Benedetto, T. Kaiser, A. Molishch, I. Oppermann, and D. Porcini, UWB communication systems: a comprehensive overview, Hindawi Publishing Corporation , 2006.

[5] "Medical Device Radiocommunications Service (MedRadio)," Federal Communication Commission , [Online]. Available: http://www.fcc.gov/encyclopedia/medical-device-radiocommunications-service-medradio. [Accessed 24 02 2015].

[6] "Wireless Medical Telemetry Service (WMTS)," FCC, [Online]. Available: http://www.fcc.gov/encyclopedia/wireless-medical-telemetry-service-wmts. [Accessed 24 02 2015].

[7] "Medical Body Area Networks," FCC, [Online]. Available: http://www.fcc.gov/document/medical-body-area-networks. [Accessed 24 02 2015].

[8] A. Hodges, "Investigation of antennas and energy harvesting methods for use with a UHF microtransceiver in a biosensor network, pp. 23," Dec 2013. [Online]. Available: https://krex.k-state.edu/dspace/bitstream/handle/2097/16218/AmeliaHodges2013.pdf?sequence=1.

[9] "NASA at K-State: Biosensor Networks and Telecommunication Subsystems for Long-Duration Missions, EVA Suits, and Robotic Precursor Scout Missions," Kansas State University, 18 July 2013. [Online]. Available: http://nasa.ece.k-state.edu/task1.html.

[10] P.S. Hall, Y. Nechayev, Y. Hao, A. Alomainy, M. R. Kamruddin, C.C. Constantinou, R. Dubrovka, and C.G Parini, "Radio channel characterization and antennas for on body communications," in *Proceeding of Loughborough Antennas and Propagation Conference*, Loughborough, UK, pp.330-333, April 2005.

[11] Alomainy, A.; Yang Hao; Owadally, A.; Parini, C.G.; Nechayev, Y.; Constantinou, C.C.; Hall, P.S., ", "Statistical Analysis and Performance Evaluation for On-Body Radio Propagation With Microstrip Patch Antennas," *IEEE Transactions on Antennas and Propagation,* vol. 55, no. 1, pp. 245-248, Jan. 2007.

[12]] Y. Hao, Alomainy, P. S. Hall, Y. I. Nechayev, C. G. Parini, and C. C. Constantinou, "Antennas and propagation for body centric wireless communications," in *IEEE/ACES International Conference on Wireless Communications and Applied Computational Electromagnet*, Honolulu, Hawaii, USA, 3-7 Apr, 2005.

[13] Alomainy, A.; Hao, Y.; Hu, X.; Parini, C.G.; Hall, P.S, "UWB on-body radio propagation and system modelling for wireless body-centric networks," *IEE Proceedings-Communications,,* vol. 153, no. 1, pp. 107-114, 2 Feb. 2006.

[14] E. R. Wade, A Body Area Network for Wearable Health Monitoring: Conductive Fabric Garment Utilizing DC Power Line Carrier Communication, Cambridge : MIT, 2007.

[15] M. Taj-Eldin, W. Kuhn and B. Natarajan, "Study of Radio Channel for Biomedical Sensors in Spacesuits," in *in 8th International Conference on Body Area Networks*, Boston, Sept 30-Oct 2, 2013.

[16] M. Taj-Eldin,W. Kuhn, B. Natarajan, and G. Peterson, "Investigation of practical antennas for astronaut body area network," *Wireless for Space and Extreme Environments (WiSEE), 2014 IEEE International Conference on,* pp. 1-7, 30-31 Oct. 2014.

[17] M. Taj-Eldin, B. Kuhn, A. Hodges, B. Natarajan, G. Peterson, M. Alshetaiwi, S. Ouyang, G. Sanchez, and E. Monfort-Nelson, "Wireless Propagation Measurements for Astronaut Body Area Network," in *Wireless for Space and Extreme Environments (WiSEE), 2013 IEEE International Conference on*, Baltimore, MD, Nov. 7-9 2013.

[18] M. Taj-Eldin, B. Kuhn, A. Hodges, B. Natarajan, G. Peterson, M. Alshetaiwi, S. Ouyang, G. Sanchez, and E. Monfort-Nelson, "Study of Wireless Propagation for Body Area Networks inside Spacesuits," *IEEE Sensors Journal,* vol. 14, no. 11, pp. 3810, 3818, Nov. 2014.

[19] M. Taj-Eldin, W. Kuhn, and B. Natarajan, "Wearable Textile Antennas: A Comparison of Antenna Performance Parameters versus Wear ability Issues at MedRadio

Band," 2015, under Preparation.

[20] Gabriel, C., T. Y. A. Chan, and E. H. Grant, "Admittance Models for Open-Ended Coaxial Probes and Their Place in Dielectric Spectroscopy," *Physics in Medicine and Biology,* vol. 39, no. 12, pp. 2183-2200, 1994.

[21] S. Gabriel, R. W. Lau, and C. Gabriel, "The dielectric properties of biological tissues: III. Parametric models for the dielectric spectrum of tissues," *Physics Med. Bio,* vol. 41, no. 11, 1996.

[22] D. Andreuccetti, "Dielectric Properties of Body Tissues," Italian National Research Council, 2010. [Online]. Available: http://niremf.ifac.cnr.it/tissprop/. [Accessed 15 03 2013].

[23] "An Internet Resource for the Calculation of the Dielectric Properties of Body Tissues," Institute for Applied Physics, Italian National Research Council, [Online]. Available: http://niremf.ifac.cnr.it/tissprop/.

[24] C. A. Balanis, Advanced Engineering Electromagnetics, second edition, Wiley , 2012.

[25] Trembly, B.S., "The Effects of Driving Frequency and Antenna Length on Power Deposition Within a Microwave Antenna Array Used for Hyperthermia," *Biomedical Engineering, IEEE Transactions on,* Vols. BME-32, no. 2, pp. 152,157, Feb. 1985.

[26] A. Vander Vost, A. Rosen, and Y. Kotsuka, RF/Microwave interaction with biological tissues, Wiley Series in Microwave and Optical Engineering, 2006.

[27] Federal Communications Commision (FCC), "Code of Federal Regulations (CFR), Title 47 Part 2, Section 2.1093, Radiofrequency radiation exposure evaluation: portable devices," October 2004. [Online]. Available: http://www.fcc.gov, .

[28] "IEEE Standard for safety levels with respect to human exposure to electromagnetic fields, 3 kHz to 300 GHz," IEEE, April 1999.

[29] "Biological effects and exposure criteria for radiofrequency electromagnetic fields," National Council on Radiation Protection and Measurements (NCRP), 1986.

[30] "Guidelines for limiting exposure to time-varying electric, magnetic, and electromagnetic fields (up to 300 GHz)," International Commission on Non-ionizing radiation Protection (ICNIRP), 1998.

[31] I. Chatterjee, M. J. Hagmann, O. P. Gandhi, "Electromagnetic absorption in a multilayered slab model of tissue under near field expoure conditions,"

Bioelectromagnetics , vol. 1, no. 4, pp. 379-388, 1980.

[32] M. Klemm and G. Troeste, "EM energy absorption in the human body tissues due to UWB antennas," *Progress In Electromagnetics Research,* vol. 62, pp. 261-280, 2006.

[33] M. N. Sadiku, Numerical Techniques in Electromagnetics, Second Edition, pp. 338-356, CRC Press, 2000.

[34] Kivekäs, O., Lehtiniemi, T. and Vainikainen, P, "On the general energy-absorption mechanism in the human tissue," *Microw. Opt. Technol. Lett,* vol. 43, no. 3, pp. 195-201, 2004.

[35] N. Kuster, Q. Balzano, "Energy absorption mechanism by biological bodies in the near field of dipole antennas above 300 MHz," *IEEE Transactions on Vechicular Technology,* vol. 1, no. 1, pp. 17-23, Feb 1992.

[36] A. Christ, A. Klingenboeck, and N. Kuster, "Energy Absorption in layered biological tissue and its consequence on the compliance testing of body-mounted wireless devices," *Progress in Electromagnetic Research Symposium ,* vol. 62, pp. 261-280, Hangzhour, August 13-26, 2005.

[37] C. A. Balanis, Antenna Theory, Analysis and Design, Third Edition, John Wiley and Sons, Inc, 2005.

[38] W. L Wong and C. I . Lin, "Characteristics of a 2.4-GHz compact shorted patch antenna in close proximity to a lossy medium," *Microw. Opt. Technol . Lett.,* vol. 45, no. 6, pp. 480-483, 2005..

[39] Huey-Ru Chuang; Wen-Tzu Chen, "Computer simulation of the human-body effects on a circular-loop-wire antenna for radio-pager communications at 152, 280, and 400 MHz," *Vehicular Technology, IEEE Transactions on,* vol. 46, no. 3, pp. 544-559, Aug. 1997.

[40] Salonen, P.; Rahmat-Samii, Y.; Kivikoski, M., "Wearable antennas in the vicinity of human body," *Antennas and Propagation Society International Symposium, 2004. IEEE,* vol. 1 , pp. 467,470, 20-25 June 2004.

[41] Sinha, B.s, "Numerical modeling of adsorption and scattering of EM energy radiated by cellular phones by human arm," *TENCON '98. 1998 IEEE Region 10 International Conference on Global Connectivity in Energy, Computer, Communication and Control ,* vol. 2, pp. 261-264, Dec. 1998.

[42] Wang, J. ; Fujiwara, O. ; Watanabe, S. ; Yamanaka, Y., "Computation with a parallel FDTD system of human-body effect on electromagnetic absorption for portable

telephones," *Microwave Theory and Techniques, IEEE Transactions on ,* vol. 52, no. 1, pp. 53- 58, Jan. 2004.

[43] A. Alomainy, Y. Hao and D. M Davenport, "Parametric Study of Wearable Antennas Varying Distances from the Body and Different On-Body Positions," *2007 IET Seminar on Antennas and Propagation for Body-Centric Wireless Communications,* pp. 84-89, 24-24 April 2007.

[44] P. S. Hall, Y. Hao, Antennas and Propagation for body-centric wireless communications, Artech House, 2nd edition, 2012.

[45] A. Alomainy, Y. Hao and F. Pasveer, "Numerical and expeimental evaluation of a compact sesor antenna for healthcase devices," *IEEE Transactions on medical circuits and systems,* vol. 1, no. 4, Dec. 2007.

[46] Kamarudin, M.R.; Nechayev, Y.I.; Hall, P.S., "Performance of antennas in the on-body environment," *Antennas and Propagation Society International Symposium, 2005 IEEE ,* vol. 3A, pp. 475,478, 3-8 July 2005.

[47] G. Conway and W. Scanlon, "Antennas for Over-Body-Surface Communication at 2.45 GHz," *Antennas and Propagation, IEEE Transactions on,* vol. 57, no. 4, pp. 844-855, April 2009.

[48] Sanz-Izquierdo, B. and Huang, F. and Batchelor, J.C., "Convert dual-band wearable button antenna," *IEEE Electronics Letters,* vol. 42 , no. 12, pp. 668-670, 2006.

[49] Scanlon, W.G.; Chandran, A.R, "Stacked-patch antenna with switchable propagating mode for UHF body-centric communications," *Antenna Technology, 2009. iWAT 2009. IEEE International Workshop on,* pp. 1,4, 2-4 March 2009.

[50] P. S. Hall, Y. Hao, Y. I. Nechayev, A. Alomainy, C. C. Constantinou, , C. G Parini , M. R Kamruddin, T., "Antennas and propagation for on-body communication systems," *IEEE Antenna Technology and Propagation Magazine,* vol. 49, no. 3, June 2007.

[51] A. Sani, "Modelling and Characterisation of Antennas and Propagation for Body-Centric Wireless Communication," Electronic Engineering, Queen Mary, University of London, London, UK, April 2010.

[52] H. D. Chen, J. S. Chen, Y. T. Chen, "Modified inverted-L monopole antenna for 2.4/5 GHz dual-band operations," *Electronics Letters,* vol. 39, no. 22, pp. 1567-1568, Oct 2003.

[53] Akhoondzadeh-Asl L., Khan I., Nechayev Y I, Hall P. S, "Investigation of polarization in on-body propagation channels," in *3rd European Conference on Antennas and*

Propagation, EuCAP 2009, 2009, pp. 466-469.

[54] Salonen, P.; Rahmat-Samii, Y, "Textile antennas: effects of antenna bending on input matching and impedance bandwidth," *Aerospace and Electronic Systems Magazine, IEEE,* vol. 22, no. 3, pp. 10-14, March 2007.

[55] Zhu, S.; Langley, R., "Dual-band wearable antennas over EBG substrate," *Electronics Letters,* vol. 43, no. 3, pp. 141,142,, Feb. 1 2007.

[56] Shaozhen Zhu; Langley, R., "Dual-Band Wearable Textile Antenna on an EBG Substrate," *Antennas and Propagation, IEEE Transactions on,* vol. 57, no. 4, pp. .926,935, April 2009.

[57] Hertleer, C.; Tronquo, A.; Rogier, H.; Vallozzi, L.; Van Langenhove, L., "Aperture-Coupled Patch Antenna for Integration Into Wearable Textile Systems," *Antennas and Wireless Propagation Letters, IEEE ,* vol. 6, pp. 392,395, , 2007.

[58] Hertleer, C.; Rogier, H.; Vallozzi, L.; Van Langenhove, L., "A Textile Antenna for Off-Body Communication Integrated Into Protective Clothing for Firefighters," *Antennas and Propagation, IEEE Transactions on,* vol. 57, no. 4, pp. 919,925, April 2009.

[59] Salonen, P.; Rantanen, J., "A dual-band and wide-band antenna on flexible substrate for smart clothing," *Industrial Electronics Society, 2001. IECON '01. The 27th Annual Conference of the IEEE ,* vol. 1, pp. 125,130 , 2001.

[60] Jaehoon Kim; Rahmat-Samii, Y., "Exterior antennas for wireless medical links: EBG backed dipole and loop antennas," *Antennas and Propagation Society International Symposium, 2005 IEEE ,* vol. 28, pp. .800,803, 3-8 July 2005.

[61] T. Rappaport, Wireless Communications Principles and Practice., New Jersey: Prentice Hall, Inc., 1996.

[62] A.A. Saleh and R. A. Valenzuela, "A statistical model for indoor multipath propagation," *IEEE Journal on Selected Areas in Communications,* vol. 5, no. 2, pp. 128-137, Feb. 1987.

[63] I. S. Kovacs, G. Pedersen, P. Eggeres, and K. Olsen, "Ultra wideband radio propagation in body area network scenario," *in ISSSTA Proceedings,* pp. 120-106, 2004.

[64] D. Neirynck, Channel Characterization and Physical Layer Analysis for Body and Personal Area Network, PhD Thesis, University of Bristol, November 2006..

[65] Kanda, M.Y.; Ballen, M.; Salins, S.; Chung-Kwang Chou; Balzano, Q., "Formulation and characterization of tissue equivalent liquids used for RF densitometry and

dosimetry measurements," *Microwave Theory and Techniques, IEEE Transactions on , vol.52, no.8, ,* vol. 52, no. 8, pp. 2046,2056, Aug. 2004.

[66] X. Xu, T. Chao, and A. Bozkurt, "VIP-Man: an image-based whole-body adult male model constructed from color photographs of the visible human project for multi-particle Monte Carlo calculations," *Health Physics,* vol. 78, no. 5, p. 476, 2000.

[67] M. N. O. Sadiku, Numerical Techniques in Electromagnetics with Matlab, CRC Press, 3rd Edition, April, 2009.

[68] "FDTD Simulation, EMPro 2013.07," Keysight Technologies, formerly (Agilent Technologies), [Online]. Available: http://edadocs.software.keysight.com/display/support/EMPro+Product+Documentation. [Accessed 09 2013].

[69] "FEM Simulation, EMPro 2013.07," Keysight Technologies, formerly (Agilent Technologies), [Online]. Available: http://edadocs.software.keysight.com/display/support/EMPro+Product+Documentation. [Accessed 09 2013].

[70] J. Chen and O. Gandhi, "Currents induced in an anatomically based model of a human forexposure to vertically polarized electromagnetic pulses," *IEEE Transactions on Microwave Theory and Tchniques ,* vol. 39, no. 1, pp. 31-39, 1991.

[71] W. G. Scanlon, N. E. Evans, and Z. McCresh, "RF performance of a 418 MHz radio telemeter packaged for human vainal placement," *IEEE Transactions on Biomedical Engineering,* vol. 44, no. 5, pp. 427-430, May 1997.

[72] W. Xia, K. Saito, M. Takahashi, and K. Ito, "Performaces of an implanted cavity slot antennas embdded in the human arm," *IEEE Transactions on Antennas and Propagation,* vol. 57, no. 4, pp. 894-899, 2009.

[73] N. Haga, K. Saito, M. Takahashi, and K. Ito, "Characteristics of cavity slot antennas for body-area networks," *IEEE Transactions on Antennas and Propagation,* vol. 57, no. 4, pp. 837-843, 2009.

[74] O. Gandhi, B. Gao, and J. Chen, " A frequency-dependent finite-difference time-domain formulation forgeneral dispersive media," *IEEE Transactions on Microwave Theory and Techniques,* vol. 41, no. 4, pp. 658-665, 1993.

[75] P. Monk and E. Suli, "Error estimates for yee's method on non-uniform grids," *IEEE Trans. Mag.,* vol. 30, pp. 3200-3203, 1994.

[76] "NASA," The National Aeronautics and Space Administration, [Online]. Available: www.nasa.gov.

[77] "EMF Shielding & Conductive Fabrics," LessEMF, 2013. [Online]. Available: http://www.lessemf.com/fabric.html.

[78] C. R. Paul, Introduction to Electromagnetic Compatibility, 2nd. Ed., , John Wiley & Sons, 2006.

[79] Emerson M.; Pugh, Emerson W. Pugh , Principles of Electricity and Magnetism. 2nd ed. Paperback, Addison Wesley Longman Publishing Co, 1970.

[80] J. Griffiths., Introduction to Electromagnetism, 3rd Edition, New Jersey: Prentice Hall, 1999.

[81] D. Giancoli, Physics: Principles with Applications (7th Edition), Addison-Wesley, June 16, 2013.

[82] M. Thompson, "Physics 623 Transmission Lines," University of Wisconsin Madison, 22 Aug 2007. [Online]. Available: http://www.physics.wisc.edu/undergrads/courses/fall2012/623/sn/1-Transmission_Line_notes.pdf.

[83] Namjun Cho; Yoo, J.; Seong-Jun Song; Jeabin Lee; Seonghyun Jeon; Hoi-Jun Yoo, "The Human Body Characteristics as a Signal Transmission Medium for Intrabody Communication," *IEEE Transactions on Microwave Theory and Techniques,* vol. 55, no. 5, pp. 1080,1086, May 2007.

[84] "Using Conformal FDTD Meshing," Agilent Technologies , [Online]. Available: http://edocs.soco.agilent.com/display/empro201101/Using+Conformal+FDTD+Meshing. [Accessed 20 Feb 2012].

[85] "Specifying FEM Simulation Setup," Agilent Technologies , [Online]. Available: http://edocs.soco.agilent.com/display/empro2011/Specifying+FEM+Simulation+Setup. [Accessed 5 August 2013].

[86] A. F. b. Linx, "ANT-433-CW-RAH-xxx," [Online]. Available: http://www.linxtechnologies.com/resources/data-guides/ant-433-cw-rah.pdf. [Accessed 04 2015].

[87] Antenna Factor by Linx, "RAH Series Right Angled Helical Antenna (2.4GHz) - SMA," [Online]. Available: http://www.simplesolutions-uk.com/products/antenna-bluetooth-zigbee-wifi-band-rf-antenna-24ghz-868mhz-433mhz-418mhz-315mhz/rah-series. [Accessed 23 04 2015].

[88] A.R. Chandran; G.A. Conway; W.G. Scanlon, "Compact Slot-Loaded Path Antenna for 868 MHz Wireless body area networks," in *LAPC 2008 Loughborough Antennas and Propagation Conference*, 2008.

[89] M. Grimm; D. Manteuffel, "Norton Surface Waves in the Scope of Body Area Networks," *IEEE Trans. on Antennas and Propagation,* vol. 62, no. 5, pp. 2616,2623, May 2014.

[90] W.C. Elmore; Heald, M. A. Heald, Physics of Waves., Courier Dover Publications, ISBN 0-486-64926-1, 1969.

[91] B. Dunbar, "Interactive Spacesuit Experience: Clickable Spacesuit," NASA, 13 11 2008. [Online]. Available: http://www.nasa.gov/audience/foreducators/spacesuits/home/clickable_suit.html. [Accessed 03 02 2014].

[92] *IEEE Recommended Practice for Measurements and Computations of Radio Frequency Electromagnetic Fields with Respect to Human Exposure to Such Fields, 100 KHz - 300 GHz, IEEE Std C95.3, 2002 (R2008).*

[93] G. Kang, and O. P. Gandhi, "Effect of dielectric properties on the peak 1- and 10-g SAR for 802.11 a/b/g frequencies 2.45 and 5.15 to 5.85 GHz," *IEEE Trans. Electrom. Comp.,* vol. 46, pp. 268-274, May 2004.

[94] D. Prasad Gon, and P. Paul , "Complex Garment Systems to Survive in Outer Space," *Journal of Textile and Apparel, Technology and Management,* vol. 7, no. 2, 2011.

[95] Ma, L.; Edwards, R.M.; Bashir, S.; Khattak, M.I., "A wearable flexible multi-band antenna based on a square slotted printed monopole," *Antennas and Propagation Conference, 2008. LAPC 2008. Loughborough ,* pp. 345,348, 17-18 March 2008.

[96] Soh, P.J.; Van den Bergh, B.; Hantao Xu; Aliakbarian, H.; Farsi, S.; Samal, P.; Vandenbosch, G.A.E.; Schreurs, D.M.M.; Nauwelaers, B.K.J.C., "A Smart Wearable Textile Array System for Biomedical Telemetry Applications," *Microwave Theory and Techniques, IEEE Transactions on ,* vol. 61, no. 5, pp. 2253,2261, May 2013.

[97] Mandal, B.; Chatterjee, A.; Parui, S.K., "A wearable button antenna with FSS superstrate for WLAN health care applications," *RF and Wireless Technologies for Biomedical and Healthcare Applications (IMWS-Bio), 2014 IEEE MTT-S International Microwave Workshop Series on,* pp. 1-3, Dec 2014.

[98] Zhi Hao Jiang; Brocker, D.E.; Sieber, P.E.; Werner, D.H., "A Compact, Low-Profile Metasurface-Enabled Antenna for Wearable Medical Body-Area Network

Devices," *Antennas and Propagation, IEEE Transactions on ,* vol. 62, no. 8, pp. 4021,4030, Aug. 2014.

[99] Cara, D.D.; Trajkovikj, J.; Torres-Sanchez, R.; Zurcher, J.; Skrivervik, A.K., "A low profile UWB antenna for wearable applications: The tripod kettle antenna (TKA)," *Antennas and Propagation (EuCAP), 2013 7th European Conference on ,* pp. 3257,3260, 8-12 April 2013.

[100] Mahmud, M.S.; Jabri, F.J.J.; Mahjabeen, B., "Compact UWB Wearable antenna on leather material for wireless applications," *Antennas and Propagation Society International Symposium (APSURSI), 2013 IEEE ,* pp. 2191,2192, 7-13 July 2013.

[101] Abbasi, Q.H.; Rehman, M.U.; Xiaodong Yang; Alomainy, A.; Qaraqe, K.; Serpedin, E., " Ultrawideband Band-Notched Flexible Antenna for Wearable Applications," *Antennas and Wireless Propagation Letters, IEEE ,* vol. 12, pp. 1606,1609, 2013.

[102] Ur-Rehman, M.; Abbasi, Q.H.; Akram, M.; Parini, C., "Design of band-notched ultra wideband antenna for indoor and wearable wireless communications," *Microwaves, Antennas & Propagation, IET,* vol. 9, no. 3, pp. 243,251, 2 19 2015.

[103] Alqadami, A.S.M.; Jamlos, M.F., " Design and development of a flexible and elastic UWB wearable antenna on PDMS substrate," *Applied Electromagnetics (APACE), 2014 IEEE Asia-Pacific Conference on ,* pp. 27,30, 8-10 Dec. 2014.

[104] Watanabe, T.; Iwasaki, H., "Wearable Finger dual band antenna for BAN," *Antennas and Propagation in Wireless Communications (APWC), 2012 IEEE-APS Topical Conference on ,* pp. 51,54 , 2-7 Sept. 2012.

[105] Sugiyama, H.; Iwasaki, H., "Wearable finger ring dual band antenna made of fabric cloth for BAN use," *Antennas and Propagation (EuCAP), 2013 7th European Conference on ,* pp. 3556,3559, 8-12 April 2013.

[106] Dwibedi, K.; Patel, P.; Poonkuzhali, R.; Thiripurasundari, D.; Alex, Z.C., "Dual band CPW fed wearable monopole antenna," *Information & Communication Technologies (ICT), 2013 IEEE Conference on,* pp. 1134,1137, 11-12 April 2013.

[107] Sundarsingh, E.F.; Velan, S.; Kanagasabai, M.; Sarma, A.K.; Raviteja, C.; Alsath, M.G.N., "Polygon-Shaped Slotted Dual-Band Antenna for Wearable Applications," *Antennas and Wireless Propagation Letters, IEEE ,* vol. 13, pp. 611,614, 2014.

[108] Velan, S.; Sundarsingh, E.F.; Kanagasabai, M.; Sarma, A.K.; Raviteja, C.; Sivasamy, R.; Pakkathillam, J.K., "Dual-Band EBG Integrated Monopole Antenna Deploying Fractal Geometry for Wearable Applications," *Antennas and Wireless Propagation Letters, IEEE ,,* vol. 14, pp. 249,252, 2015.

[109] Nagarjun, R.; George, G.; Thiripurasundari, D.; Poonkuzhali, R.; Alex, Z.C., "Design of a triple band planar bow-tie antenna for wearable applications," *Information & Communication Technologies (ICT), 2013 IEEE Conference on ,* pp. 1185,1189, 11-12 April 2013.

[110] Agneessens, S.; Rogier, H., "Compact Half Diamond Dual-Band Textile HMSIW On-Body Antenna," *Antennas and Propagation, IEEE Transactions on ,* vol. 62, no. 5, pp. 2374,2381, May 2014.

[111] C. Wu, T. Chien, C. Luo, "Design of Novel S-Shaped Quad-Band Antenna for MedRadio/WMTS/ISM Implantable Biotelemetry Applications," *International Journal of Antennas & Propagation;2012, p1,* Jan. 2012.

[112] T. Castel, et al., "Improved Reception of In-Body Signals by Means of a Wearable Multi-Antenna System," *International Journal of Antennas and Propagation,* vol. 2013, no. Article ID 328375, 2013.

[113] Merli, F.; Bolomey, L.; Zurcher, J.; Corradini, G.; Meurville, E.; Skrivervik, A.K., "Design, Realization and Measurements of a Miniature Antenna for Implantable Wireless Communication Systems," *Antennas and Propagation, IEEE Transactions on,* vol. 59, no. 10, pp. 3544, 3555, Oct. 2011.

[114] Psathas, K.A.; Nikita, K.S., "Evaluation of miniature implantable antenna and telemetry link for intracranial pressure monitoring," *Wireless Mobile Communication and Healthcare (Mobihealth), 2014 EAI 4th International Conference on ,* pp. 207,210, 3-5 Nov. 2014.

[115] Kiourti, A.; Costa, J.R.; Fernandes, C.A.; Nikita, K.S., "A Broadband Implantable and a Dual-Band On-Body Repeater Antenna: Design and Transmission Performance," *Antennas and Propagation, IEEE Transactions on ,* vol. 62, no. 6, pp. 2899,2908, June 2014.

[116] T. Kellomaki, "Effects of the Human Body on Single-Layer Wearable Antennas," Tampere University of Technology Publication 1025, Finland , March 2012.

[117] H. A. Rahim, F. Malek, I. Adam, S. Ahmad, N. B. Hashim, and P. S. Hall, "Design and Simulation of a Wearable Textile Monopole Antenna for Body Centric Wireless Communications," *Progress In Electromagnetics Research Symposium Proceedings, Moscow, Russia,* pp. 19-23, August 2012 .

[118] Soh, P.J.; Vandenbosch, G.A.E.; Volski, V.; Nurul, H.M.R., "Characterization of a simple broadband textile planar inverted-F antenna (PIFA) for on body communications," *ICECom, 2010 Conference Proceedings ,* vol. 8, pp. 1,4, 20-23 Sept. 2010.

[119] H. Morishita and N. T. Hung, "Characteristics of Antennas with Folded Structure," *Proceedings of ISAP2012,* 2012, Nagoya, Japan.

[120] Nagatoshi, M.; Morishita, H.; Tanaka, S.,, "A study on an improvement of folded bow-tie antenna by adding aditional elements," *Antennas and Propagation (APSURSI), 2011 IEEE International Symposium on,* pp. 630,633, 3-8 July 2011.

[121] Chandra, R.; Johansson, A.J.,, "An Analytical Link-Loss Model for On-Body Propagation Around the Body Based on Elliptical Approximation of the Torso With Arms' Influence Included," *Antennas and Wireless Propagation Letters, IEEE ,* vol. 12, pp. 528,531, , Feb 2013.